

Fine Structure of the Isoscalar Giant Quadrupole Resonance from High-Resolution Inelastic Proton Scattering Experiments

Vom Fachbereich Physik
der Technischen Universität Darmstadt

zur Erlangung des Grades
eines Doktors der Naturwissenschaften
(Dr. rer. nat.)

genehmigte

D i s s e r t a t i o n

angefertigt von

Artem Shevchenko
aus Kharkiv (Ukraine)

Februar 2005

Darmstadt
D 17

Referent: Professor Dr. rer. nat. Dr. h.c. mult. A. Richter

Korreferent: Professor Dr. rer. nat. J. Wambach

Tag der Einreichung: 08.02.2005

Tag der Prüfung: 25.04.2005

Zusammenfassung

Im Rahmen dieser Arbeit wurde eine systematische Untersuchung des Phänomens der Feinstruktur der isoskalaren Quadrupol-Riesenresonanz in Atomkernen durchgeführt. Hierzu wurde eine Reihe von hochauflösenden Protonenstreuexperimenten am iThemba LABS in Südafrika durchgeführt. Die in diesen Experimenten erreichte Energieauflösung von $\Delta E < 50$ keV (FWHM) erlaubte es erstmals, die Feinstruktur in allen untersuchten Kernen, ^{58}Ni , ^{89}Y , ^{90}Zr , ^{120}Sn , ^{142}Nd , ^{166}Er , ^{208}Pb , zu beobachten. Damit wurde gezeigt, dass die Feinstruktur der Quadrupol-Riesenresonanz ein globales Phänomen ist.

Die Feinstruktur wird durch charakteristische Energieskalen beschrieben, die den Zerfall von Riesenresonanzen über eine Hierarchie von Kopplungen an komplexere Zustände charakterisieren. Im Rahmen dieser Arbeit wurden die Skalen mit Hilfe der Entropie-Index-Methode und neuen, auf einer Waveletanalyse basierenden Verfahren, die zum Teil in dieser Dissertation entwickelt wurden und weitergehende Informationen als die Entropie-Index-Methode liefern, extrahiert.

Die ermittelte Systematik zeigt eine Präsenz von drei globalen Klassen der Skalen. Zu der ersten Klasse gehören die Skalen mit Größen von unter 100 keV, die in allen Kernen beobachtet wurden. Die zweite Gruppe von Skalen beinhaltet Skalen im Bereich von 100 keV bis 1 MeV. Diese Gruppe zeigt grössere Variationen der Skalenwerte von Kern zu Kern. Die dritte Klasse spiegelt die Skalen oberhalb 1 MeV wider, die der Breite der Quadrupole-Riesenresonanz entsprechen.

Um die physikalische Natur der Skalen interpretieren zu können, wurden die experimentell bestimmten Werte mit theoretischen Vorhersagen im Rahmen verschiedener mikroskopischer Vielteilchenmodellen verglichen. Eine qualitative Übereinstimmung zwischen den aus dem Experiment und den theoretischen Modellen extrahierten Skalen bestätigt, dass die Zweiteilchen-Zweiloch-Konfigurationen eine entscheidende Rolle für die Bildung der Feinstruktur spielen. Eine quantitative Betrachtung zeigt dabei, dass die verschiedenen Modelle unterschiedliche Werte für die berechneten Skalen ergeben.

Eine detaillierte Analyse der Rolle der verschiedenen Prozesse im Zerfall der Quadrupol-Riesenresonanz zeigt, dass in den schweren Kernen die kollektive Dämpfung, die durch die Kopplung der Einteilchen-Einlochzuständen an kollektive

Oberflächenvibrationen zustande kommt, alle Skalen verursacht und eine entscheidende Rolle beim Zerfall spielt. Ein nichtkollektiver Dämpfungsmechanismus, bei dem Einteilchen-Einlochzustände an Vielteilchen-Viellochzustände gekoppelt sind, ergibt hingegen keine prominenten Skalen. Durch den Vergleich mit einem Modell stochastischer Kopplung wurden generische Eigenschaften dieser nichtkollektiven Dämpfung extrahiert.

Summary

In the present work the phenomenon of fine structure in the region of the isoscalar giant quadrupole resonance in a number of heavy and medium-heavy nuclei is systematically investigated for the first time. High energy-resolution inelastic proton scattering experiments were carried out in September-October 2001 and in October 2003 at the iThemba LABS cyclotron facility in South Africa with an incident proton energy of 200 MeV.

The obtained data with the energy resolution of $\Delta E < 50$ keV FWHM revealed the appearance of fine structure in all the nuclei studied (^{58}Ni , ^{89}Y , ^{90}Zr , ^{120}Sn , ^{142}Nd , ^{166}Er , ^{208}Pb), thereby establishing the global character of this phenomenon.

Fine structure can be described using *characteristic energy scales*, appearing as a result of the decay of collective modes towards the compound nucleus through a hierarchy of couplings to complex degrees of freedom. For the extraction of the characteristic energy scales from the spectra an entropy index method and a novel technique based on the wavelet analysis are utilized.

The global analysis of available data shows the presence of three groups of scales, according to their values. To the first group belong the scales with the values around and below 100 keV, which were detected in all the nuclei studied. The second group contains intermediate scales in the range of 100 keV to 1 MeV. These scales show large variations depending on the nuclear structure of the nucleus. The largest scales above 1 MeV are classified to the third group, describing the global structure of the resonance (the width).

The interpretation of the observed scales is realized via the comparison with microscopic model calculations including the coupling of the initial *one-particle-one-hole* excitations to more complex configurations. A qualitative agreement of the experimentally observed scales with those obtained from the theoretical predictions supports the suggestion of the origin of fine structure from the coupling to the *two-particle-two-hole* states. However, quantitatively, large deviations are observed for the values of scales given by different models.

A more detailed study of the physical nature of extracted scales is provided with the help of the *quasiparticle-phonon model* and *extended time-dependent Hartree-Fock model*, which allow to separate the contributions from different damping

mechanisms. The main source of the observed scales is identified to arise from the *collective damping* mechanism, which is the coupling to *low-lying surface vibrations*. This conforms with the doorway picture of the damping of giant resonances. At the same time, through the comparison with a model of *stochastic coupling* to many *particle-hole* states some generic features of the *non-collective damping* mechanism could be extracted.

Table of contents

| | | |
|----------|--|-----------|
| 1 | Introduction | 1 |
| 2 | Excitation and Decay of Giant Resonances | 3 |
| 2.1 | Doorway-State Picture of Giant Resonances | 5 |
| 2.2 | Fine Structure and Characteristic Scales in the Nuclear Response | 8 |
| 3 | High-Resolution Proton Scattering at iThemba LABS | 11 |
| 3.1 | Separated-Sector Cyclotron Facility | 11 |
| 3.2 | The K600 Magnetic Spectrometer | 13 |
| 3.3 | Dispersion Matching Techniques | 16 |
| 4 | Experiment | 18 |
| 4.1 | Experimental Procedure | 19 |
| 4.2 | Data Acquisition and Online Analysis | 21 |
| 4.3 | Offline Data Analysis | 22 |
| 4.4 | Measured Spectra | 28 |
| 5 | Search for Characteristic Energy Scales of Fluctuations | 34 |
| 5.1 | Characterization of Quantum-Chaotic Phenomena | 34 |
| 5.2 | Entropy Index Method | 36 |
| 5.3 | Results of the Entropy Index Analysis | 38 |
| 5.4 | Limitations of the Entropy Index Method | 40 |
| 5.5 | Local Scaling Dimension | 41 |
| 5.6 | Fourier Analysis | 41 |
| 5.7 | Windowed Fourier Transform | 42 |

| | | |
|----------|--|-----------|
| 6 | Wavelet Analysis | 43 |
| 6.1 | Wavelet Transform | 43 |
| 6.2 | Continuous vs. Discrete Wavelet Transform | 46 |
| 6.3 | Properties of the Wavelet Transform and Wavelet Functions . . . | 48 |
| 6.3.1 | Linearity of the Wavelet Transform | 48 |
| 6.3.2 | Vanishing Moments | 48 |
| 6.4 | Selection of the Optimal Wavelet Function | 49 |
| 6.4.1 | Haar Wavelet | 49 |
| 6.4.2 | Mexican Hat and Other Derivatives of a Gaussian | 50 |
| 6.4.3 | Morlet Wavelet | 50 |
| 6.4.4 | Biorthogonal Wavelet Bior3.9 | 51 |
| 6.5 | Results of the CWT | 52 |
| 6.5.1 | Scales from the GQR in ^{208}Pb | 52 |
| 6.5.2 | Scales in Other Magic Nuclei | 54 |
| 6.5.3 | Importance of Wavelet Function Selection | 57 |
| 6.5.4 | Role of Other Multipoles | 58 |
| 6.5.5 | Role of Shell Closures and Deformation | 60 |
| 6.5.6 | Summary of Extracted Scales in the ISGQR Region | 61 |
| 6.6 | Discrete Wavelet Analysis | 63 |
| 7 | Fine Structure and Microscopic Models for the Damping of Giant Resonances | 69 |
| 7.1 | Mean Field Approximation | 69 |
| 7.2 | Models Beyond the Mean Field | 70 |
| 7.2.1 | Second-RPA Model | 72 |
| 7.2.2 | Extended Time-Dependent Hartree-Fock Model | 72 |
| 7.2.3 | Extended Theory of Finite Fermi Systems | 73 |
| 7.2.4 | Quasiparticle-Phonon Model | 73 |

| | | |
|----------|---|-----------|
| 8 | Results and Discussion | 79 |
| 8.1 | Origin of Fine Structure | 79 |
| 8.2 | Comparison of Extracted Scales | 80 |
| 8.3 | Collective vs. Non-Collective Damping | 84 |
| 8.4 | Nature of the Non-Collective Damping | 91 |
| 8.4.1 | Picket-Fence Model | 91 |
| 8.4.2 | Stochastic Coupling Model | 92 |
| 9 | Summary and Outlook | 94 |

1 Introduction

Electric and magnetic giant resonances in the atomic nucleus represent a spectacular example of the complexity of collective phenomena that take place in many-body fermionic quantum systems. In atomic nuclei these collective excitations of atomic nuclei are usually classified according to their multipolarity ΔL , spin ΔS and isospin ΔT quantum numbers [1, 2].

The first experimental observation of the phenomenon of increased absorption cross section of photons in some nuclei was made by Bothe and Gentner [3] and was later confirmed by Baldwin and Klaiber [4]. An interpretation was given by Goldhaber and Teller [5] within the macroscopic hydrodynamical model, which treated protons and neutrons as rigid fluids, oscillating relative to each other. This mode was identified as an isovector giant dipole resonance (IVGDR), characterized by the multipolarity, spin and isospin transfers $\Delta L = 1$, $\Delta S = 0$, and $\Delta T = 1$, respectively. The second experimentally observed collective mode in atomic nuclei was the isoscalar giant quadrupole resonance (ISGQR). Since its discovery [6], this mode has been also extensively studied in different nuclei in various reactions [7–18], so that nowadays systematic experimental data exist on its energy centroid, width, and the exhausted strength in terms of the *energy-weighted sum rule* (EWSR) [10]. Macroscopically the ISGQR can be described as a quadrupole ($\Delta L = 2$) shape vibration of a nucleus, the protons and neutrons oscillating in phase, thereby defining the isoscalar ($\Delta T = 0$) nature of this resonance.

In the past decades many other collective modes were found to exist in atomic nuclei. A remarkable progress in the understanding such elementary modes of excitations has been made both experimentally and theoretically [2, 19]. A tremendous amount of experimental work has been carried out towards the investigation of global dependencies and systematics of those modes in various nuclei. The macroscopic properties of giant resonances, like centroid energies and widths, are now well studied for many nuclei. Despite all the experimental and theoretical efforts, our knowledge about the internal collective processes in the nucleus is still very limited [19–22]. Perhaps one of the most urgent problems that has to be solved for a complete understanding of intrinsic damping mechanisms of giant resonances, is a - presently lacking - consistent explanation of the corresponding

decay widths observed experimentally. Modern sophisticated many-body theories often predict the centroid energies of the resonances quite well, however, they fail when attempting to describe their widths. This problem is directly related to the question of the dominant decay mechanisms of giant resonances. An early experimental observation of fine structure in the region of giant quadrupole resonance [23] was much debated until the hadronic reactions of comparable resolution did confirm the physical nature of the observed fluctuations. Novel methods for the analysis of fine structure phenomena were developed recently [24–27]. Application to the ^{208}Pb data suggests the coupling between $1p-1h$ and $2p-2h$ states as an origin of fine structure, described by the characteristic scales. However, a question remained, whether the observed phenomenon is a peculiar feature of the doubly-magic ^{208}Pb nucleus, or is it a global one.

The aim of the present work was a systematic study of the phenomenon of fine structure and associated characteristic scales of the ISGQR in heavy and medium-heavy nuclei. A number of high-resolution inelastic proton scattering experiments on a wide mass range of nuclei were carried out at iThemba LABS in order to solve this question.

The thesis is structured in the following way. Chapter 2 provides an introduction into the problem of understanding the intrinsic mechanisms of excitation and decay of giant resonances. A widely-accepted doorway picture for the damping of collective excitations in many-body quantum systems is discussed. Chapter 3 describes the facility at iThemba LABS and the experimental setup for high-resolution scattering experiments. Chapter 4 deals with the technical details of the experiments carried out. The main steps in the data analysis, and the finally obtained excitation spectra of the nuclei studied are presented. The techniques for characterizing the fine structure and extracting information out of it are outlined in Chapter 5, emphasizing the well-established entropy index analysis. Chapter 6 introduces a novel wavelet transform technique. The results of a wavelet analysis applied to the experimental data and comparison with those from the microscopic model calculations are given. Modern theoretical approaches to the description of excitation and decay of giant resonances are briefly introduced in Chapter 7. Results of the comparative analysis of theoretical predictions and experimental findings are presented in Chapter 8. The thesis closes with a summary and an outlook.

2 Excitation and Decay of Giant Resonances

The decay of giant resonances in nuclei is an excellent example of how a well-ordered collective excitation dissolves into disordered motion of internal degrees of freedom in quantum many-body systems [20]. Microscopically, giant resonances are generally described within the *random-phase approximation* (RPA) theories [28, 29], where each nucleon is moving in an average mean-field potential created by all the other nucleons, but without interacting with any other nucleon. Collective modes are treated as small-amplitude vibrations around the ground state. These vibrations are described via coherent overlap of many *one-particle–one-hole* ($1p - 1h$) excitations. A schematic representation of such a microscopic description of the GQR for the example of the ^{90}Zr nucleus can be seen in Fig. 2.1,

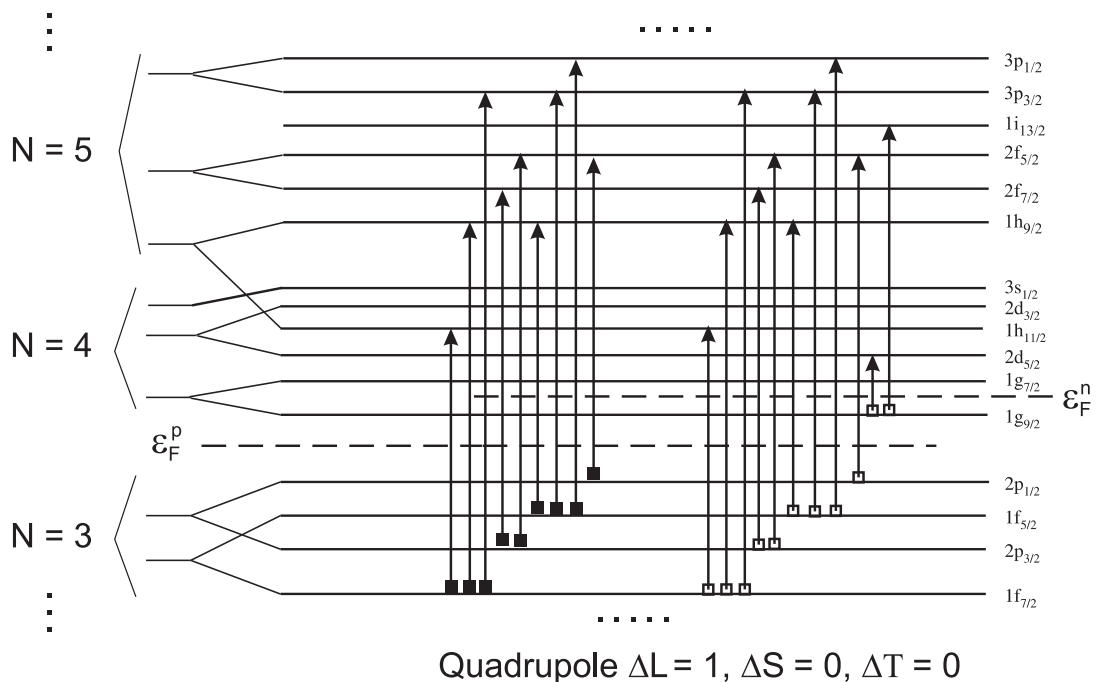


Fig. 2.1: An example of microscopic representation of giant resonances as a coherent superposition of many *particle-hole* transitions. Shown is the case for electric electric quadrupole ($\Delta L = 2$) excitation in the ^{90}Zr nucleus. Proton (arrows with solid squares) and neutron (arrows with open squares) $1p - 1h$ transitions from and to corresponding energy levels below and above the Fermi level ϵ_F , which contribute coherently to a given collective mode, are shown.

where $1p-1h$ transitions contributing coherently to a quadrupole ($\Delta L = 2$) mode are displayed. The existence of many differently coupled particle-hole excitations induces a chaotic behavior in such a quantum many-body system with a large number of degrees of freedom. This gives rise to the phenomenon of chaos-driven decay of the collective motion of nucleons and appears as fluctuations and fine structure in the nuclear response.

The RPA approach is the small amplitude limit of the *time-dependent Hartree-Fock* (TDHF) model. It is rather successful in predicting the position and the strength of giant resonances. However, it is not suitable for describing the damping of the collective excitations. For a realistic description of how these modes decay, one has to go beyond the mean-field theory and take into account the mixing of $1p-1h$ excitations with more complex configurations.

In many-body systems the damping of excitations appears to be very complex since it can involve many different processes. Already at the mean-field level the RPA predicts only sharp states, with a resonance width acquired via several damping processes (e.g. a fragmentation of the collective response into several collective states, a process known in solid state and plasma physics as *Landau damping*, which is the damping via coupling to uncorrelated *particle-hole* excitations). This process is believed to be unimportant for giant resonances, with the exception of the light nuclei. Another possibility for strength fragmentation is via nuclear deformations, which can shift the energies of $p-h$ excitations contributing to the collective mode, a process often referred to as *inhomogeneous damping*. Finally, particle or γ -decay might also produce additional broadening of resonance strength.

For the case of electric giant resonances in heavy nuclei, the strength distributions are well approximated by assuming a Lorentzian line shape with a resonance decay width Γ . This width is usually explained to result from several contributions:

$$\Gamma = \Delta\Gamma + \Gamma^\uparrow + \Gamma^\downarrow. \quad (2.1)$$

Here, $\Delta\Gamma$ is the width acquired via a fragmentation of initial $1p-1h$ states at the mean-field level, which is caused by *Landau damping*. Another contribution is the *escape width* Γ^\uparrow , which expresses the coupling to the continuum, i.e. direct decay via particle emission from the initial $1p-1h$ states. The third possibility Γ^\downarrow

describes the *spreading width*, which arises due to internal mixing with $2p-2h$ and more complex configurations. The explanation for the spreading width is given by the commonly-accepted *doorway model* for the decay of giant resonances. This concept is discussed in more detail in the next subsection.

2.1 Doorway-State Picture of Giant Resonances

It is generally accepted that internal mixing occurs through a hierarchy of couplings towards more and more complex degrees of freedom in the nucleus, starting from the *two-particle-two-hole* ($2p-2h$) and finally coming up to the $np-nh$ states of the compound nucleus. The *doorway* mechanism is expected to dominate the damping of giant resonances in heavy nuclei. The concept of *doorway* states was introduced by Block and Feshbach [30] and was later generally formulated by Feshbach [31, 32].

A schematic representation of the damping of giant resonances within a *doorway* picture is shown in Fig. 2.2. At $t = 0$ the nucleus is excited from its ground state

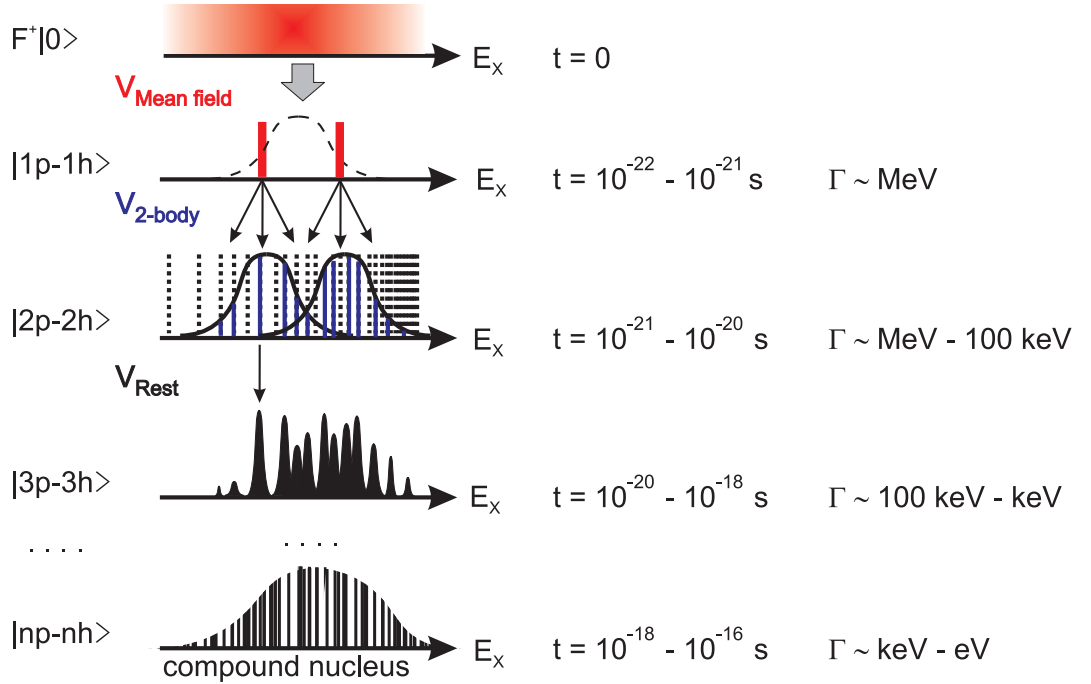


Fig. 2.2: Damping of giant resonances. A hierarchy of lifetimes and energy scales in the decay of giant resonances as a result of different processes.

$|0\rangle$ by an external field, producing an infinite spectrum of eigenvalues $\mathbf{F}^+ |0\rangle$. At the very first step, a mean field is settled down in the system by the time of $t = 10^{-22} - 10^{-21}$ s, thereby allowing only few dominant frequencies to be selected in the nuclear response, which correspond to energies of the so-called *doorway states*. Though these states, described by the RPA, do not have any width, the fragmentation of strength by a few MeV might appear if the number of such *doorways* is more than one. This is believed to be significant only for light nuclei. On the next level, these *doorway* states couple via *residual two-body interaction* to the more complicated $2p - 2h$ states, thereby acquiring an additional width. Most of these $2p - 2h$ configurations are so-called *background states* (shown as dashed lines in Fig. 2.2), the coupling to which is weak and stochastic. Embedded in such a background are a few collective $2p - 2h$ states, the coupling to which is much stronger (solid lines at the $2p - 2h$ level in Fig. 2.2). As these states, when observed experimentally, are partially overlapping, fine structure appears in the nuclear response. On this level, the energy scales from several MeV down to hundreds of keV are expected to be observed. Some of these $2p - 2h$ states can in turn serve as *doorways* and couple via *residual interaction* to even more complex configurations. This chain of couplings can be continued down to the level of compound nucleus, where the energy is already equally distributed over all available degrees of freedom. It might take $t = 10^{-16}$ s unless such a system experiences a subsequent decay via a particle or gamma emission, a process known as *statistical decay*.

In reality, the width associated with the coupling to $3p - 3h$ and more complicated states, and eventually to the totally mixed states describing the compound nucleus, does not differ substantially from the spreading produced by the *doorway coupling* to $2p - 2h$, because the increase of the density of complex states is compensated for by the decrease of the coupling matrix elements. The effect of this coupling is reflected in a smoothly varying strength function. Actually, a particle decay out of the system might take place at any step of this hierarchy. Accordingly, one can distinguish between different types of decay processes, as shown in Fig. 2.3.

The decay reactions may be qualitatively classified as due to direct, semi-direct, pre-equilibrium, or statistical processes. Direct decay occurs via coupling of the initial $1p - 1h$ states to the continuum, leading to direct emission of the particle,

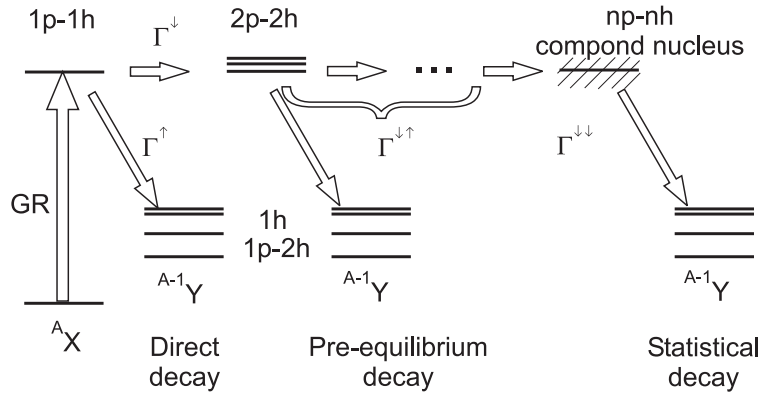


Fig. 2.3: Schematic representation of the different decay processes that might take place at different stages of the damping of collective motion [2].

which takes excitation energy out from the system. Preferential decays of the resonance to particular one-hole states in the residual nucleus are called *direct*. The corresponding escape width Γ^\uparrow depends significantly on the mass number A , the excitation energy, the multipolarity, and may be not negligible in lighter nuclei. The resonance may also mix with more complicated states, like surface vibrations or $2p-2h$ states, giving rise to the spreading width Γ^\downarrow . It can be further separated into two parts, $\Gamma^{\downarrow\uparrow}$ for the decays of the intermediate configurations (pre-equilibrium decay) and $\Gamma^{\downarrow\downarrow}$ for the statistical decay of equilibrated compound nucleus. The relative probability of different decay channels for such decays are predicted by the Hauser-Feshbach calculations, describing statistical decay as an evaporation of the particle from the equilibrated compound nucleus.

The separation between direct- and compound-decay can be eventually obtained through model-dependent calculations. Thus, by studying the particle decay of giant resonances, e.g. by means of coincidence experiments, as it was done e.g. at the S-DALINAC [33–35] and iThemba LABS [34, 36], and comparing the results with the Hauser-Feshbach model predictions, one can gain information about the predominant decay path of such collective modes in different nuclei. In the case where the observed experimental spectra cannot be accounted for by the statistical model calculations, the presence of a direct decay component can be invoked [20].

In order to understand the resonance decay towards the compound nucleus, one has to go beyond the mean field and include the couplings to more complex configurations in the microscopic description. The two-body nature of the nuclear

interaction suggests that the $2p-2h$ components of the many-body wave-function play the dominant role in the damping of giant resonances. The most effective amongst them are those containing an uncorrelated *particle-hole* excitation and a single collective surface vibration or two vibrations. As many microscopic models predict, the coupling to these *doorway* states causes a strong fragmentation of the resonance strength. This is the phenomenon of *collisional damping*, essentially connected with the coupling of giant modes to the quantal fluctuations of the nuclear surface.

The microscopic calculations that include the coupling to the $2p-2h$ configurations are successful in describing many properties of giant resonances. The microscopic description can be further extended by introducing more and more complex components such as $3p-3h \dots np-nh$. All modern transport theories include such a hierarchy of progressively more and more complicated levels of description [37–39]. However, the model space and the level of complexity of such approaches becomes so large, that one has to artificially truncate the model space using some selection rules. The computational power of modern computers is still not sufficient to treat this problem self-consistently and one is effectively limited to the very first step of the $2p-2h$ configurations.

2.2 Fine Structure and Characteristic Scales in the Nuclear Response

Investigation of the dominant damping mechanisms of giant multipole resonances is of paramount importance for unraveling their dynamical, intrinsic structure. Experimental verification of the above discussed and now widely-accepted *doorway picture* and of the dominant damping mechanisms of giant resonances still remains an open question. One of the most promising approaches to this long-standing problem lies in the phenomenon of fine structure in the nuclear excitation spectra and the related characteristic scales of fluctuations associated with the coupling between collective states and internal and external degrees of freedom. One expects a hierarchy of lifetimes and related, via the Heisenberg uncertainty principle, characteristic energy scales, starting from the typical scale associated

with short-lived collective states, the full width at half-maximum (FWHM) which is of the order of few MeV, going down to the scales characterized by the width of long-lived compound nuclear states which is of the order of few eV or even smaller. This hierarchy of couplings leads to the fluctuations in the observed strength, giving rise to the formation of the fine structure, as it is visualized in Fig. 2.4. In the case of strongly overlapping decay channels, one works in the regime of *Ericson fluctuations* [40, 41]. The appearance of fine structure itself was already observed for quite some time [23, 42] in the region of the ISGQR in ^{208}Pb . High-resolution ($\Delta E \simeq 50$ keV FWHM) electron scattering data obtained at DALINAC in Darmstadt revealed structures in the excitation energy spectrum, which clearly exceeded the statistical significance and could not be interpreted as pure statistical noise. As mentioned above, this phenomenon resulted in much debate concerning its physical nature, since at the same time the proton- or α -particle scattering experiments could not detect any fine structure. As soon as the necessary energy resolution could be achieved for the hadronic probes, the comparison of electron and proton scattering data demonstrated that the observed fluctuations are to a very large extent similar and are, therefore, physical in nature [43].

In order to characterize the properties of the observed fine structure and extract quantitative information out of a complex signal where several scales of different nature are mixed, a variety of methods were proposed so far, e.g. using a *doorway* model and microscopic calculations [44] or autocorrelation techniques [40, 41] assuming a statistical distribution of the decay channels [45]. The problem becomes

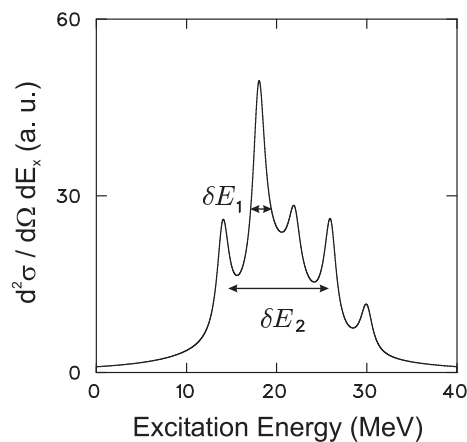


Fig. 2.4: Schematic representation of the fine structure formation out of a mixture of multiple scales of fluctuations.

especially difficult to treat when the number of scales in the fine structure is larger than two. This problem aside, the results provided by such methods remain dependent on underlying model assumptions. Therefore, one needs more elaborate and versatile tools to study the properties of these multiscale fluctuations. A few novel ideas for such analysis have been proposed recently. One representative example is a multifractal analysis [24–26] of the fluctuating strength function.

One of the most promising techniques so far is the entropy index method, which allows for the extraction of multiple scales of fluctuations from the excitation energy spectra [46]. This method has been successfully applied to the above-mentioned case of the ISGQR in ^{208}Pb . The extracted characteristic energy scales of fluctuations appeared to be independent of the exciting probe [27]. At the same time, the comparison to the second-RPA calculations for E2 response in ^{208}Pb demonstrated [47] that the observed scales indeed result from the first step of the coupling hierarchy, i.e. $1p - 1h$ to $2p - 2h$ states, thus proving its dominant role in the process of internal damping. This result has raised many new questions, in particular the following:

- Is fine structure of the ISGQR a global phenomenon, appearing also in other nuclei, or is this a peculiar feature of the doubly-magic ^{208}Pb nucleus?
- Does fine structure also appear in other resonances, e.g. GDR?
- What about magnetic giant resonances? The relative importance of escape and spreading widths in the spin-flip resonances, such as the Gamow-Teller (GT) and the spin-dipole resonance, may be quite different from that in the electric resonances.
- Are the observed scales characteristic to a nucleus or to a resonance, or can any generic behavior be revealed?
- What is the physical nature of observed scales?
- What is the role of the escape width?

A set of experiments was carried out at iThemba LABS, South Africa, with the aim of answering some of these questions by studying this phenomenon systematically in medium-heavy and heavy nuclei using high-resolution inelastic proton scattering. The next chapter outlines the experimental facility and techniques used to obtain such valuable experimental data.

3 High-Resolution Proton Scattering at iThemba LABS

The facility at iThemba LABS with its K600 high-resolution magnetic spectrometer is one of the two presently existing places in the world where hadronic reactions in the intermediate energy range (100 - 200 MeV/nucleon) with an energy resolution of $\Delta E/E \simeq 10^{-4}$ or better can be studied. This opens a variety of new exciting possibilities to address questions at the very forefront of current nuclear structure and astrophysical research. This chapter will introduce the accelerator facility and the experimental setup used for the high-resolution proton scattering experiments that constitute the main content of the present thesis.

3.1 Separated-Sector Cyclotron Facility

The inelastic proton scattering experiments on the investigation of the fine structure phenomena of the ISGQR took place at the National Accelerator Centre (NAC), recently renamed iThemba LABS (Themba means hope, and LABS stands for Laboratory for Accelerator Based Sciences), located in Somerset West, near Cape Town.

Figure 3.1 shows schematically the layout of the main accelerator together with related installations for various experiments and applications. A primary beam of protons and light ions can be produced and pre-accelerated by an injector cyclotron SPC1. Another injector cyclotron SPC2 with external ion sources is used for polarized protons and heavy ions. The heart of the facility is a separated-sector cyclotron (SSC), a four-sector machine with a sector angle of 34° . After injection into the cyclotron the particles start to gain energy while circulating in the RF and magnetic fields on the cyclotron orbits, the maximum proton energy gain per turn being about 1 MeV. At the exit high-energy beams of various ions can be extracted and used in a wide range of applications, like radioactive isotope production, or proton and neutron therapy for medical treatment of cancer patients. An intense program of fundamental nuclear physics research is also carried out at iThemba LABS (see e.g. [18, 48–54]).

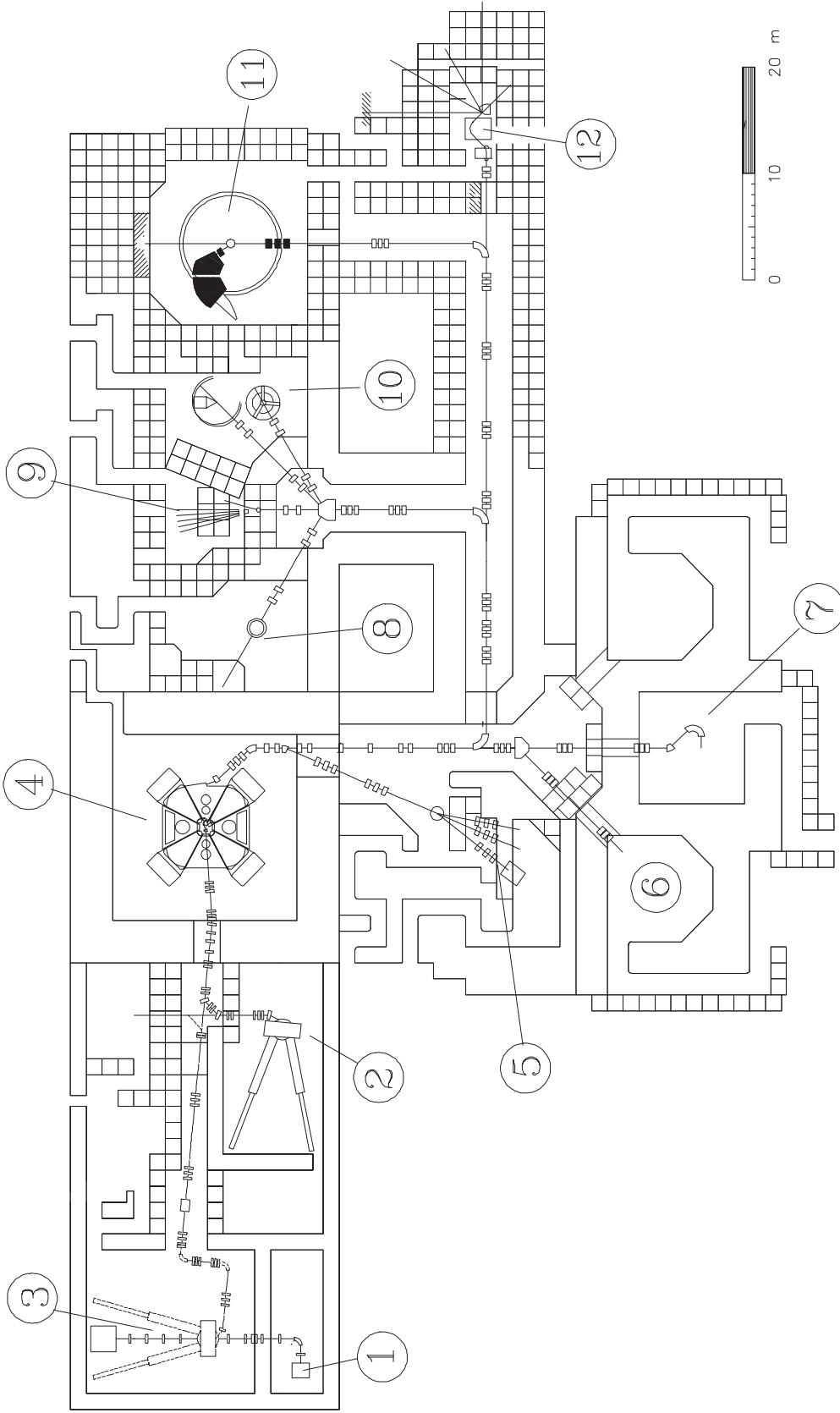


Fig. 3.1: The accelerator cyclotron facility at iThemba LABS: (1) ECR Ion Source, (2) SPC1 Injector Cyclotron, (3) SPC2 Injector Cyclotron, (4) Separated-Sector Cyclotron, (5) Radioactive Isotope Production, (6) Proton Therapy, (7) Neutron Therapy, (8) Experiments with Charged Particles, (9) Experiments with Neutron Beams, (10) γ -Spectroscopy, (11) K600 magnetic spectrometer, (12) Beam Swinger Magnet.

3.2 The K600 Magnetic Spectrometer

For the present experiment a proton beam with an energy of 200 MeV and currents between 5 and 20 nA was provided by the SSC and delivered to the experimental hall of the K600 magnetic spectrometer. The spectrometer layout is shown in detail in Fig. 3.2. A proton beam from the accelerator enters the scattering chamber (1), at the center of which is a set of targets put on a target holder. For measurements at small scattering angles an internal Faraday cup (2) is used as a beam dump. At larger angles one can use an external beam dump (3). Protons scattered off the target are collimated by one of the collimators installed on the carousel (4) which define the solid angle. The protons then pass through the ion-optical system of the K600 spectrometer. It is a QDD-type horizontal-bending, focussing magnetic spectrometer for protons and other light ions of intermediate energy. Its optical system consists essentially of a sextupole magnet (5), a quadrupole magnet (6) for vertical focussing, and two horizontally-bending dipole magnets (7) and (9), each having its own focussing coil, the so-called K- and H-correction coils (8) and (10). The K-coil is a quadrupole focusing element, used to adjust for first-order kinematical variations of momentum with angle [55]. The H-coil is a hexapole focusing element to correct for second-order aberrations.

The particles are focused on the focal plane of the spectrometer, where a detector system is placed (see Fig. 3.3), consisting of three multiwire drift chambers (12). The particle momentum is analyzed by the X-chambers with 198 vertical signal wires along the dispersive direction. A Y-chamber, having 16 horizontal wires, is used for monitoring the vertical beam alignment. Two paddles of 3.2 mm and 12.7 mm thick plastic scintillators, located behind the drift chambers, serve as a trigger and a particle identification detector. The design of the K600 magnetic spectrometer at the iThemba LABS essentially follows the one previously used at the Indiana University Cyclotron Facility (IUCF) [56, 57]. It can be operated in three modes of (A) low, (B) medium, and (C) high dispersion. The spectrometer settings were optimized for the medium dispersion mode (B) with 200 MeV protons, covering an excitation energy bite of about 23 MeV. With these settings the full excitation energy range of interest could be recorded within a single measurement, while still providing sufficient resolution at the focal plane. Some important parameters of the K600 spectrometer are summarized in Table 3.1.

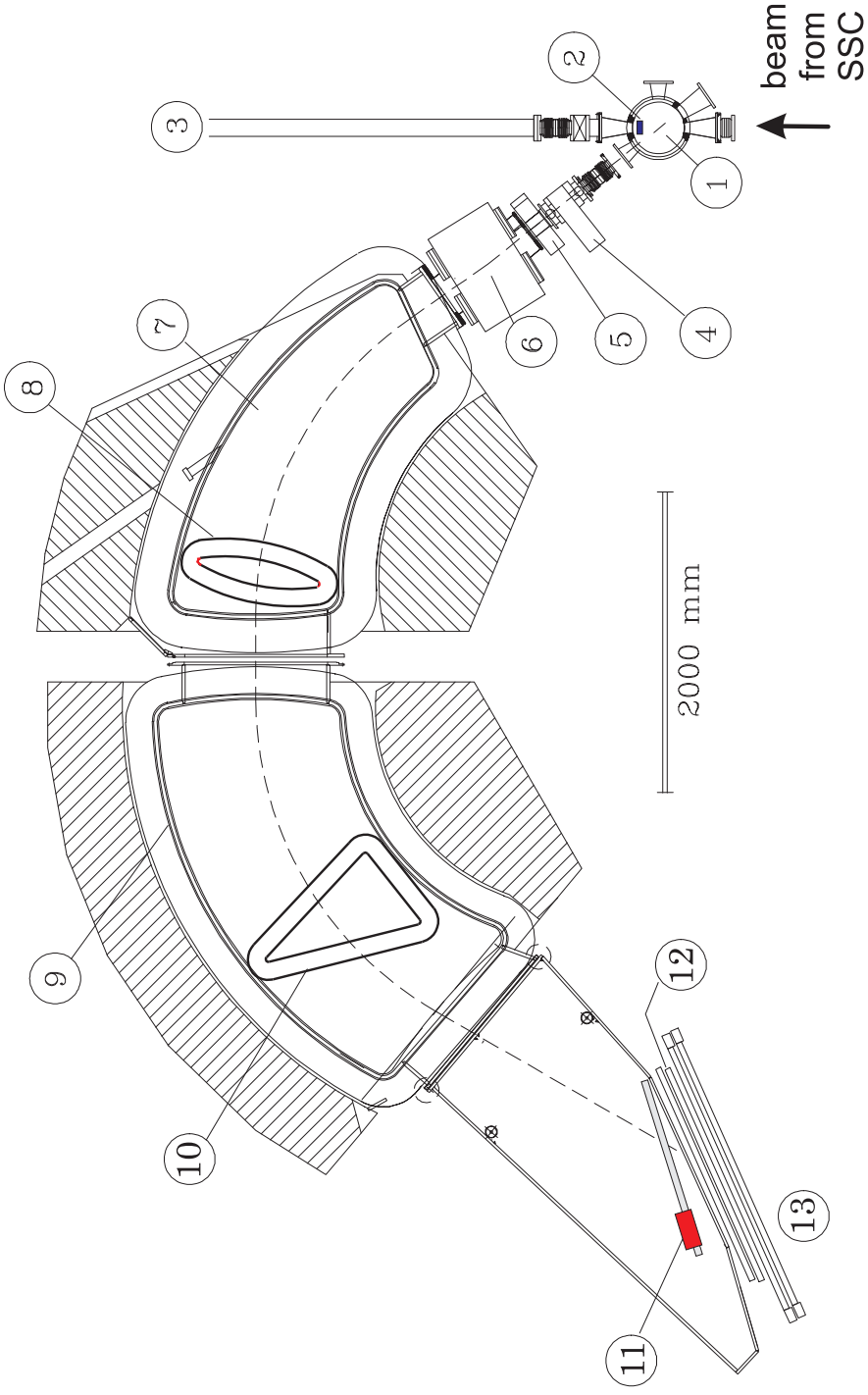


Fig. 3.2: Plan view of the K600 high-resolution magnetic spectrometer at iThemba LABS: (1) scattering chamber with targets, (2) internal Faraday cup for small-angle scattering experiments, (3) beam line to external beam dump, (4) set of collimators, (5) sextupole magnet, (6) quadrupole magnet, (7) first dipole, (8) H-correction coil, (9) second dipole, (10) K-correction coil, (11) focal plane beam blocker for decreasing count-rate from elastic line, (12) vertical drift chambers for momentum determination and a horizontal drift chamber for monitoring the Y-position of the beam, (13) scintillator paddles as trigger detectors.

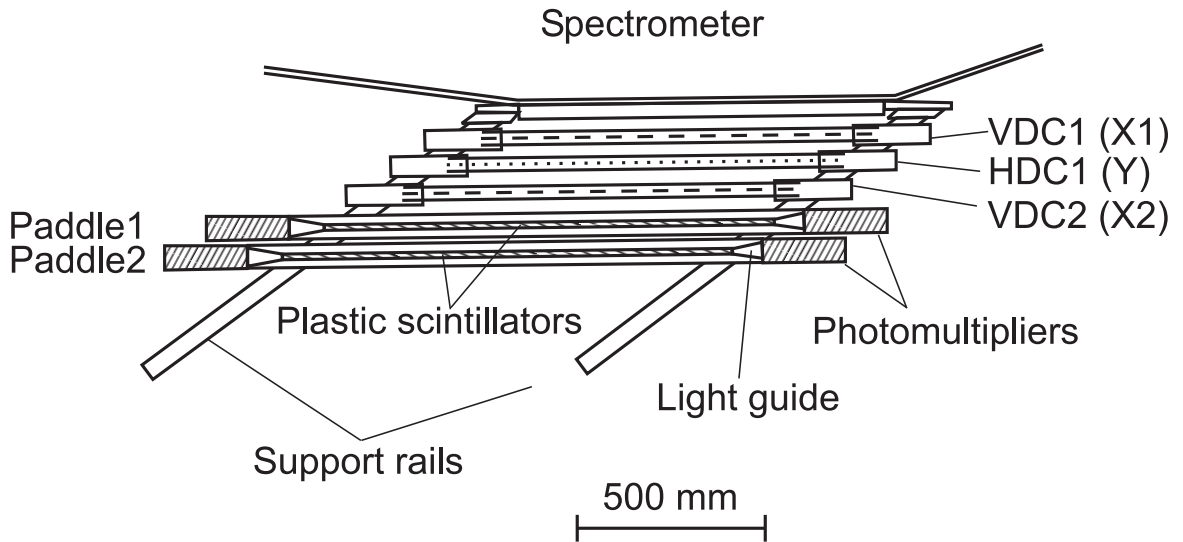


Fig. 3.3: Plan view of the K600 focal-plane detector system.

Tab. 3.1: Parameters of the K600 magnetic spectrometer

| Parameter | Value |
|---|--------------|
| Resolving power (for 0.6mm object slit) | 28000 |
| Horizontal acceptance (mrad) | ± 44 |
| Vertical acceptance (mrad) | ± 44 |
| Max. solid angle (msr) | 6 |
| Dispersion (cm/%) | |
| - mode A | 9.8 |
| - mode B | 8.1 |
| - mode C | 6.2 |
| Mean radius of central ray (cm) | 210 (mode B) |
| Maximum rigidity (T·m) | 3.6 (mode B) |
| Maximum proton energy (MeV) | 520 |
| Length of the focal plane (cm) | 78 |

3.3 Dispersion Matching Techniques

The full capabilities of a magnetic spectrometer can only be achieved if the characteristics of the beam are matched to the requirements of the spectrometer by a proper adjustment of the beam-line optics. The methods of matching beam properties to the specific spectrometer focussing conditions allow the compensation for line-broadening effects caused by the beam momentum spread. This is particularly important for the class of experiments like the ones presented here, where the highest possible energy resolution is aimed for.

The special design of the beam line at iThemba LABS allows for a so-called *lateral momentum dispersion-matched mode* to be realized. The principle of momentum dispersion matching is shown schematically in Fig. 3.4 and requires adjustment of the beam dispersion, emittance and spot size at the target using beam-line focussing and steering elements to match with the ion-optical properties of the spectrometer. In the conventional *achromatic* mode (left panel of Fig. 3.4), the beam is focussed to a point at the target. If the beam particles are not monoenergetic, but have some energy spread, then the rays having slightly different momenta will be focussed by the magnetic field of the spectrometer to different points in the focal plane and they will cross it at slightly different angles. The image resolution in such a case will be affected by the initial momentum spread of the beam. In order to achieve a better resolution, momentum dispersion matching techniques can be applied. In the *lateral dispersion matching* mode (middle panel of Fig. 3.4) one adjusts the dispersion of the beam on the target in a such way that the rays of different momenta traverse different path lengths through the magnetic field, and are focussed back on the focal plane at one point, thus providing better image resolution, almost unaffected by the residual spread of the primary beam energy. There exists also a third possibility, the so-called *angular dispersion* (right panel), when the primary beam is delivered to the target not only with a certain dispersion, but also having an angular convergence. All particles scattered through the same angle then cross the focal plane not only in the same point, but also under the same angle. This technique allows for the improvement in the angular resolution, which is of crucial importance for zero-degree scattering experiments [58].

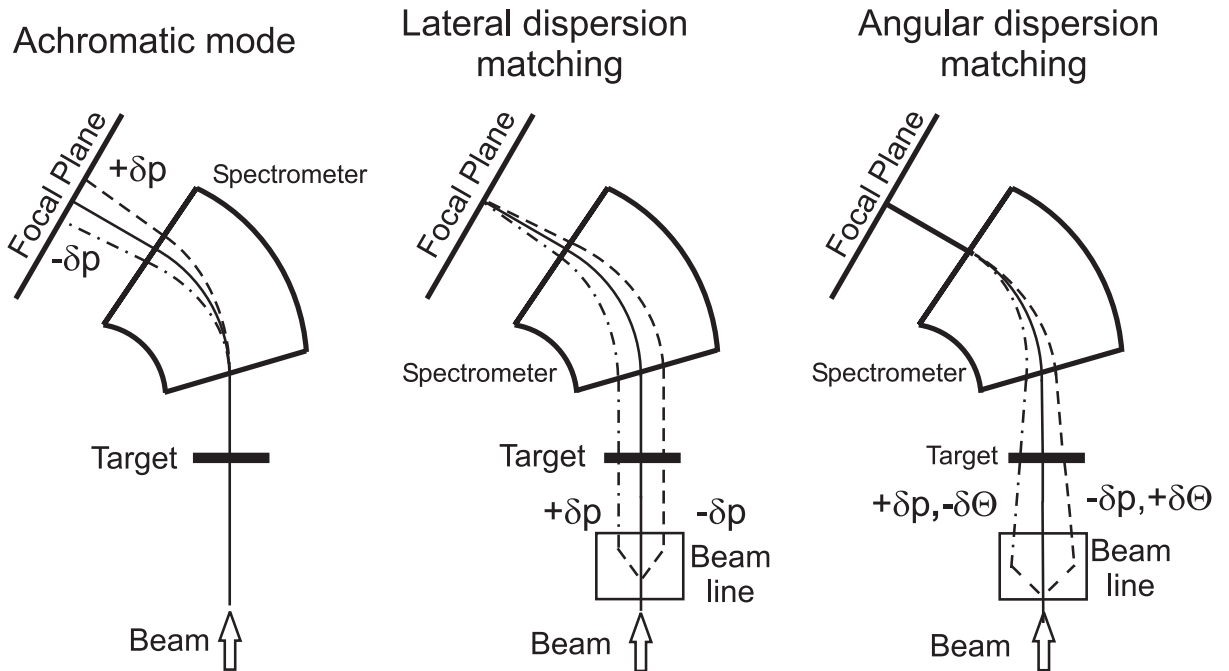


Fig. 3.4: Dispersion matching techniques. In the *achromatic* mode (left panel), the position and the angle of scattered rays at the focal plane depend on the initial beam energy spread, which thereby limits the resolution. The *lateral dispersion* mode (middle panel) makes it possible to improve the resolution by spatially spreading the beam spot on the target according to the beam dispersion, matching it with the focussing properties of the magnetic spectrometer. A further improvement can be achieved in an angular dispersion mode (right panel), when additionally the angles of incoming rays at the target are matched accordingly so that the focal plane position and angle are not affected by the initial beam energy spread.

4 Experiment

During three weekends of beam-time in September/October 2001, inelastic scattering experiments of 200 MeV protons were carried out for a wide mass range of targets of closed and near-closed shell nuclei, ^{208}Pb , ^{120}Sn , ^{90}Zr , ^{89}Y , and ^{58}Ni . In proton scattering, one can excite a certain kind of multipole modes rather selectively, by choosing appropriate kinematic conditions. The scattering angles were selected to match the maximum of the cross sections for $\Delta L = 2$ excitations in the corresponding targets, thereby exciting predominantly the ISGQR under investigation. Additionally, for two selected examples (^{90}Zr and ^{208}Pb), measurements were taken at angles above and below the maximum of the $\Delta L = 2$ angular distributions in order to estimate the effects of the mixing of different multipoles in the cross sections.

In October 2003 another set of experiments took place, and the excitation energy spectra for two more target nuclei ^{166}Er and ^{142}Nd were taken in the maximum of the $\Delta L = 2$ cross section. The information on all the targets and scattering angles used is summarized in the Table 4.1.

Tab. 4.1: Summary of information on the targets and scattering angles used.

| Target element | Angles (deg.) | Density (mg/cm ²) | Enrichment (%) |
|-------------------|----------------|-------------------------------|----------------|
| ^{208}Pb | 6, 8, 10, 12.5 | 0.74, 6.0 | >98 |
| ^{166}Er | 8 | 1.8 | >95 |
| ^{142}Nd | 9 | 1.49 | >95 |
| ^{120}Sn | 8 | 4.5 | >95 |
| ^{90}Zr | 9.2, 11, 13 | 10.1 | 97.7 |
| ^{89}Y | 9.2 | 1.9 | >95 |
| ^{58}Ni | 10 | 3.0 | >95 |

4.1 Experimental Procedure

Before taking data, a special procedure of adjusting the offsets and threshold settings of the time-to-digital converter (TDC) modules of the drift chambers was carried out, to ensure reliable timing information from each wire. At the beginning of the assigned beam time period, the proton beam was delivered in the achromatic mode to the scattering chamber at the K600 spectrometer. A test run with a thin ^{208}Pb target was performed to check the operation of the spectrometer and the detector system, as well as the data acquisition system. The energy resolution at this stage was in the range of 100 keV. A spectrometer setting for the mid-point of the focal plane corresponding to an excitation energy of 50 MeV in ^{208}Pb was then chosen. At this setting, the cross section is essentially constant and the measured spectrum resembles the features of a 'white spectrum'. The data served to calibrate the time-to-distance conversion table, as described in [59]. This table is used to obtain drift lengths of secondary particles to the corresponding wires from the measured drift times. With such information it is possible to calculate the focal-plane crossing position and the angle of the scattered proton by a linear regression from the obtained drift distances. After this step, the beam dispersion matching was realized. For an approximate setting of the beam-line elements, calculations with the ray-tracing simulation programs TRANSPORT and TRACK [60] were used, taking into account not only the whole beam transport system, but also the actual experimentally measured field map inside the K600 spectrometer. Although there was no any direct tool to confirm the realization of perfect matching conditions in the first experiment, the procedure gave a significant (factor of two) improvement in the resolution.

A unique possibility to achieve dispersion matching conditions is provided by the so-called *faint beam method*. The intensity of the incoming beam is reduced by several orders of magnitude by inserting meshes in the beam line between the ion source and the injector cyclotron. It allows the magnetic spectrometer to be positioned at zero degrees and the incident beam be observed directly with the focal-plane detector system. This method, first realized at RCNP [61], has been later successfully implemented at iThemba LABS, and realized for the first time in the 2003 experimental campaign, proving the validity of the approach utilized here, based on the predictive power of the ray-trace simulations.

For monitoring the energy resolution, a thin ($740 \mu\text{g}/\text{cm}^2$) ^{208}Pb target was used and small adjustments of settings of the K- and H-coils and the group of quadrupole magnets in front of the scattering chamber were performed, in order to achieve the smallest width for the elastic line and low-lying prominent transitions. A typical value of $\Delta E = 30 \text{ keV}$ FWHM was achieved. A 1° wide vertical slit-collimator at the entrance of K600 spectrometer was used, which defined the solid angle of the spectrometer $\Delta\Omega_p = 1.3 \text{ msr}$.

Before starting the actual data taking, the beam position on the target was checked using a Al_2O_3 scintillating target with a hole of 3 mm in diameter in its center. Steering elements immediately in front of the scattering chamber were adjusted so that the beam passed exactly through the hole. Additional background optimization was achieved by minimizing the count rates in the scintillator paddles of the detector system when slightly adjusting the beam position. Afterwards, background from beam halo was monitored using an empty frame target, and when necessary, the beam was readjusted to obtain the smallest possible counting rate in the drift chambers from the halo background. In some cases all of these steps had to be repeated iteratively, to ensure a minimum contribution of the experimental background to the spectrum and provide the best possible resolution.

Once these preparations were attended to, the process of collecting experimental data could begin. The events from elastic scattering were then cut off by moving a brass block in the in the vacuum chamber in front of the focal plane such that the count rate from the elastic line disappeared completely. This reduced the data rates by a factor of 10^3 . In order to achieve sufficient statistics in the spectrum region of giant resonances, approximately 12 hours per angle setting per target were required. A typical data acquisition run lasted for 2 hours and was followed by another background check with an empty frame measurement, after which a next data run was started. Because of the instabilities of the cyclotron and long measuring periods, the resolution of 30 keV could not be maintained during the experiment, so that on average the full-statistics spectra show resolution of 35 to 50 keV (FWHM). The stability of the magnetic fields of the K600 dipoles was monitored throughout the experiment by means of two NMR probes, and was shown to be sufficient to avoid an extra contribution to the energy resolution.

4.2 Data Acquisition and Online Analysis

The timing and energy signals from the detectors were processed by standard NIM and CAMAC fast electronics. The data acquisition electronics used during the experiment is schematically shown in Fig. 4.1. The main steps of the data acquisition process are as follows. An event trigger is started after a coincidence between the two scintillator paddles is established. Each scintillator paddle has two photomultipliers, at opposite ends. After extraction of the time information with a constant-fraction discriminator (CFD), the signals from the opposite photomultipliers of each paddle are fed into a mean-timer, which serves to provide independence of the timing of the trigger signal from the intersection point in

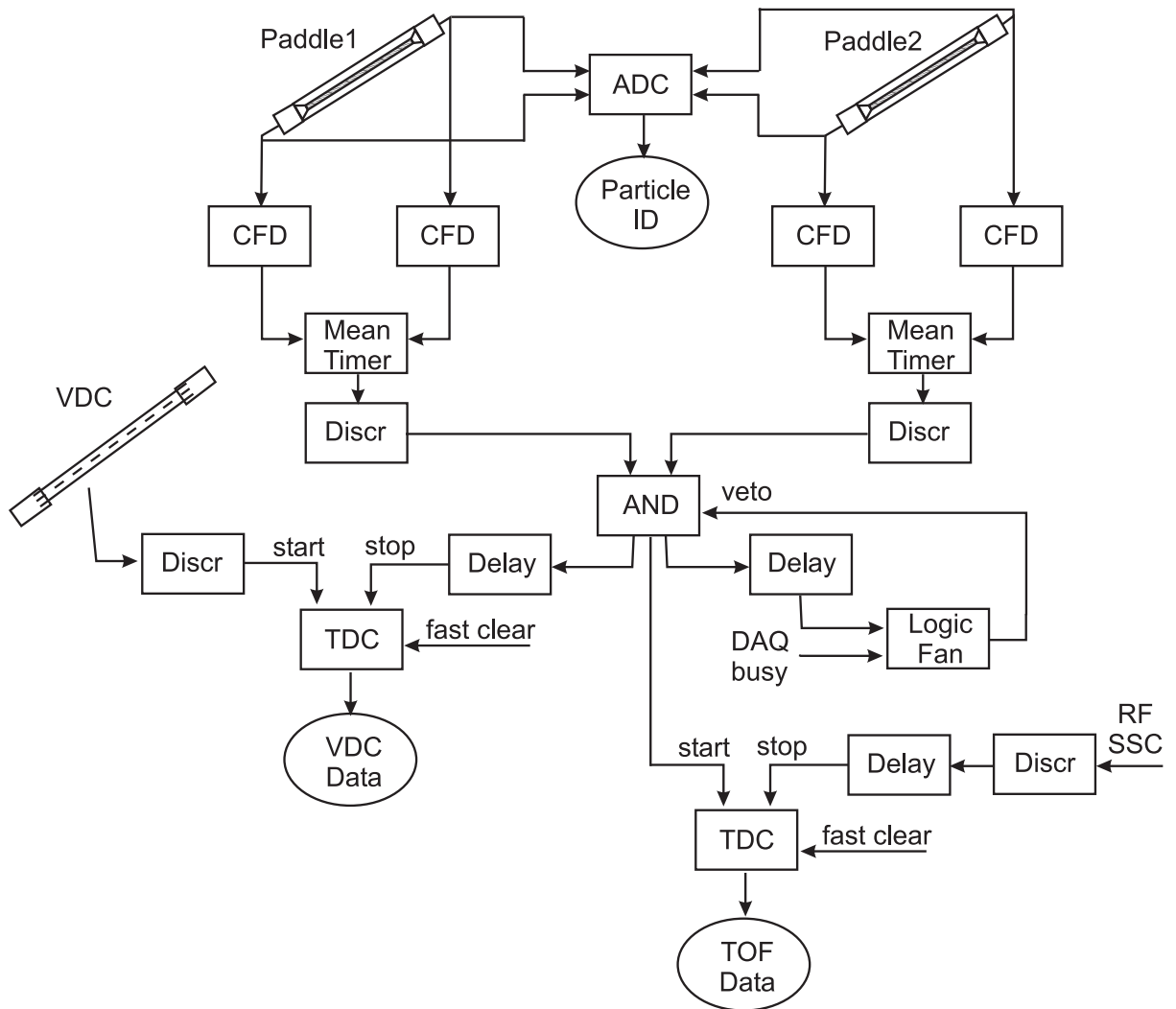


Fig. 4.1: Schematic view of the data acquisition electronics used in the experiment.

the focal plane. This signal is then used as a start for the time-of-flight (TOF) measurement. The signal from the cyclotron's RF system serves as a stop signal. The spectrum with the distribution of TOF values is later used to suppress events that are not correlated with the beam pulse. Additionally, the pulse heights from each scintillator paddle are digitized for the purpose of particle identification.

Each signal wire of the multiwire drift chambers is connected to its own pre-amplifier, discriminator and a separate channel of the time-to-digital converter (TDC) module. When a signal is registered on a signal wire, the corresponding TDC counter is started and a delayed paddle coincidence trigger signal serves as a common stop for all the channels, thereby providing the drift-time information for each activated drift cell. All these data are then passed via a VME front-end [62] to a VAX data acquisition computer and in parallel to a tape storage device. A VAX/VMS 4000 workstation was used for data acquisition and online analysis using the XSYS software [63, 64].

For the online analysis, a simplified algorithm of track reconstruction was used and only some basic spectra were collected for monitoring purposes. The dead time of the data acquisition system was determined with a standard technique by inhibiting the current integrator scaler with a busy signal from the data acquisition system. As the goal of the present experiment was the investigation of fine structure in the spectra rather than absolute cross section measurements, the data were taken with high beam currents of up to 25 nA, for the sake of good statistics. The resulting dead time values of up to 20% were considered acceptable.

4.3 Offline Data Analysis

For the offline analysis the same XSYS software package was used. However, the analysis algorithm was significantly improved producing a much more precise track reconstruction, smaller background, and better excitation energy resolution. A schematic of the offline data processing algorithm is presented in Fig. 4.2. The discussion of the different steps of the analysis is supplemented by the corresponding figures, serving as examples. First, one has to distinguish between protons and other charged particles detected by the spectrometer. Particle identification

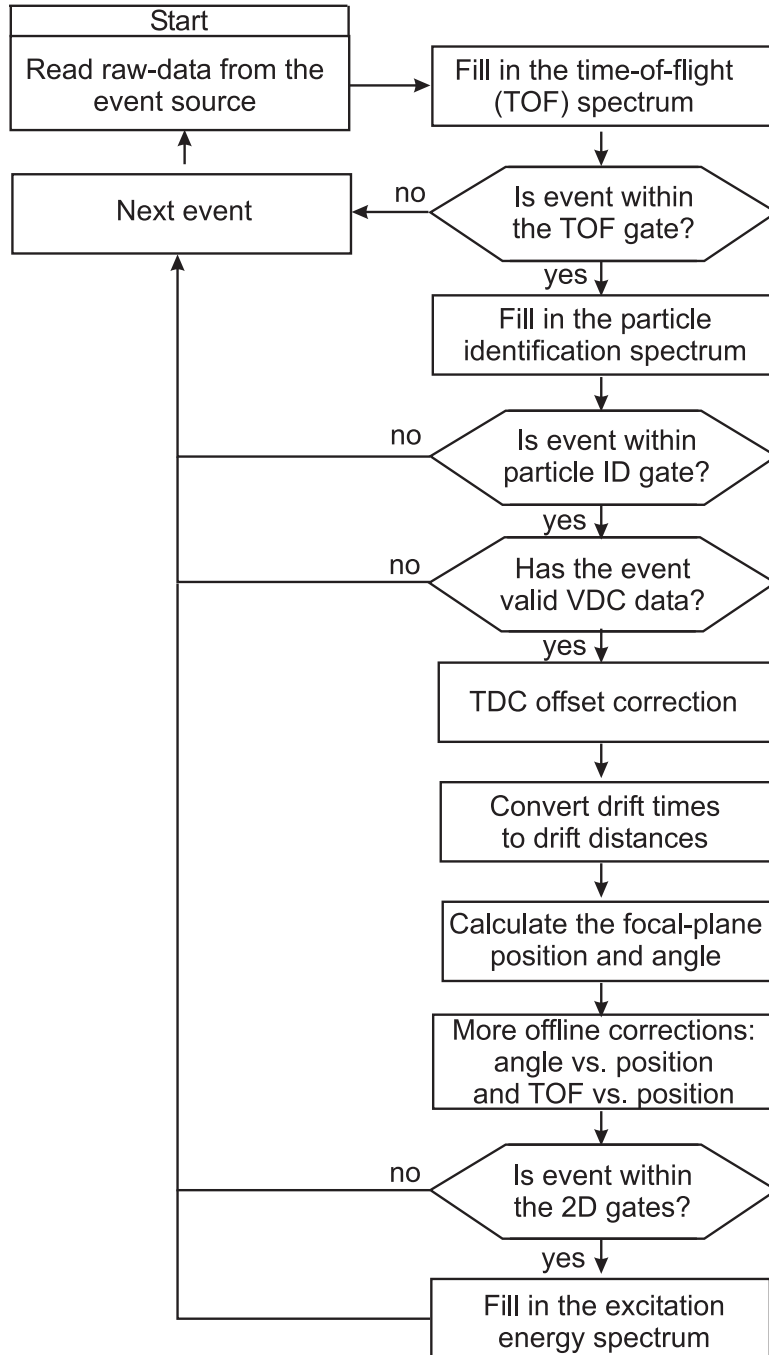


Fig. 4.2: Algorithm of the offline raw data analysis routine.

can be achieved via particle time-of-flight (TOF) information and independently via the energy-loss spectrum in the scintillator paddles. It was shown in ion-optical simulations [48] that one can clearly separate protons from other charged particles by looking at the time interval between the actual particle scattering off the target, and its arrival at the focal plane. In practice, one starts the TOF measurement by the signal from the scintillator paddles and stops it using a delayed signal from the radio-frequency (RF) system of the cyclotron accelerator.

Such a TOF spectrum is shown in Fig. 4.3. One can clearly see a proton peak superimposed on the flat background of other uncorrelated events. To select the proton events one sets a gate in the analysis software on this peak, shown by the dashed lines in Fig. 4.3. At a later step, the validity of the drift-chamber data is checked. If one plots the TOF-spectrum for valid VDC events only (the bottom histogram of Fig. 4.3), then one can see that the background has disappeared.

Another method for identifying different charged particles is realized using the signals from the scintillator paddles. The energy deposited by a charged particle in the scintillator material depends on the particle charge and kinetic energy. This energy is then converted to a proportional amount of light in the scintillator. Therefore, by digitizing the signals from the photomultipliers using analog-to-digital converters (ADC) one obtains a measure of the energy-loss of the particle ΔE in the scintillator paddles. In order to eliminate the pulse height dependence on the position along the scintillator, an average of the two values from the opposite photomultipliers was taken. Figure 4.4 presents a 2D distribution of events

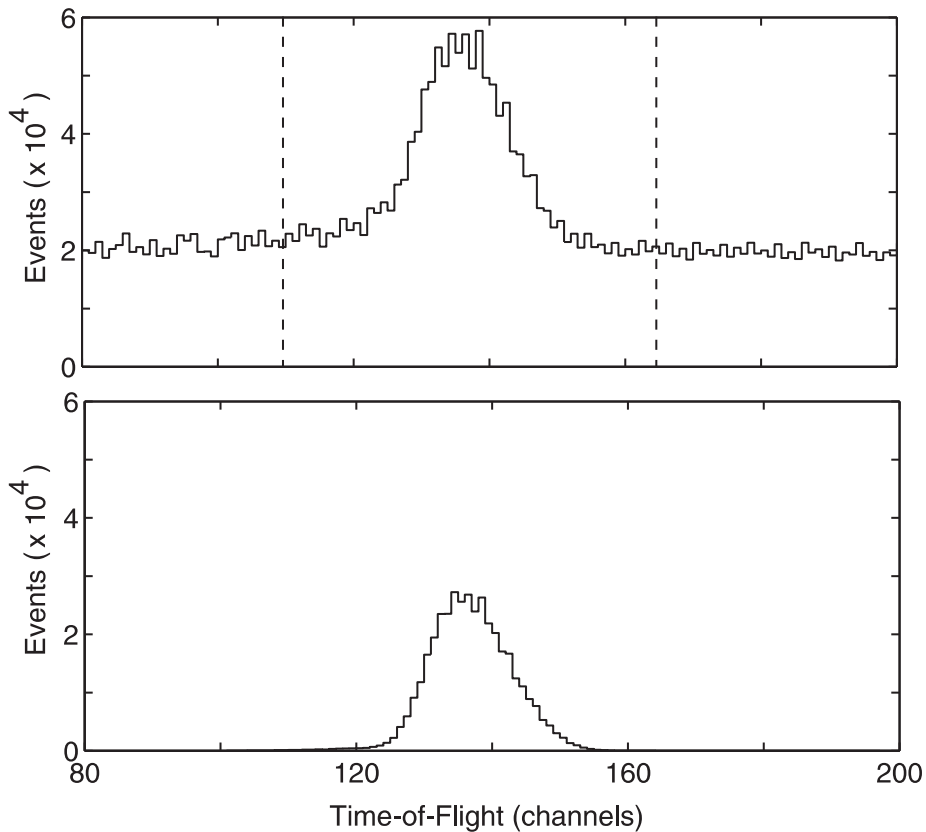


Fig. 4.3: Time-of-flight spectrum for all events (top) and for events with valid VDC data (bottom). The dashed lines show the gates for selecting proton events.

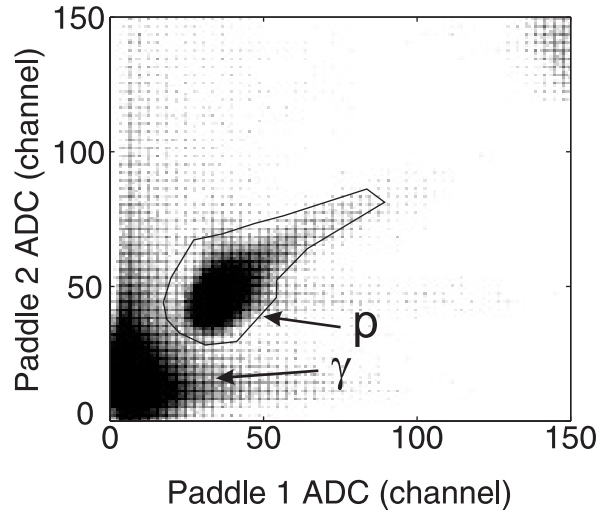


Fig. 4.4: Particle identification spectrum, produced by the ΔE signals from the scintillator paddles 1 and 2. Proton events can be clearly identified.

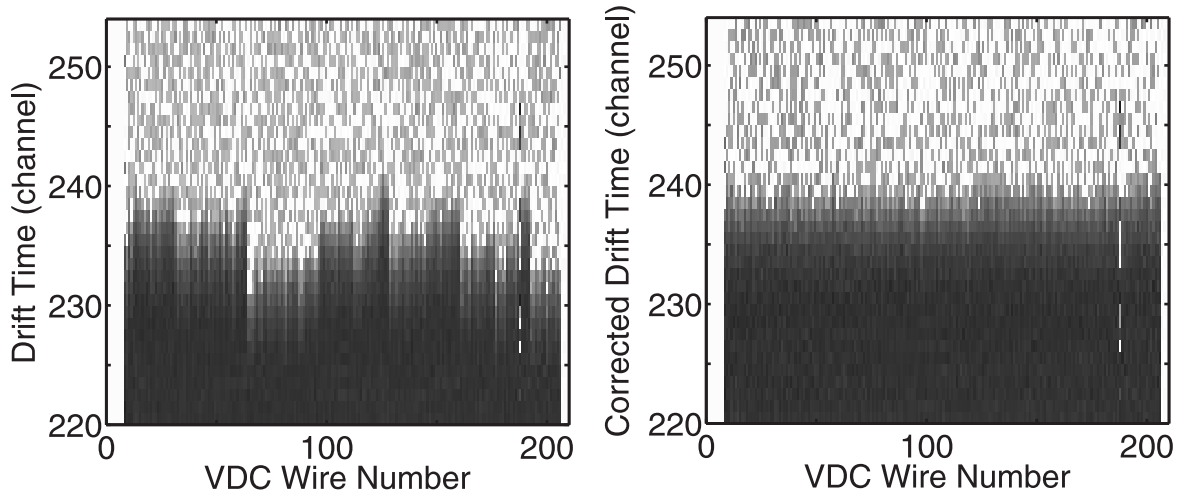


Fig. 4.5: Drift time offset adjustment for each wire of the VDC. Left: original drift time distribution. Right: the same after offset adjustments.

according to their energy losses ΔE_1 and ΔE_2 in the first and second paddles. Proton events are localized and can be easily separated from other background contributions by putting a suitable gating condition in the analysis software, as shown in the figure.

In the next step, the drift times from the VDCs have to be converted into absolute values of drift distances using a look-up table. Although the so-called 'autotrimming' procedure was utilized in order to align the offsets of all TDC channels, the distribution of drift times during offline replay of raw data (left panel of Fig. 4.5) still shows large deviations from a straight line. This may result in an incorrect

position reconstruction and artificial structures in the spectra. Therefore, an additional software offset correction for each TDC channel was implemented into the offline analysis. The right panel of Fig. 4.5 displays the results of such an offset correction.

After that, the integrity of the drift chambers raw data was tested. A valid event should have not less than 3 and not more than 9 wires hit. The drift times associated with these wires must be within a specific allowed range. Up to two missing wires in one event are allowed if the number of wires hit is sufficient for the reconstruction. Drift time values should follow in such an order, that one can assign a track unambiguously to the corresponding drift distances. Then, the position of the crossing point in the focal plane along the dispersive direction is determined using the drift distances and wire-position coordinates. The slope of the trajectory should also fit into a certain range of values, constrained by geometrical considerations.

Next, the scattered-particle focal-plane position and angle spectra are generated. To achieve the best position resolution, one has to do further offline corrections. For this purpose, additional 2D distributions of events as a function of position, angle, and time-of-flight are constructed. Figure 4.6 shows as an example correlations between the position of the particle in the focal plane and its time-of-flight (left plots). The excitation energy region of the first excited state in ^{208}Pb is shown. One can see that the distribution of raw data is not straight, but slightly tilted. Using the polynomial correction function of 3rd order, one can make it straight, as shown in the bottom-left panel, thereby improving the resolution. A similar procedure can be performed for the position-vs.-angle distribution, as demonstrated in the right part of Fig. 4.6, leading to a further improvement in the resolution.

This plot can also be used for the identification of possible instrumental background sources in the data. Thus, Fig. 4.7 shows the position-vs.-angle distribution over the whole focal plane for one run on the ^{208}Pb target. Note that the excitation energy increases to the left with decreasing channel number. One can identify several excited states. The elastic scattering line should have appeared at the rightmost position, however, it was suppressed by the focal-plane beam blocker. Nevertheless, a small part of elastically scattered protons did rescatter

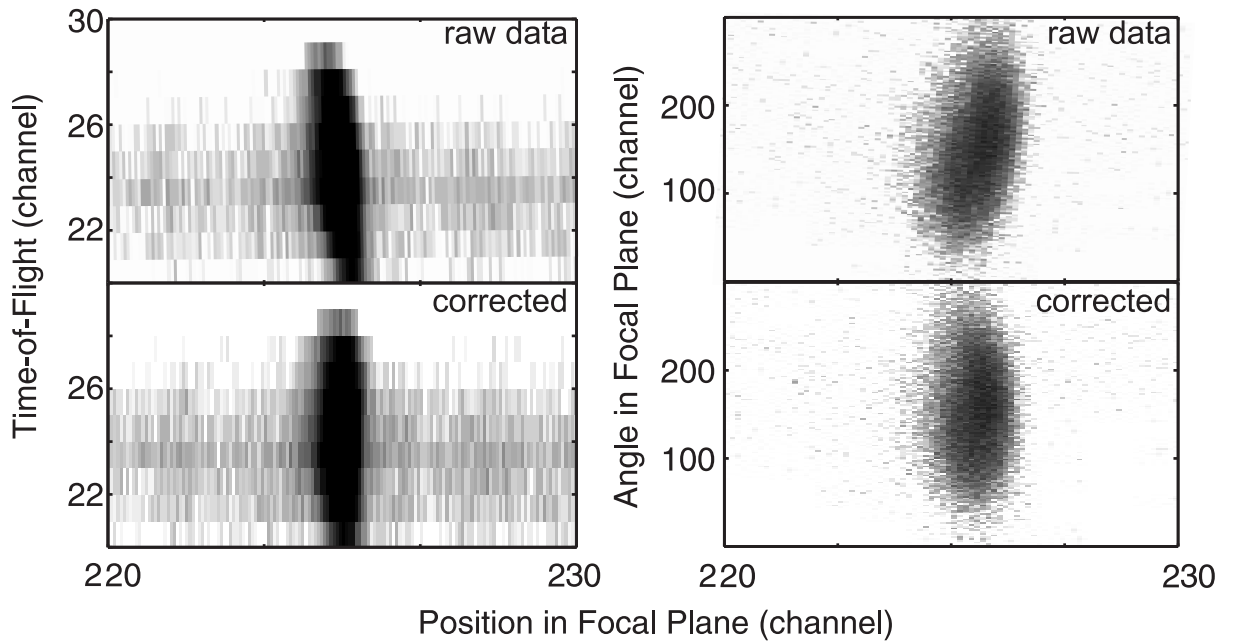


Fig. 4.6: Distribution of events from the ^{208}Pb reaction at energies around the first excited state as a function of the position in the focal plane and of either the time-of-flight (left) or focal-plane angle (right) of the particle before (top) and after (bottom) application of position corrections. Shown is the magnified region of the first excited state in ^{208}Pb .

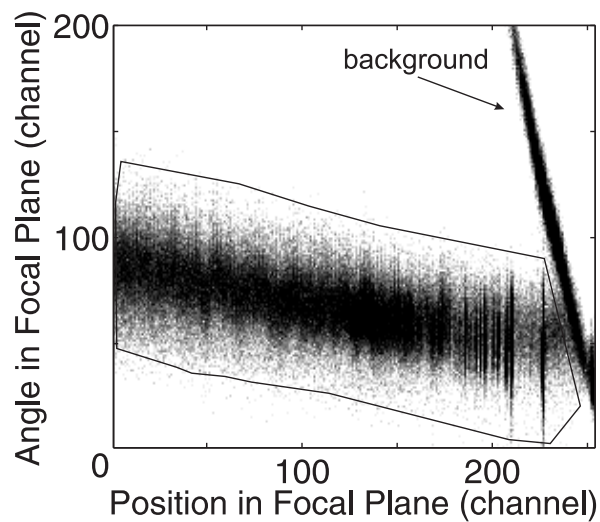


Fig. 4.7: Full distribution of events over the position and the angle in the focal plane of the spectrometer. One can identify a background caused by rescattering of protons on the focal-plane beam blocker (see Fig.3.2). A closed-polygon line denotes the gating condition for filtering out the background.

on it and passed into the detector system at a different point and angle. These events show up as a tilted line, going across the focal plane. Using suitable gating condition (like the one shown in Fig. 4.7 by a closed polygon line) one can still remove this background contribution from the final spectra. Finally, the particle momentum and excitation energy spectra were calculated using the information from several identified states in the spectra and information from the ^{12}C target calibration run. Afterward one proceeds to the next event.

It was observed that because of accelerator instabilities and drifts the energy resolution was degrading slowly with time. Therefore, for an additional improvement of the resolution in the offline analysis, long runs were divided into several subruns, which were energy-calibrated separately and later merged back into a single spectrum. This resulted in a gain in resolution of several keV.

4.4 Measured Spectra

The final spectra obtained after summing up all the data for a given target and angle are presented in this section. The excitation energy spectrum of ^{208}Pb measured at $\theta = 8^\circ$ is presented in Fig. 4.8, compared to the (e,e') data from the DALINAC [23], and proton scattering data from IUCF [65], discussed in the introduction, and having a comparable energy resolution. One can see that, indeed, similar structures are observed in all three experiments. Figure 4.9 shows the same excitation spectrum in ^{208}Pb at 8° for three excitation energy ranges, the upper part representing the global overview of the whole spectrum, whereas the lower left- and right-hand side plots magnify the region of the ISGQR and the high-excitation energy region, respectively. The difference is striking, pointing to the physical nature of the former due to the presence of several energy scales, and the statistical nature of the latter.

It is also interesting to reverse the time perspective and compare to results of pioneering experiments demonstrating the prominent excitation of the ISGQR in the (p,p') reaction, to see the advances that have been made due to the development of experimental techniques. Such a retrospective view can be seen in Fig. 4.10, where the two excitation energy spectra of the $^{90}\text{Zr}(p,p')$ reaction under similar

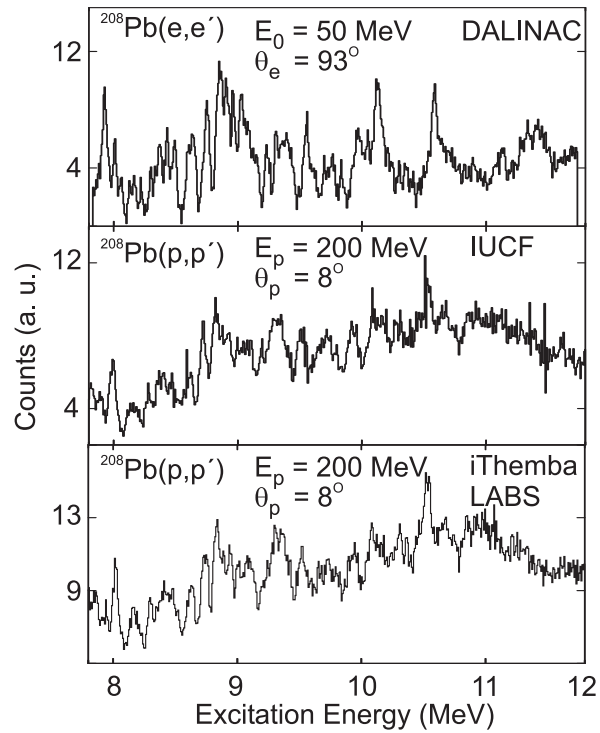


Fig. 4.8: Similarity of the structures observed in the three experiments on ^{208}Pb carried out in Darmstadt (upper part) [23], at IUCF (middle part) [65], and recently at iThemba LABS (bottom part).

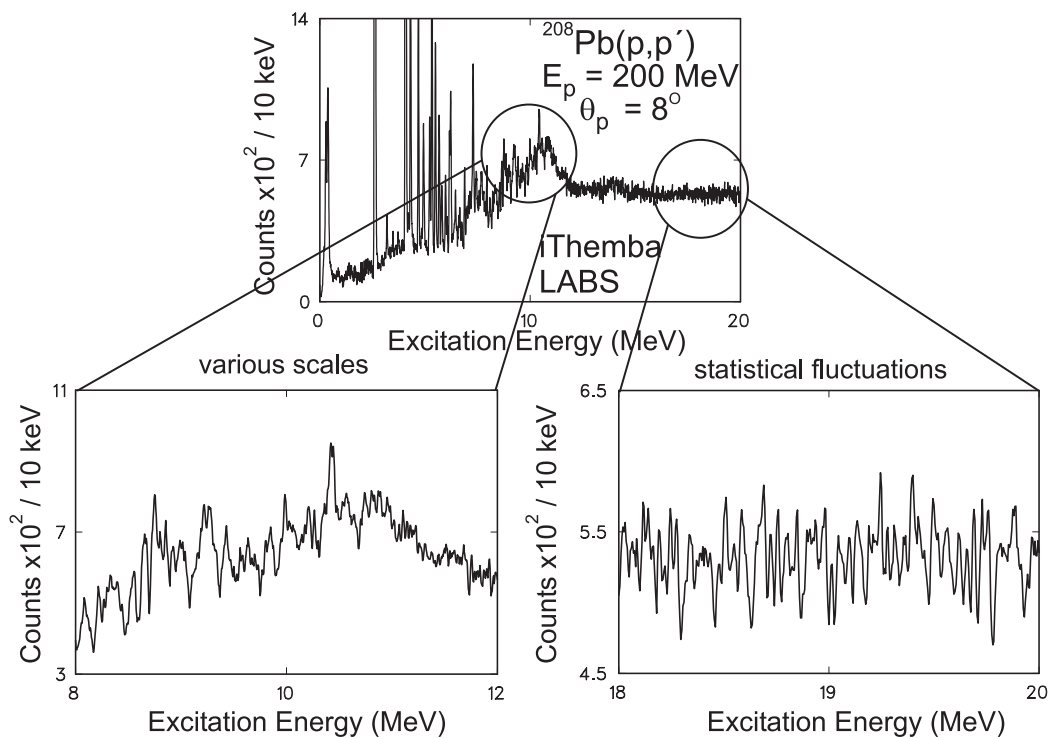


Fig. 4.9: Different modes of fluctuations in ^{208}Pb nucleus observed at different excitation energy ranges.

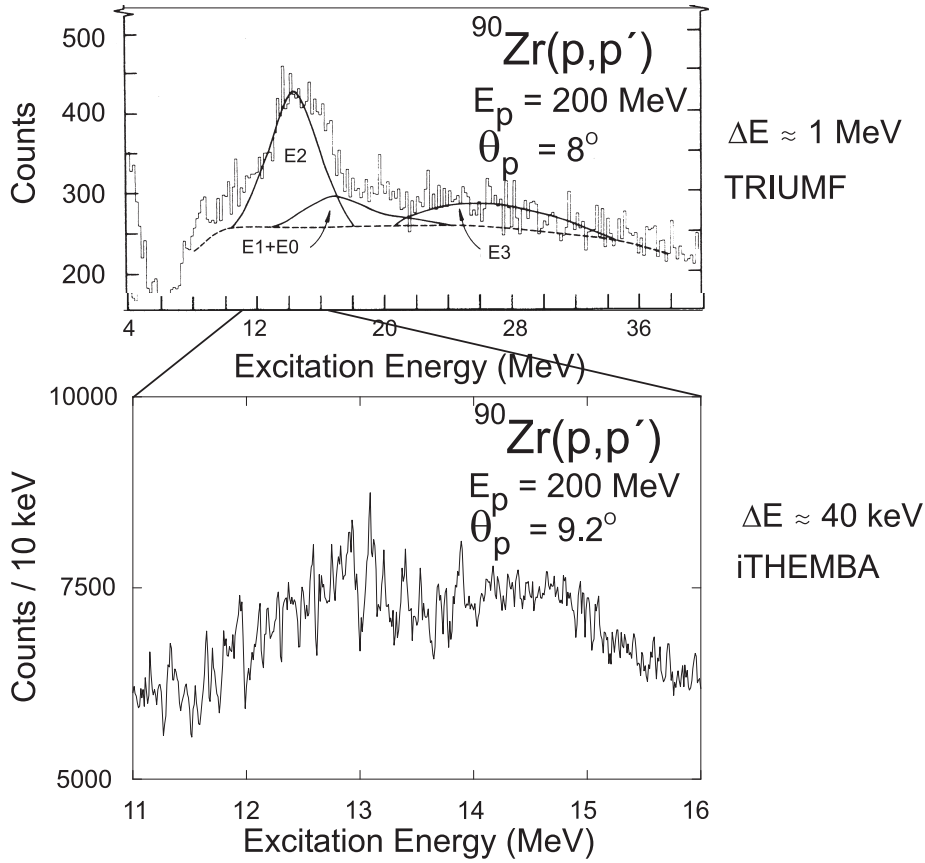


Fig. 4.10: Comparison of a pioneering (p,p') experiment on the ISGQR in ^{90}Zr by Bertrand et al. [66], with the recently obtained high energy resolution data at iThemba LABS under similar kinematics. A broad bump in the upper spectrum around 14 MeV is interpreted as the GQR. The resolution of 1 MeV is insufficient to observe any detailed structure. When measured with high energy-resolution, the GQR region expanded in the lower part exhibits fine structure, and a double-hump structure deviating from the typical assumption of a single Lorentzian.

kinematic conditions are shown. The upper part shows the old data by Bertrand et al. [66] measured with 1 MeV resolution. Underneath are the recent iThemba LABS data. The improvement of the energy resolution from 1 MeV down to 40 keV FWHM brings a qualitatively different picture, resolving subtle effects of the GQR in an atomic nucleus of ^{90}Zr . With such a high energy resolution one can observe fluctuations of different strengths and scales. Another spectacular feature of the new data is that the resonance bump does not have a Lorentzian form (as assumed in all analysis of hadronic scattering data), but has a rather fragmented double-hump structure.

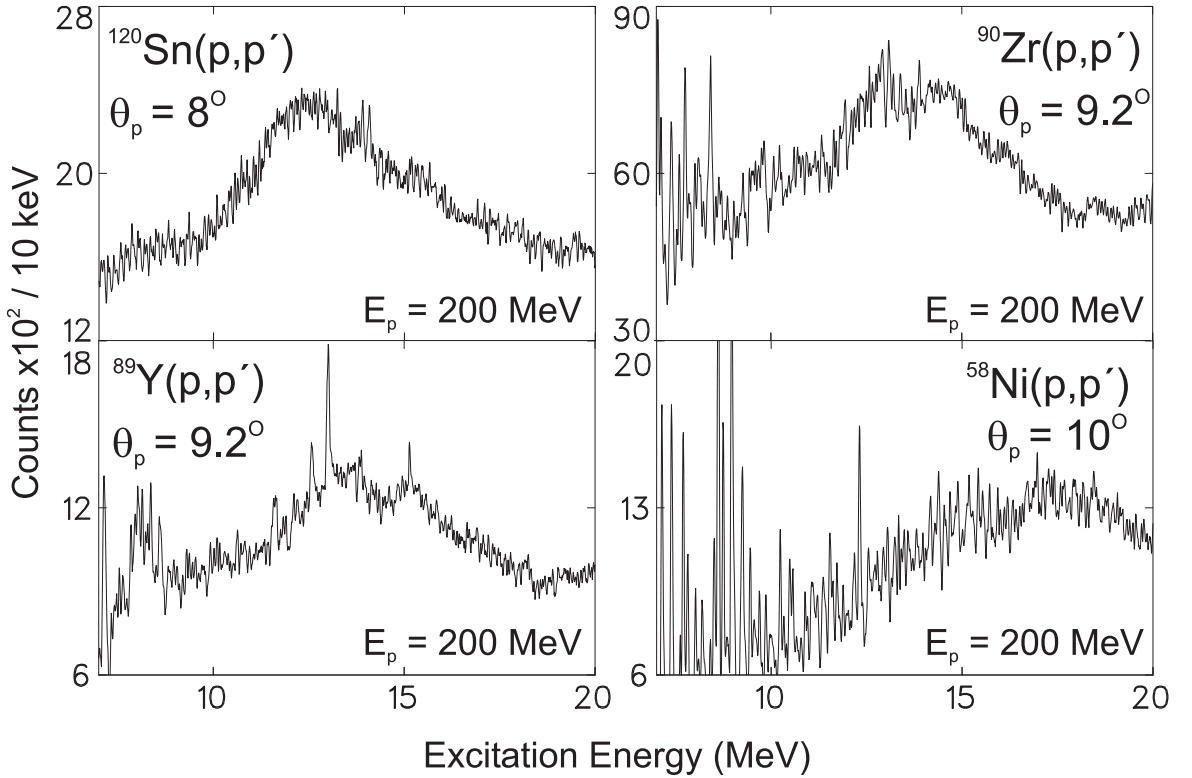


Fig. 4.11: Experimental excitation energy spectra of the ISGQR in several nuclei, ^{120}Sn (top-left panel), ^{90}Zr (top-right panel), ^{89}Y (bottom-left panel), and ^{58}Ni (bottom-right panel) measured at $E_p = 200$ MeV for scattering angles corresponding to a maximum in the $\Delta L = 2$ angular distribution. All the cases show the appearance of the fine structure, confirming the phenomenon as a global feature of the ISGQR.

The excitation energy spectra of the GQR region in other measured target nuclei are presented in Fig. 4.11. In all the nuclei studied one could observe the appearance of the fine structure, which conforms to the suggestion of the global character of this phenomenon in the ISGQR, present in many different nuclei. The figures 4.12 and 4.13 investigate the kinematical dependence of the fine structure phenomenon for the cases of ^{208}Pb and ^{90}Zr . Both nuclei were measured over a larger angle range where other multipoles may become important. Finally, Fig. 4.14 presents two excitation energy spectra of ^{142}Nd (left) and ^{166}Er (right) nuclei taken during the second beam time in year 2003. Resonance structure is observed in both spectra. ^{142}Nd spectrum contains several strong peaks on top of the resonance. Despite increased level density in a deformed ^{166}Er nucleus, one can still see rather strong fluctuations of the cross section, indicating the presence of fine structure even under such conditions.

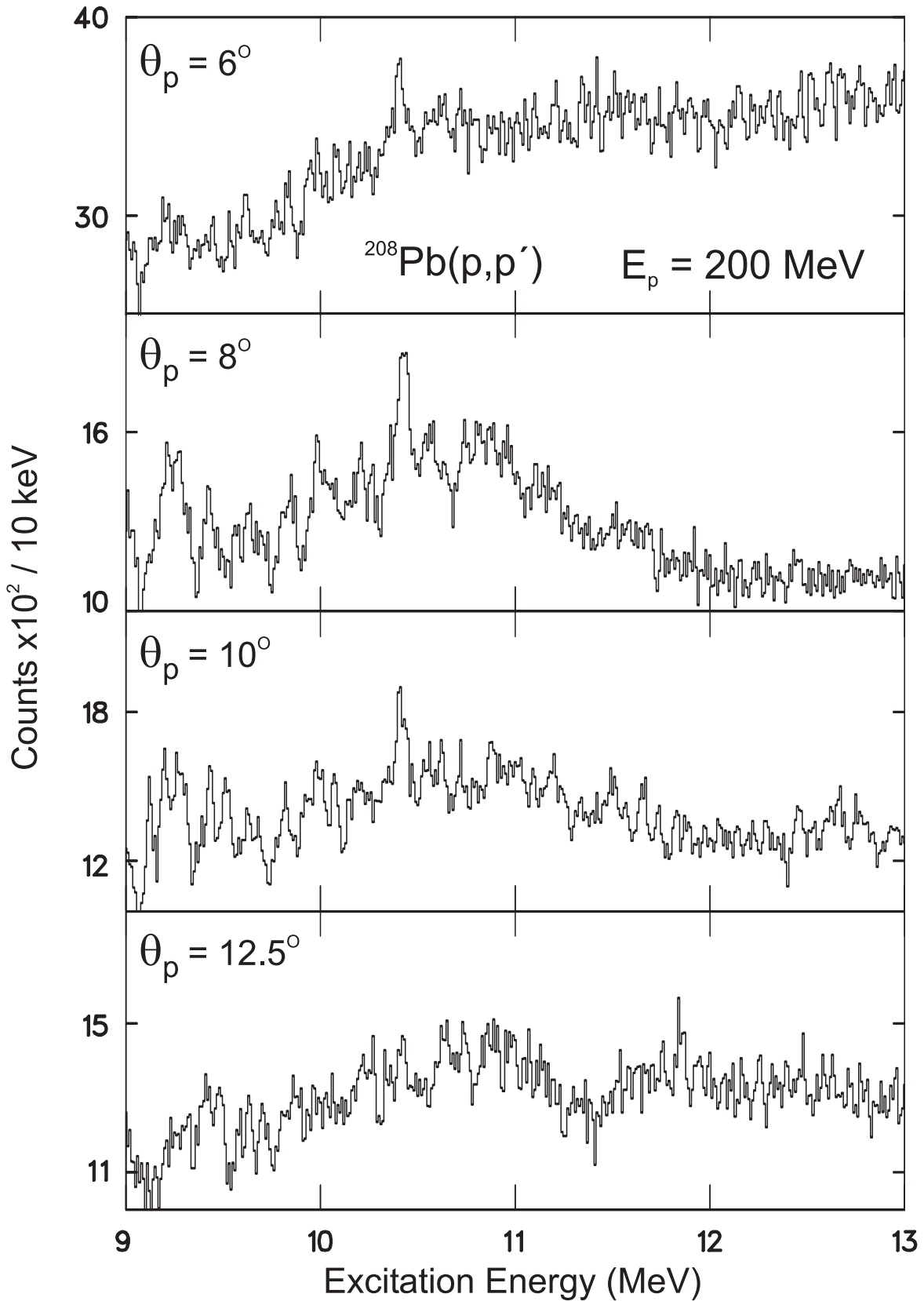


Fig. 4.12: Excitation energy spectra in the ^{208}Pb nucleus for different proton scattering angles at $E_p = 200$ MeV. A scattering angle of $\Theta_p = 8^\circ$ corresponds to the maximum of $\Delta L = 2$ angular distribution.

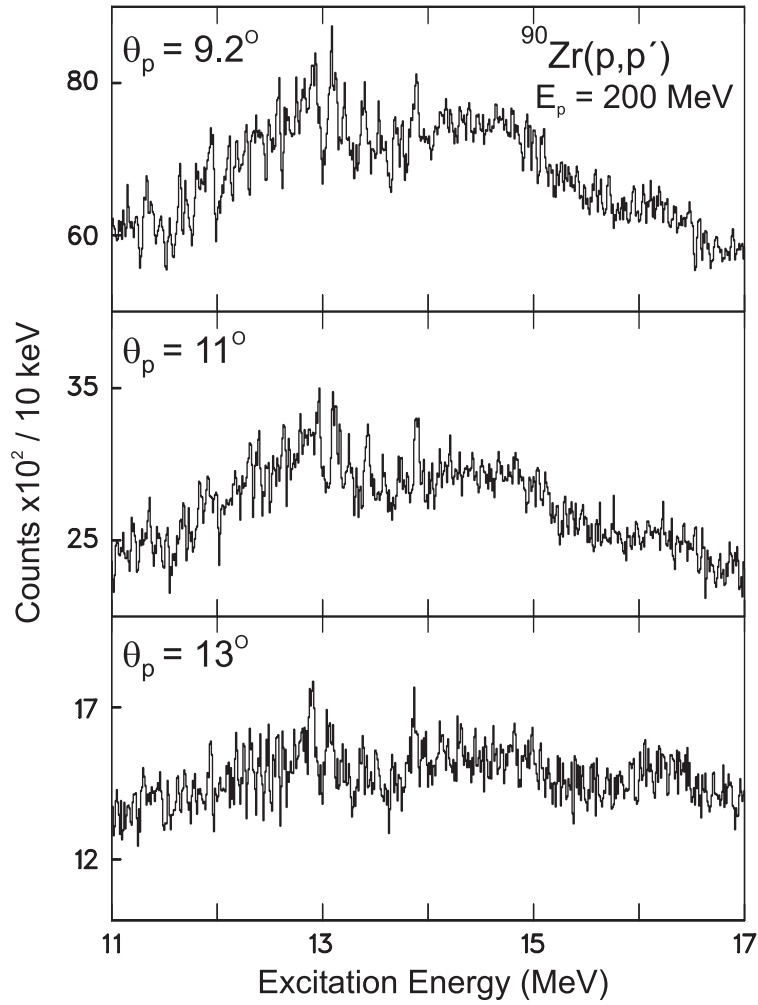


Fig. 4.13: Excitation energy spectra in the ^{90}Zr nucleus for different proton scattering angles at $E_p = 200$ MeV. A scattering angle of $\Theta_p = 9.2^\circ$ corresponds to the maximum of $\Delta L = 2$ angular distribution.

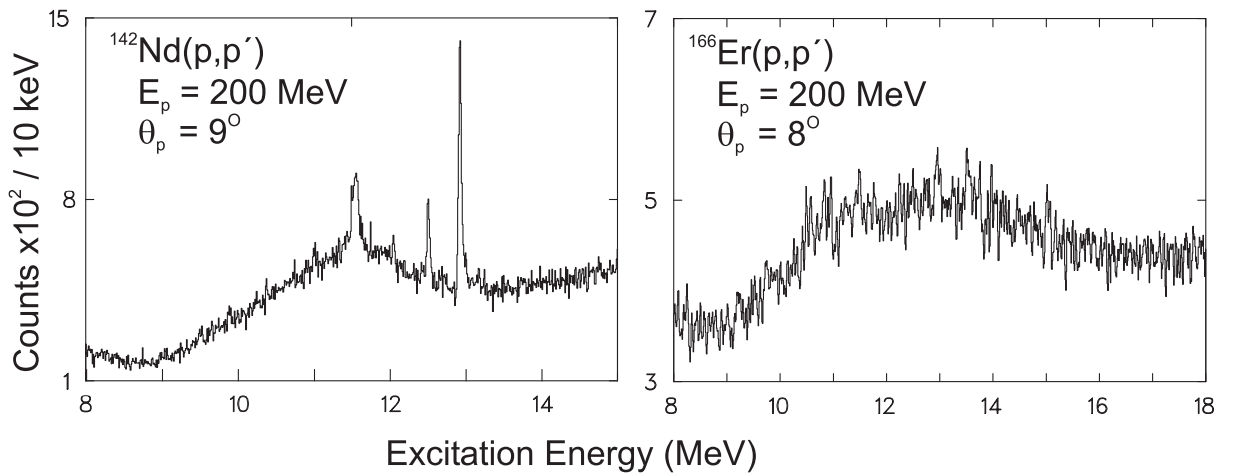


Fig. 4.14: Excitation energy spectra in the GQR region of ^{142}Nd at $\Theta_p = 9^\circ$ (left) and ^{166}Er at $\Theta_p = 8^\circ$ (right).

5 Search for Characteristic Energy Scales of Fluctuations

Very often complex many-body systems exhibit an interplay of ordered collective motion with chaotic behavior. Giant resonances in atomic nuclei represent an example of such an interplay, where a highly collective excitation of almost all nucleons is damped out via a chaotic continuum of many intrinsic degrees of freedom in many-body quantum-mechanical systems.

In this section, a brief overview will be given of the techniques that might appear to be suitable for studying such a class of phenomena. In more detail, the concept of entropy will be discussed, together with the novel method of the entropy index analysis.

5.1 Characterization of Quantum-Chaotic Phenomena

In order to quantitatively characterize the fine structure observed in the high energy-resolution experimental data one needs elaborate tools with whom one is able to extract the significant features out of noisy spectra in a model-independent way. Several methods have been proposed so far. Historically, one of the first methods successfully adopted to the fine structure studies was the doorway-state analysis, applied for the case of the GQR in ^{208}Pb [44] and later for magnetic-dipole strength in ^{58}Ni [67]. Assuming sequentially a one- and a two-doorway model for coupling to a large number of complex configurations one was able to extract the coupling matrix elements and determine the escape and spreading widths for the underlying doorway states. Despite the richness of extracted information, the practical application of the doorway-state analysis is connected with complications. Firstly, the technique itself is very sophisticated and time consuming. Thus, only in the case of the one doorway assumption unambiguous results could be derived, whereas when suggesting the two-doorway configuration in the decay of the GQR in ^{208}Pb the problem becomes so complicated, that

in practice no reliable estimates can be made anymore. Secondly, the results of the analysis are model-dependent, since one has to know the number of doorway states *a priori*.

A typical path towards chaos goes through a sequence of fluctuations. There exist several quantitative measures of chaotic vibrations: frequency distribution, fractal dimension, invariant probability distribution, Lyapunov exponents [68] and correlation dimensions [69], Kolmogorov entropy [70] etc.

When the motion is periodic or quasiperiodic, the frequency distribution shows a set of narrow spikes or lines, indicating that the signal can be represented by a discrete set of harmonic functions $e^{\pm i\omega_k t}$. Near the onset of chaos, however, a continuous distribution of frequency appears, and in the fully chaotic regime the continuous spectrum may dominate over the discrete spikes. The representation by the Fast Fourier Transform essentially treats a signal as a periodic function. In general, this is not the case and a discontinuity is introduced which adds spurious information into the frequency distribution. This is called *aliasing error*, and some methods exist to minimize its effect [71].

The Lyapunov exponent λ , which was initially introduced for an analysis of chaos, measures the rate at which nearby points on an attractor diverge or converge along nearby trajectories. For regular motions the condition $\lambda \leq 0$ is realized, whereas for chaotic motions λ should be positive. Correlations are a well-known tool to measure the lifetime of a quantal system. Thus, the autocorrelation function can be utilized. When a signal is chaotic, information about its past origins is soon lost. This means that the autocorrelation function goes to zero as time goes to infinity or that the signal is only correlated with its recent past. Correlation integrals and correlation dimensions are useful quantities to examine whether a given signal is chaotic or not [68, 69].

Unfortunately, all these quantities are properly defined only for stationary signals, and, therefore, are not applicable to the case of damping of giant resonances, which is a highly non-stationary process.

The nearest neighbor spacing distribution [72] and the Δ_3 -statistics are reliable measures for chaoticity of the system in a regime of resolved non-overlapping states of one known well-separated class (e.g. states with a certain spin J^π).

However, this quantity cannot be applied to the case of the continuum of strongly overlapping states and fluctuating strength.

The fluctuation analysis using the autocorrelation function is also an established method to extract level densities and scales out of the fine structure. Nevertheless, in this method there also exists a problem, namely that the background should be known beforehand, which is usually not the case for experimental data. Besides, the method is restricted only to the case of small and intermediate scales.

5.2 Entropy Index Method

A natural approach to quantitatively describe the degree of order or chaos in a complex system is to use a concept of entropy. The thermodynamic entropy is well known in physics as a measure of disorder of a system. A new measure of spectral entropy has been recently defined from the Fourier power spectrum. An ordered activity with a narrow peak in the frequency domain would result in a low entropy, while disordered activity with a wide-band frequency response would give large values for the entropy. However, it has some disadvantages: the Fourier transform does not take into account the time evolution of the frequency patterns. It also requires stationarity of the signals, which is often not fulfilled.

Consequently, a further development of this idea is to define the entropy from a wavelet transform. Based on this concept is the entropy index method, which enabled, in a novel way, to determine the number of scales present in the spectra and their magnitude. This technique has been initially proposed for the study of self-similar fluctuations in heartbeats [73] and was later adopted to fine structure studies [46]. The method gives model-independent results, for it does not make any *a priori* assumptions on the number of doorways or on the decay mechanisms. The following section describes the entropy index method in detail.

The main idea is to construct a measure that would characterize the fluctuations of some physics observable $\sigma(E)$, e.g., the cross section or the strength function, as a function of the resolution in energy δE , as shown in Fig. 5.1. Having an experimental spectrum covering the excitation energy interval $\Delta E = [E_{min}, E_{max}]$, one

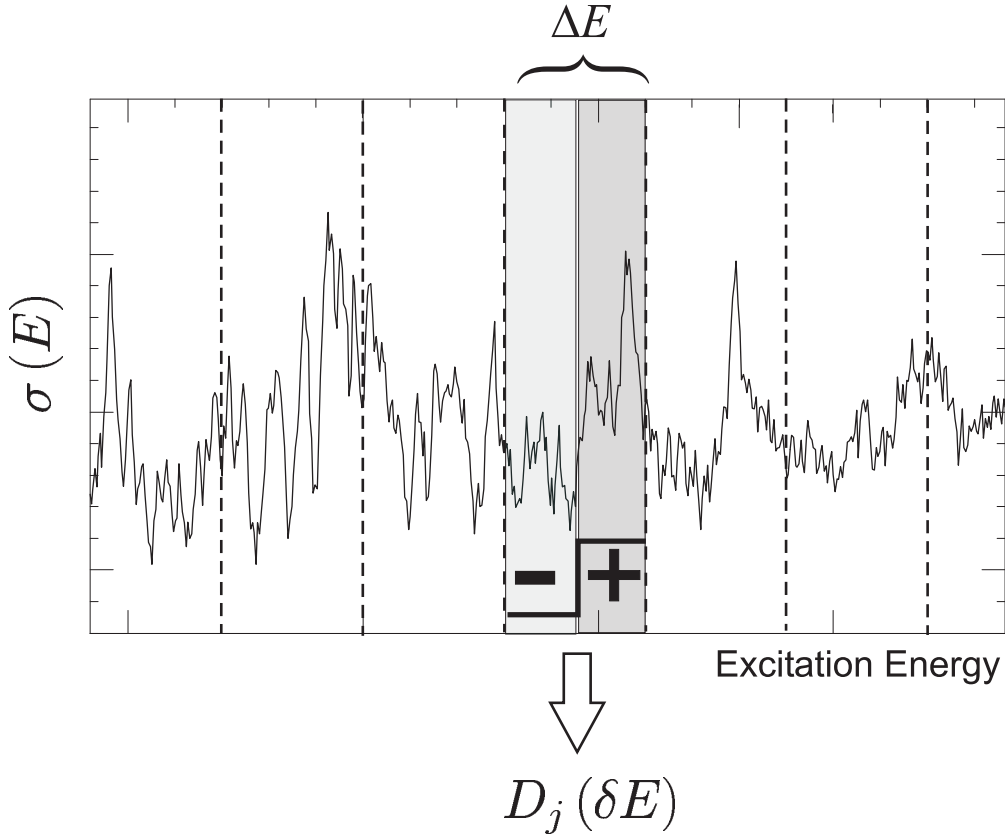


Fig. 5.1: Entropy index method explanation. The binning width δE defines the scale, at which the fluctuations are to be characterized. A set of coefficients $D_j(\delta E)$ describes the fluctuation level at a given scale for each subinterval of the spectrum by taking the coarse-grained derivative of the function.

can divide this interval into n equal bins with the size of δE , so that $n = \Delta E/\delta E$. The coefficients D_j for each bin j is defined as

$$D_j(\delta E) = \int_{E_{j-1}}^{E_j} dE \sigma(E) \Psi_j(E), \quad (5.1)$$

where $E_j = E_{min} + j\delta E$. In this expression, $\Psi_j(E)$ denotes the analyzing window function which takes a non-zero value in the interval $[E_{j-1}, E_j]$ and is equal to zero outside the given bin. One can take any antisymmetric function with zero mean. The simplest one is just a step function defined as follows

$$\Psi_j(E) = \text{sign}(E - (j - 1/2)\delta E). \quad (5.2)$$

The coefficients D_j represent a coarse-grained derivative of the function σ in each bin j , and the values of these coefficients are directly related to the fluctuations

of σ at the considered scale δE . These coefficients are then normalized by the average of their absolute values,

$$W_j(\delta E) = |D_j| / \langle |D_j| \rangle \quad (5.3)$$

with

$$\langle |D_j| \rangle = 1/n \sum_{j=1,n} |D_j|, \quad (5.4)$$

so that the normalized quantities do not depend on the magnitude of the original signal. In order to obtain global properties of these fluctuations, one builds an entropy index K

$$K(\delta E) = -\frac{1}{n} \sum_{j=1}^n W_j(\delta E) \log W_j(\delta E), \quad (5.5)$$

which has several interesting properties. For the case of pure statistical fluctuations the values of $K(\delta E)$ remain constant. A change in the behavior of $K(\delta E)$ is a signature for the appearance of a characteristic scale. For progressively more and more complex configurations the entropy index value should increase reaching the maximum value for the scale with the most complex $np-nh$ configuration, i.e.

$$K(\delta E)_{np-nh} > \dots > K(\delta E)_{2p-2h} > K(\delta E)_{1p-1h}. \quad (5.6)$$

Therefore, changes in the entropy index $K(\delta E)$ at certain energy scales δE indicate the existence of multiple scales present in the fine structure. By studying the behavior of $K(\delta E)$ it is possible to extract the values of characteristic energy scales of fluctuations in the excitation spectra. Very often the number of data points is not large, which limits the analysis at large binning intervals δE . In order to avoid this problem, one takes many repetitions of the analyzed data interval [46].

5.3 Results of the Entropy Index Analysis

This method has already been successfully applied to the case of ISGQR in ^{208}Pb [27]. It has been shown that the entropy index method can detect well-separated prominent scales of fluctuations in the spectra. The intermediate scales

of fluctuations around 1.1 MeV, 460 keV and 125 keV for an excitation energy region 7.6 – 11.7 MeV were found. Figure 5.2 displays the entropy index as a function of the averaging interval δE , when deduced from the $^{208}\text{Pb}(p,p')$ experiment at iThemba LABS (see Fig. 4.8), for the same excitation energy interval. The entropy index in Fig. 5.2 exhibits sudden variations as a function of δE which can be associated with the appearance of different dominant scales in the fine structure. Although the number of dominant scales appears directly from the analysis, their precise determination is not straightforward from the localization of the curvature changes. The model studies carried out have shown that for the models considered in [46] the entropy index can be approximated by a function $F(\delta E)$ defined as $F(\delta E) = \sum_n K_n(\delta E)$ where n is an index running over the different scales and where $K_n(\delta E)$ is defined as a Fermi-Dirac-like distribution function

$$K_n(\delta E) = \frac{k_n}{1 + \exp\left(\frac{\ln(\delta E) - d_n}{\Delta_n}\right)} \quad (5.7)$$

with parameters k_n , d_n and Δ_n . A superposition of Fermi functions simulates the characteristic increase of the entropy index with the appearance of a new scale.

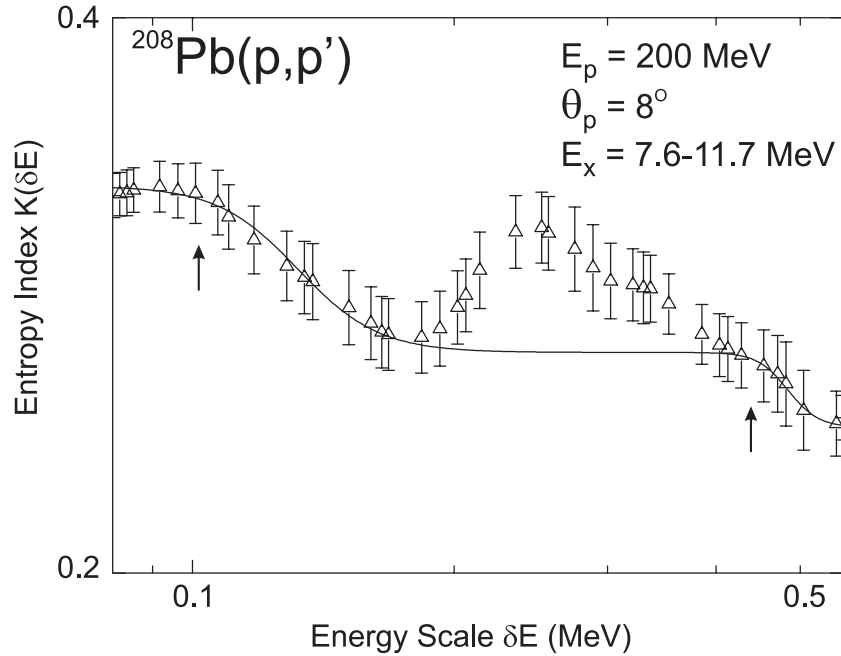


Fig. 5.2: Entropy index K as a function of the averaging interval δE for the ^{208}Pb spectrum. The solid line is a fit using a superposition of Fermi-Dirac functions which simulates the characteristic increase of the entropy index with the appearance of a new scale in the spectrum.

By studying the model cases where the scales Γ_n were known, one could establish an empirical relation $K_n(\Gamma_n)/k_n = 0.92 \pm 0.01$. By applying the same ratio to the parameters of Fermi-Dirac functions that are obtained from the fit to the entropy index derived from experimental data, one can extract the values of characteristic scales. The solid line in Fig. 5.2 is a fit by a sum of several Fermi-Dirac functions using the least squares minimization. The data provide evidence for several scales in the spectrum, 1.1 MeV, 440 keV, and 100 keV, which are similar to what was found previously in ^{208}Pb [27]. At the same time, the entropy index of the proton data, in the region between 200 and 300 keV, shows an increase of the entropy index with increasing scale, which cannot be described by Fermi-Dirac functions. This represents an intrinsic problem of the entropy index method, which often hinders the correct extraction of characteristic scales.

5.4 Limitations of the Entropy Index Method

The development of the entropy index method was in some sense a turning point which revived the discussion of a long-standing problem of damping of collective modes, resulting in new ideas and possibilities. Despite this fact, there are a few reasons which limit to some extent the application of this method. A test study of the possible influence on the entropy index of the physical background from e.g. quasielastic scattering, and possible experimental background showed that their energy dependence can under certain circumstances affect the results of the analysis. It was also found that the choice of the energy interval may play a significant role.

The main drawback of this technique is the lack of information on the localization of scales against excitation energy. One is not able to tell if the scale is really coming from a local resonance area or exists over larger energy regions. Besides, the resolution of the extracted values of scales appears to be intrinsically limited by the technique itself. For example, if several scales are lying close to each other, or even partially overlap, or are weak (i.e. are having small significance) the entropy index method will not be able to separate them. In this case it is not easy to unambiguously determine the number of the scales and their values. Therefore,

the results obtained from the entropy index method have to be accompanied by the analysis using other methods for identification of the characteristic scales.

5.5 Local Scaling Dimension

Another novel idea is a multifractal analysis of the fluctuating strength function, proposed by Aiba et al. [25]. It is, however, essentially similar to the approach of the entropy index method in the way of constructing some characteristic measures for the fluctuations as a function of scaling dimension, namely the partition function, thereby inheriting the same limitations as the entropy index method.

Although in the case of theoretical strength calculations the local scaling dimension method provides a good extraction of scales [24–26], the numerical study carried out showed that the technique is not stable in respect to even the constant background. This makes the application of the method to experimental data, which usually contain some background, questionable. Besides that, the resolution of scale extraction in this technique is rather limited, so that it is suitable only in cases where one has just few well-separated scales.

5.6 Fourier Analysis

The Fourier transform (FT) is an adopted tool for the analysis of periodic signals [74]. It decomposes a signal into its constituent frequency components. Despite the functionality of the Fourier transform, there are several shortcomings of this technique. The first drawback is the inability of the FT to accurately represent functions that have non-periodic components that are localized in time or space, and are often observed as a signature for a transient behavior. The FT is based on the assumption that the signal is periodic and of infinite length. Another deficiency is its inability to provide any information about the time dependence of a signal, since the signal to be examined is assumed to be stationary, and thus cannot give a time evolution of the frequency pattern. Any existing correlation

between the time and frequency domains of a signal will not be detected by the Fourier transform. Most physics phenomena in nature are actually not stationary, but rather have a transient, aperiodic character. The Fourier analysis appears to be not suited for the non-stationary aperiodic signals having finite duration [75].

5.7 Windowed Fourier Transform

The above-mentioned limitations of Fourier analysis can be partially resolved by using a windowed Fourier transform (WFT). Under the assumption that the analyzed signal is quasi-stationary within the narrow time period, the FT can be applied within this narrow window. This window is shifted along the time axis, and the same procedure is repeated, thereby obtaining the time evolution of the frequency spectrum. An arbitrary windowing function such as a boxcar (no smoothing) or a Gaussian window can be chosen. The problem with the WFT roots back to the Heisenberg uncertainty principle, which dictates that one cannot know what spectral components exist at what instances of time. What is known are the time intervals in which a certain band of frequencies exist [75]. Using a window of infinite length, the FT is obtained, which gives perfect frequency resolution, but no time information. Moreover, the stationarity assumption is violated. The narrower one makes the window, the better the time resolution, and the better the assumption of stationarity, but a poorer frequency resolution becomes. In the WFT one averages short-duration components and cannot capture those components that last longer than the window itself. The cutoff of low- and high-frequency components that did not fall within the frequency range of the window gives additional inaccuracy to the obtained results. The inefficiency is caused by the fact that usually several window lengths must be tried to determine the most appropriate choice. The WFT represents, therefore, an inaccurate and inefficient method of time-frequency localization. For analyses where a predetermined scaling may not be appropriate because of a wide range of dominant frequencies, a method of time-frequency localization that is scale independent, such as wavelet analysis, should be employed [76].

6 Wavelet Analysis

The wavelet analysis provides a novel and extremely effective way to represent and analyze multiscale structures. Indeed, many physical systems are organized into “levels” or “scales” of some variable. A multi-resolution or scalable mathematical representation may provide a simpler and more efficient extraction of the relevant degrees of freedom in physical systems [77]. In this section, a brief review of the wavelet transform and its defining properties is presented together with the discussion of practical aspects and optimization for the problem of fine structure in nuclear response and giant resonances.

6.1 Wavelet Transform

The distinct feature of a wavelet analysis is the presence of a scaling parameter, which - loosely speaking - can be interpreted as reciprocal Fourier frequency. The wavelet transform (WT) differs substantially from the windowed Fourier transform (WFT), discussed above, as it allows for an arbitrarily precise localization in time of high-frequency signal features. This is explained schematically in Fig. 6.1. Shown are the Heisenberg uncertainty boxes associated with the analyzing functions in the position, or, applied to our case, excitation energy–vs.–energy scale plane. In the WFT the Heisenberg box has always constant dimensions at all scales and locations. On the contrary, in the wavelet transform the analyzing wavelet function changes its size depending on the scale parameter, so that the associated Heisenberg uncertainty box in the position-scale plane becomes narrow and tall at small scales or wide and short at higher scales. This flexibility allows the time evolution of the frequency pattern to be studied with an optimal resolution. Another important distinction between the wavelet and Fourier analysis is that the former is not limited to using sinusoidal analyzing functions only, but rather can employ a large selection of localized waveforms as long as they satisfy the predefined mathematical criteria described below.

The WT is based on the concept of wavelet functions or so-called *wavelets*. There exist two conditions which determine whether a certain real or complex function

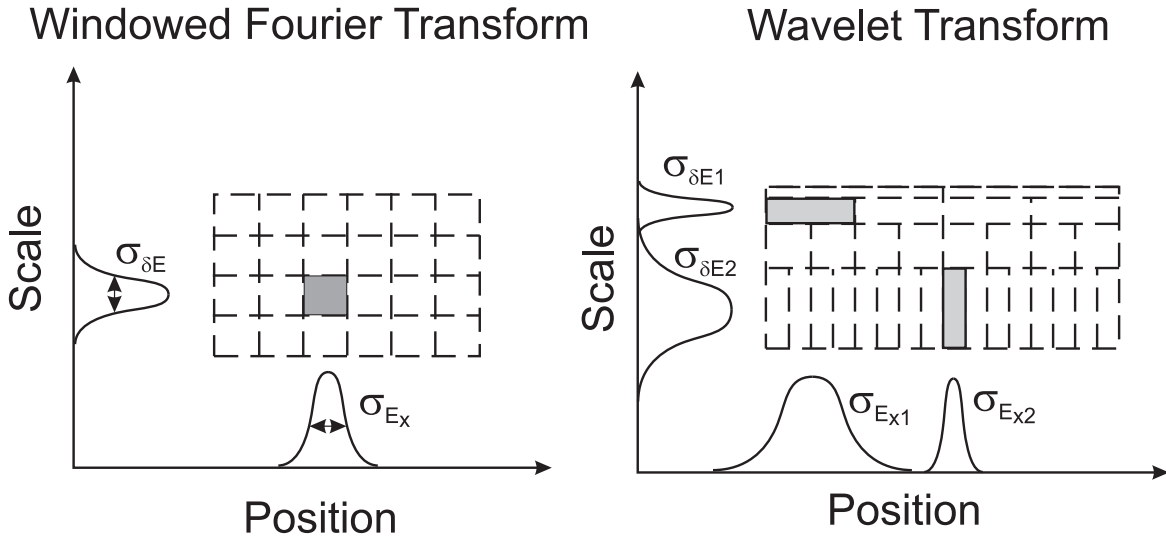


Fig. 6.1: Heisenberg uncertainty box associated with the analyzing function of the WFT (left panel) and WT (right panel) in the position-vs.-scale plane. The WFT retains the resolution constant all over the time-frequency plane. Conversely, the resolution of the wavelet transform is adjusted to the optimum at each point. Better scale information is extracted at large scales, where the signal dynamics is low and the time information is less important, whereas for small scales, where the signal changes rapidly, the resolution in time is improved.

$\Psi(x)$ can be used as a wavelet,

$$\int_{-\infty}^{\infty} \Psi^*(x) dx = 0, \quad (6.1)$$

and

$$K_{\Psi} = \int_{-\infty}^{\infty} |\Psi^2(x)| dx < \infty, \quad (6.2)$$

where the index $*$ means complex conjugation. The quantity K_{Ψ} is the wavelet norm, or so-called *admissibility constant*, which is different for various wavelets. The first requirement imposes that the function must be oscillating (therefore, 'wave-' in the naming convention), and in the absence of an imaginary part its mean value should be zero. The second equation describes the requirement of a finite duration or so-called *compact support* of the function (therefore, '-let'). Thus, wavelet basis functions describe the local behavior more efficiently because they are not affected by properties of the data far away from the location of

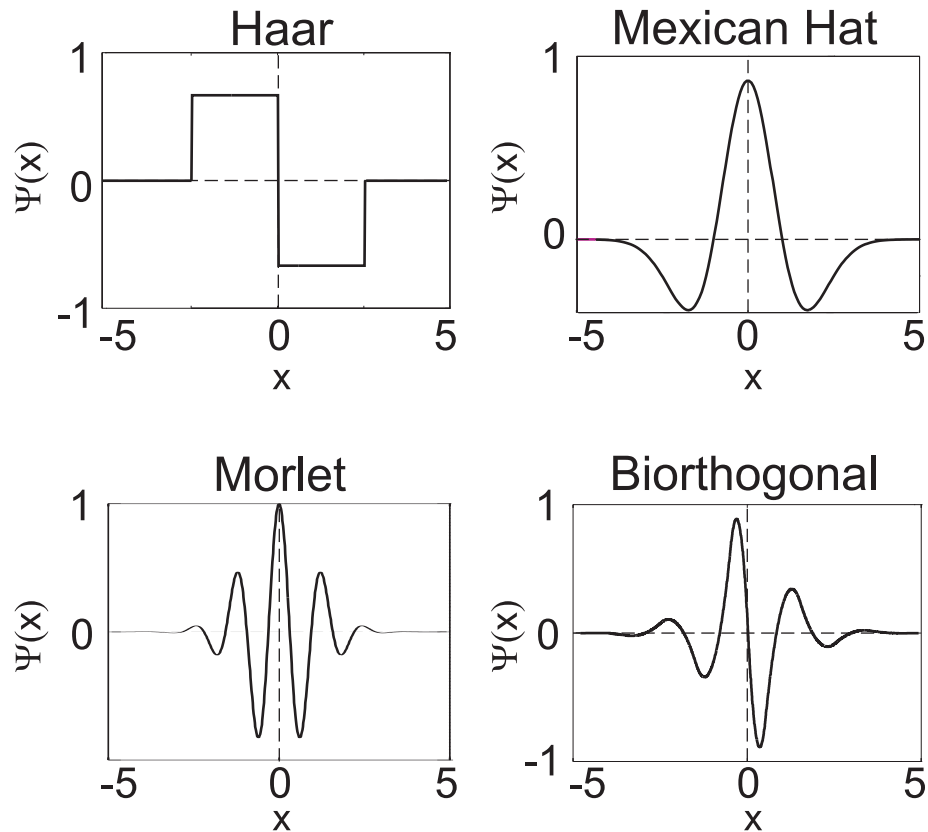


Fig. 6.2: Some frequently used wavelet functions. The Haar wavelet (top-left panel) is a combination of several Heaviside step functions, producing a square wave. Its usage is analogous to the entropy index method. The Mexican hat (top-right) is the second derivative of the Gauss function, taken with a negative sign. It has better localizing properties, than the Haar wavelet. The Morlet wavelet (bottom-left) is a locally periodic wavepacket, constructed out of a plane wave modulated by a Gaussian. The so-called *Bior3.9* function has no analytic form (bottom-right).

interest. In other words, a wavelet is a small wave, localized both in time and frequency domains.

Having only these two conditions one might expect to have an unlimited variety of functions that can be used as wavelets. Indeed, constructing a function that satisfies these two requirements is not a very difficult task. However, highly sophisticated mathematics is involved when wavelets with special properties are wanted. Some examples of such functions widely used in wavelet analysis are presented in Fig. 6.2. Their properties will be discussed later, as soon as some important features of the wavelet transform have been introduced.

The wavelet transform of some signal $\sigma(E)$ is defined as its convolution with the (generally complex-conjugated) wavelet function as

$$C(\delta E, E_x) = \frac{1}{\sqrt{\delta E}} \int \sigma(E) \Psi^* \left(\frac{E_x - E}{\delta E} \right) dE . \quad (6.3)$$

The first parameter δE scales the function (makes a dilation), whereas the second parameter E_x shifts the wavelet position along the excitation energy, so that the scale localization information becomes accessible. As a result of such a transformation one obtains a 2-D distribution of wavelet coefficients $C(\delta E, E_x)$. These coefficients will be large at those scales δE and locations E_x , where the form of the scaled and shifted wavelet $\Psi(x)$ has a great similarity to the analyzed data sample $\sigma(E)$. Vice versa, if the scale of a wavelet function is very different from characteristic scales in the data at a given location, the coefficients will be small. Therefore, by studying this 2-D distribution of wavelet coefficients one can extract not only the values of the characteristic scales but also their locations, which is very important for non-stationary processes. It is also possible to reconstruct the original signal out of the wavelet coefficients by using the inverse wavelet transform [75, 78, 79]

$$\sigma(E) = \frac{1}{K_\Psi} \int_{-\infty}^{\infty} \int_0^{\infty} C(\delta E, E_x) \frac{1}{(\delta E)^{5/2}} \Psi \left(\frac{E_x - E}{\delta E} \right) d(\delta E) dE_x . \quad (6.4)$$

This reconstruction procedure is widely-used in practice for wavelet filtering of noise out of the data and in compression algorithms. As it will be shown later in the present work, another important application of the inverse reconstruction is the significance test of different wavelet scales.

6.2 Continuous vs. Discrete Wavelet Transform

The wavelet analysis can be generally divided into two categories: continuous wavelet transform (CWT), where the scale and location parameters δE and E_x are varied continuously, or discrete wavelet transform (DWT), which adopts variables

only at discrete points

$$\delta E_k = 2^k \Delta \quad E_{x_k} = k \cdot \delta E_k, k = 1, 2, \dots, \quad (6.5)$$

where Δ is the binsize of the data. The smallest possible scale is therefore 2Δ .

Both methods have their advantages and drawbacks. Continuous wavelets are more favorable when high temporal and spectral resolution and/or phase information is required. The CWT provides intuitively clear results that are easy to interpret. However, depending on the problem the computational effort can become demanding, when the arrays of the wavelet coefficients become huge. A limitation of the CWT is that only an approximate reconstruction of the signal from the obtained wavelet coefficients is possible.

Contrary to the CWT, the DWT can be performed quickly. The DWT is able to produce a very sparse representation of large amounts of data, conserving at the same time the characteristic features. Often the coefficients from the DWT are used to verify the fractal scaling properties of chaotic behavior in different phenomena. The drawback here is that the scale resolution is limited as one has to increase the bandwidth of the filter by a factor of two at each new scale. The DWT does not possess translational invariance, i.e. the results will depend on the selected interval and how this interval is divided into separate subregions (the same problem appears in the entropy index as well). Finally, the DWT is possible only with some specific wavelets from which an orthogonal basis of functions can be constructed.

The choice of which kind of a wavelet analysis to use, the continuous transform or the discrete one, depends very much on the nature of the phenomenon under investigation, and on the data itself. The ability of the wavelet transform to localize structures both in time and in frequency domains makes it possible to analyze time series that contain non-stationary power at many different frequencies [80]. The wavelet transform has been proven to be particularly useful for analyzing signals which can be characterized as aperiodic, noisy, intermittent, irregular, transient, fractal and so on. The unique properties of the WT have resulted in a number of sophisticated wavelet-based methods for signal decomposition, manipulation, pattern recognition, feature extraction (e.g., discontinuities and singularities). The range of applications is very large and is still expanding quickly [81].

6.3 Properties of the Wavelet Transform and Wavelet Functions

In the present section, some of the most important features of the wavelet transform are briefly outlined.

6.3.1 Linearity of the Wavelet Transform

From (6.3) one can immediately see that the wavelet transform is a linear operation. This means that the wavelet transform of a signal, which is the sum of two components,

$$\sigma(E) = \sigma_1(E) + \sigma_2(E) , \quad (6.6)$$

is equal to the sum of the two separate wavelet transforms of these two components, i.e.

$$\frac{1}{\sqrt{\delta E}} \int [\sigma_1(E) + \sigma_2(E)] \Psi^* \left(\frac{E_x - E}{\delta E} \right) dE = C_1(\delta E, E_x) + C_2(\delta E, E_x) . \quad (6.7)$$

This is a very useful property, especially when combined with the property of vanishing moments.

6.3.2 Vanishing Moments

One of the very 'desirable' properties is the number of the so-called *vanishing moments* of the wavelet function. One can define a k^{th} moment of a wavelet function by

$$M_k = \int_{-\infty}^{\infty} x^k \cdot \Psi(x) dx , \quad k = 0, 1, \dots \quad (6.8)$$

By the definition of a wavelet function, the 0^{th} moment M_0 is zero, according to (6.1). In other words, any wavelet function has at least one vanishing moment (M_0). However, one can construct such wavelet functions that will have other higher moments equal or close to zero, i.e.

$$M_k = 0 , \quad k = 0, \dots, N . \quad (6.9)$$

Such a function is said to have N vanishing moments. The importance of this property becomes clear if one recalls that the wavelet transform is a linear operation. Usually the experimental data are composed of a useful signal of interest and a noise component, or some background, which hampers the extraction of the useful information

$$\sigma(E) = \sigma_{useful}(E) + \sigma_{BG}(E) . \quad (6.10)$$

If the background contribution $\sigma_{BG}(E)$ can be approximated by a constant or by some polynomial function, then the wavelet transform of the measured data using a wavelet function with a sufficient number of vanishing moments will effectively filter out the background contribution, so that the result will not be affected by the background. This remarkable feature makes wavelets a powerful tool for the analysis of real experimental data with background.

6.4 Selection of the Optimal Wavelet Function

An important advantage of the wavelet analysis is the freedom to use different wavelet functions and find the most appropriate one for a given problem, thereby extracting the required features most efficiently. In order to achieve a sparse representation of the signal using wavelet analysis, one has to select a function, which best resembles the features of the signal to be studied. Thus, the shape of the wavelet function should be similar to that of the signal. However, also the scale resolution of different wavelets must be taken into account. It is worthwhile, therefore, to consider the applicability of different wavelets to the field of giant resonances in more detail.

6.4.1 Haar Wavelet

The Haar wavelet function is a square wave (top-left of Fig. 6.2). It is perfect for real-time processing because of the high computational speed, which results from the simplicity of the Haar wavelet function. Additionally, both continuous

and discrete Haar wavelet transforms are possible. However, its bad analytic behavior with the abrupt change at the interval boundaries, i.e. its bad regularity causes some deficiencies of the Haar wavelet applications. Smooth signals cannot be approximated well by the Haar wavelet. Moreover, it has only the trivial 0^{th} vanishing moment. When applied to the fine structure studies, the wavelet transform using the Haar wavelet gives results which are affected by any background except a constant one. However, the most important limitation of the Haar wavelet is its poor resolving power for the scales. Although it is rather good in localizing the scale position along the excitation energy axis, its precision of determining the scale values is very limited, since it acts as a rather broad-band frequency filter.

6.4.2 Mexican Hat and Other Derivatives of a Gaussian

The Mexican hat (top-right of Fig. 6.2) is defined as the second derivative of a Gaussian curve:

$$\Psi_{Mexhat}(x) = (1 - x^2) \exp\left(-\frac{x^2}{2}\right). \quad (6.11)$$

As compared to the Haar wavelet, this function has a regular analytic form and possess much better scale precision, although it is achieved at the expense of decreased spatial resolution.

Generally, any m^{th} derivative of a Gaussian of the form

$$\Psi_{G_m}(x) = (-1)^m \frac{d^m}{dx^m} \exp\left(-\frac{x^2}{2}\right) \quad (6.12)$$

for $m > 0$ will satisfy the admissibility conditions. The Gaussian curve itself ($m = 0$) is not admissible as a wavelet since it does not have a zero mean, see (6.1). The m^{th} derivative has m vanishing moments starting from the 0^{th} to $(m - 1)^{th}$ and will therefore effectively suppress any polynomial components of the studied signal up to $(m - 1)^{th}$ order, thereby emphasizing contributions of weak higher orders or features, which are hidden in the background.

6.4.3 Morlet Wavelet

Another widely used function is the Morlet wavelet (bottom-left of Fig. 6.2), named after Jean Morlet, whose fundamental work laid the basis of the whole

of multiresolution analysis. The Morlet function is obtained by taking a periodic wave and localizing it with a Gaussian (bell-shaped) envelope

$$\Psi_{Morlet}(x) = \pi^{-1/4} \cos(kx) \cdot e^{-x^2/2}. \quad (6.13)$$

The value of k specifies the number of “significant” sinusoidal oscillations within a Gaussian window. Formally, the function (6.13) is not generally applicable as a wavelet. However, for $k \geq 5$ the admissibility condition (6.1) is satisfied within the accuracy of computations with single precision arithmetic. Higher values of k would slightly improve the scale resolution and in a limiting case one would end up with a Fourier spectrum. However, at the same time the scale localization property would be decreasing. For the analysis of nuclear giant resonance spectra described below, a value of $k = 5$ was found to provide the best compromise.

The Morlet wavelet appears to be the most suited for the present studies of fine structure phenomena in nuclear spectra, as it gives the smallest time-bandwidth product [82]. Indeed, the Morlet function, being a superposition of a Gaussian and a plane wave, has one of the best localization properties among the whole wavelet family both in position and in scale domains, thus resulting in a more precise and reliable extraction of the characteristic scales.

6.4.4 Biorthogonal Wavelet Bior3.9

The Bior3.9 wavelet (bottom-right of Fig. 6.2) properties are close to those of the Morlet wavelet, which makes it also suitable for fine structure studies. Its advantages are good resolution and applicability to the discrete wavelet transform, which makes it possible to exactly reconstruct the original signal from the wavelet coefficients. Besides, it possesses three vanishing moments which makes results insensitive to polynomial backgrounds of up to third order. An example of its application to the data will be given later on. A certain disadvantage is that this wavelet cannot be expressed in an analytical form.

6.5 Results of the CWT

In this section the application of the continuous wavelet transform to the experimental data will be discussed. Some of these results were presented during several international conferences and were recently published in [83–85].

6.5.1 Scales from the GQR in ^{208}Pb

As one could see in the previous section, the CWT using the Haar wavelet is a natural extension of the entropy index method. However, instead of using the Haar wavelet one can obtain better performance with other wavelet functions, e.g. a Morlet wavelet function. Figure 6.3 demonstrates the application of the new wavelet approach to the experimental $^{208}\text{Pb}(p,p')$ spectrum measured at

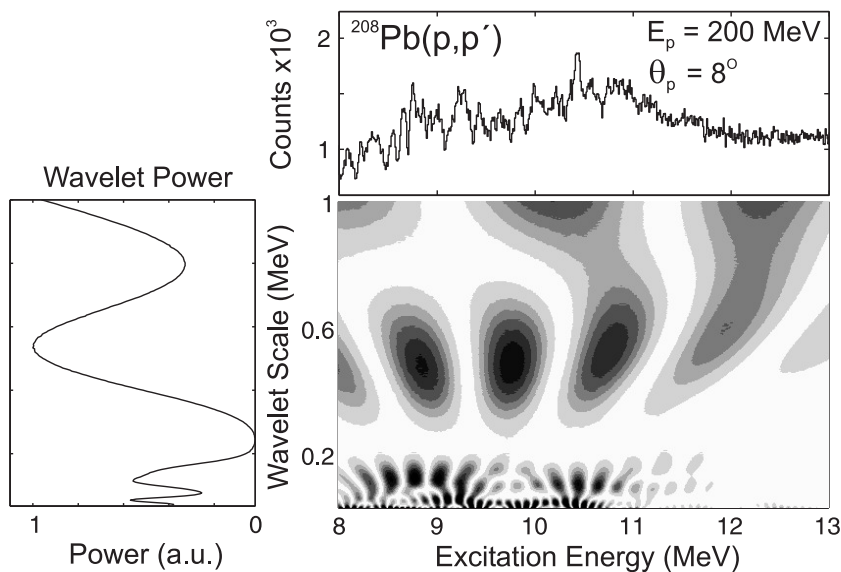


Fig. 6.3: The CWT of the excitation energy spectrum of $^{208}\text{Pb}(p,p')$ measured at 8° using the Morlet wavelet. Upper panel: spectrum of the GQR. Middle panel: 2D distribution of the squared wavelet coefficients as a function of excitation energy (horizontal axis), and energy scales (vertical axis). Dark regions indicate large amplitudes, whereas white ones correspond to small values. Left-hand side: wavelet power spectrum which corresponds to a projection of the squared wavelet coefficients onto the axis of the wavelet scale. Note that the power increases from right to left.

8° using the Morlet wavelet. The upper panel shows a part of the excitation energy spectrum, corresponding to the region of the GQR. Underneath the two-dimensional distribution of the squared wavelet coefficients is shown for each scale from 50 keV up to 1 MeV in the Y direction and for the same excitation energy region from 8 to 13 MeV in ^{208}Pb in the X direction. The shading intensity of each point on this plot corresponds to the magnitude of the squared wavelet coefficients (dark for large, white for small one). The values for each scale were normalized by the value of the scale itself. This is done in order to conserve the power of wavelet transforms at different scales, so that the values at different scales are comparable to each other. This also leads to the enhancement and better recognition of the dynamics at smaller scales, which would otherwise be strongly damped by the more powerful coefficients at larger scales. One can see on this plot regions of increased intensities (dark colors), reflecting the fluctuations, occurring with corresponding scales (Y axis), and also localized at a certain region of the spectrum (X axis). This also demonstrates one of the advantages of the wavelet transform over the Fourier transform, and also over the entropy index method, which provides only the global features of the whole selected excitation energy interval of the spectrum. In contrast, the wavelet analysis delivers additional information on the localization of scales in the excitation spectrum.

A further extension of the method is to project this 2D-plot to the scales axis, producing the so-called *wavelet power spectrum*, shown in the left panel of the figure. The maxima at certain scales along the vertical scale axis correspond now to the values of characteristic scales. Note that the horizontal power axis is increasing from right to left. For visibility reasons, the scale axis in Fig. 6.3 is limited to the value of 1 MeV. The smallest scale is the trivial one that comes from the experimental resolution. Figure 6.4 shows the region of scales up to 3 MeV, providing evidence for further characteristic scales. Both Figs. 6.3 and 6.4 demonstrate that the scales are localized in the energy region of the GQR in ^{208}Pb . Another proof is given by Fig. 6.5, where wavelet power spectra in ^{208}Pb are shown for two different excitation energy intervals, the 8 to 13 MeV region of the GQR (upper panels), vs. the excitation region of 16 to 21 MeV, where only statistical fluctuations are observed (bottom panels). Indeed, no pronounced scales can be detected at high excitation energies, even with a magnification factor of 10 in the power axis.

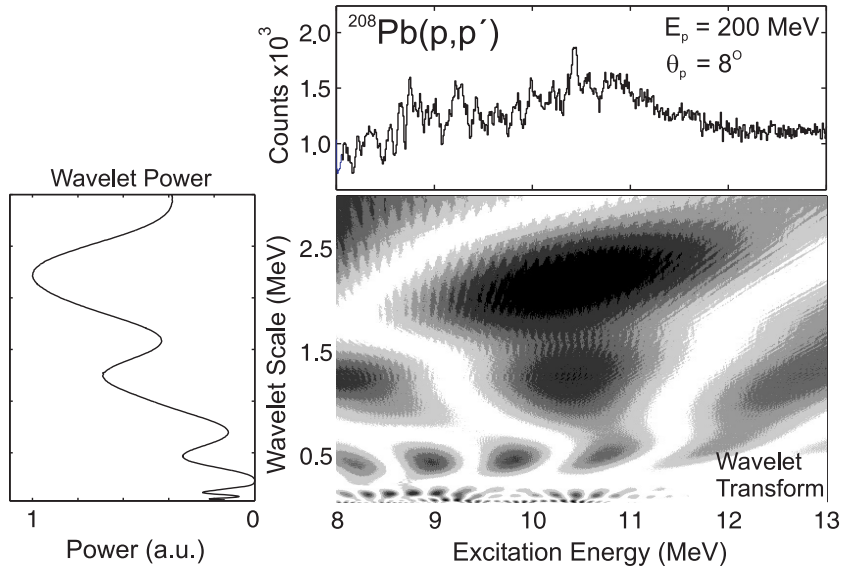


Fig. 6.4: Same as Fig. 6.3 for larger scales up to 3 MeV. Here one can observe large scales, describing the gross structure of the resonance. This shows that the scales are really coming from the resonance.

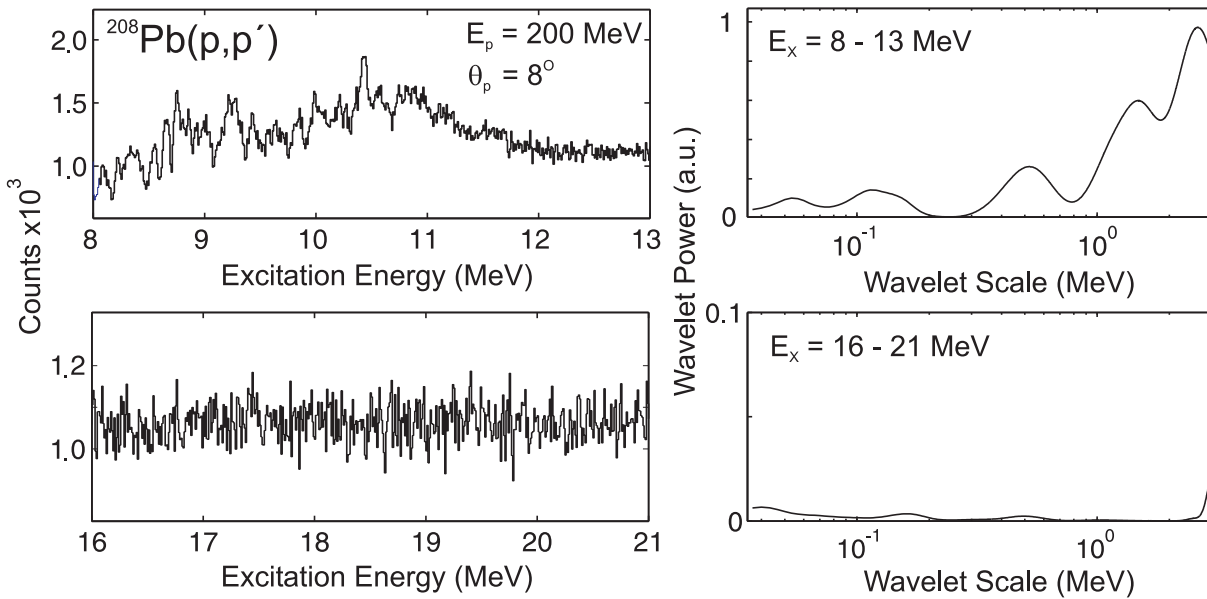


Fig. 6.5: Left-hand side: Excitation energy spectrum of ^{208}Pb for the energy interval of the GQR (top), and for the higher excitation energy region (bottom). Right-hand side: Wavelet power spectra for these two regions. At higher excitation energies one can see no prominent scales.

6.5.2 Scales in Other Magic Nuclei

The other nuclei studied in the present work also show the appearance of scales, as it is demonstrated in Figs. 6.6 - 6.8 for the region of the GQR in spectra of

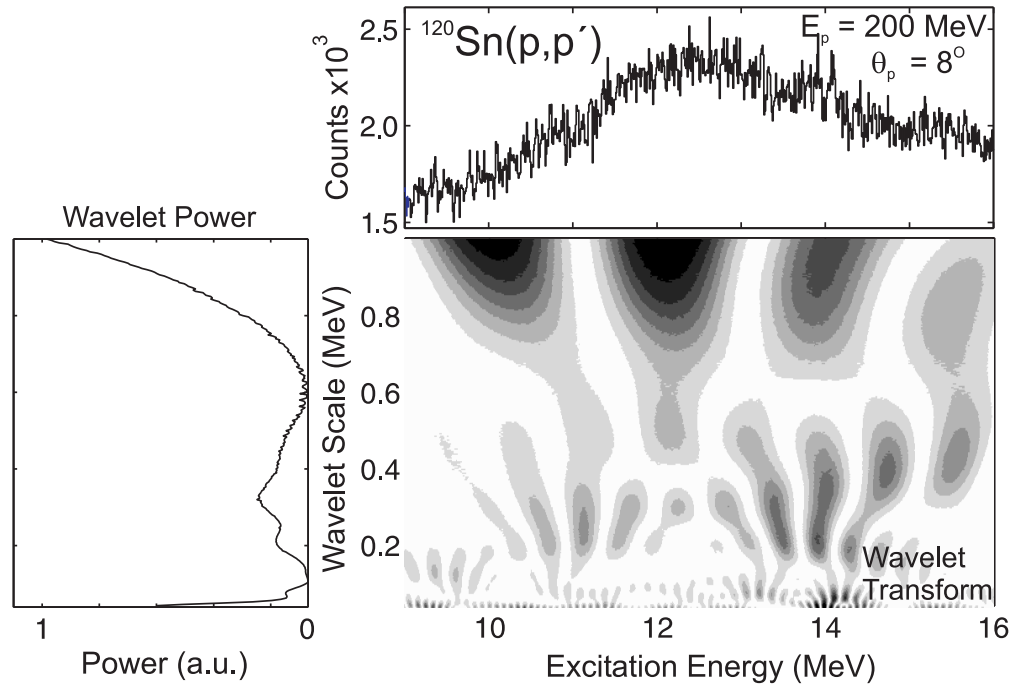


Fig. 6.6: The CWT of the $^{120}\text{Sn}(p,p')$ spectrum for $E_p = 200$ MeV and $\Theta_p = 8^\circ$ using the Morlet wavelet.

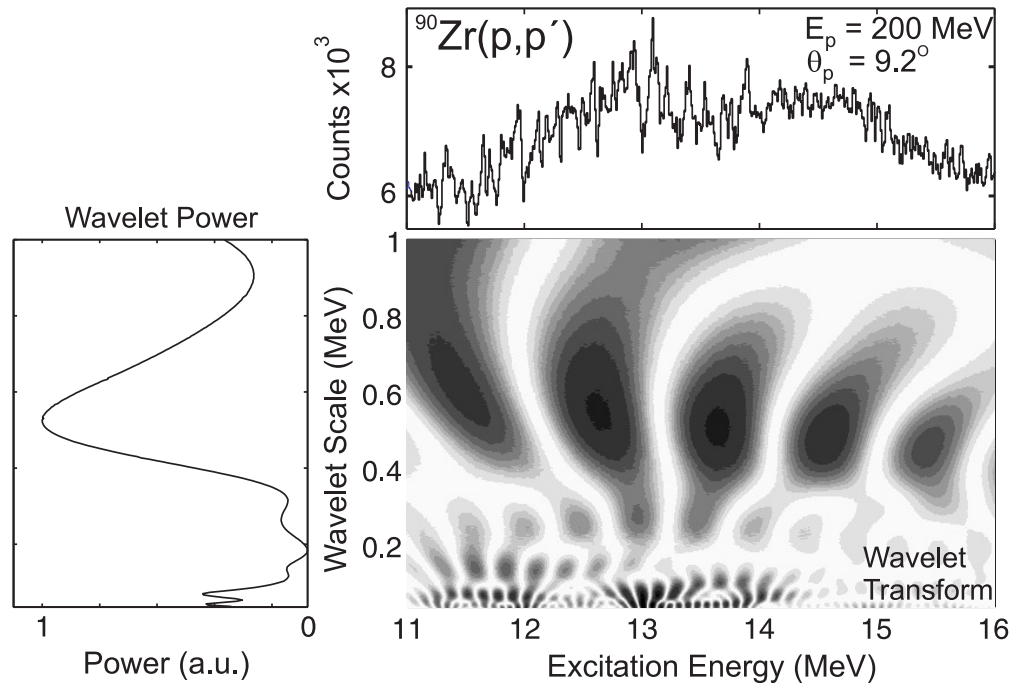


Fig. 6.7: The CWT of the $^{90}\text{Zr}(p,p')$ spectrum for $E_p = 200$ MeV and $\Theta_p = 9.2^\circ$ using the Morlet wavelet.

the (p,p') reaction on ^{120}Sn , ^{90}Zr , and ^{58}Ni , respectively. Again, one can see in all the measured spectra structures with different scales, and one can easily extract the values of these characteristic scales. Figure 6.9 displays the wavelet analysis

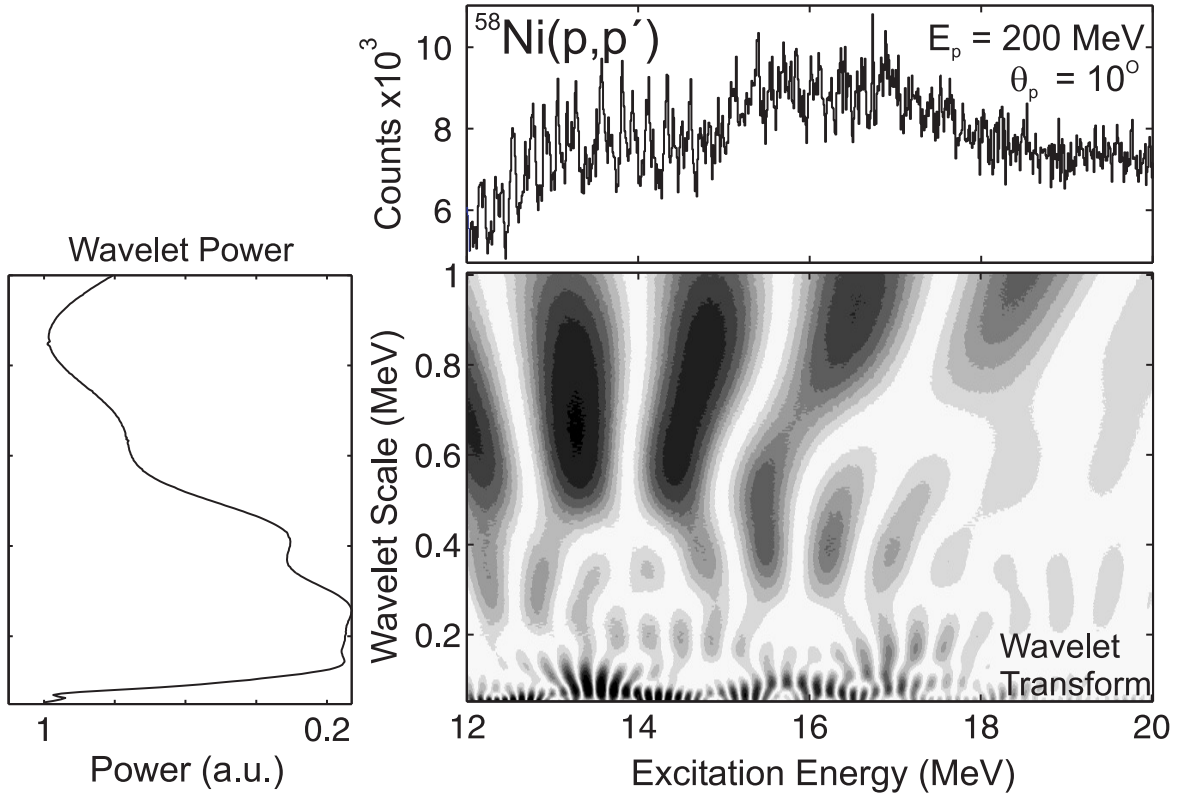


Fig. 6.8: The CWT of the $^{58}\text{Ni}(p,p')$ spectrum for $E_p = 200$ MeV and $\Theta_p = 10^\circ$ using the Morlet wavelet.

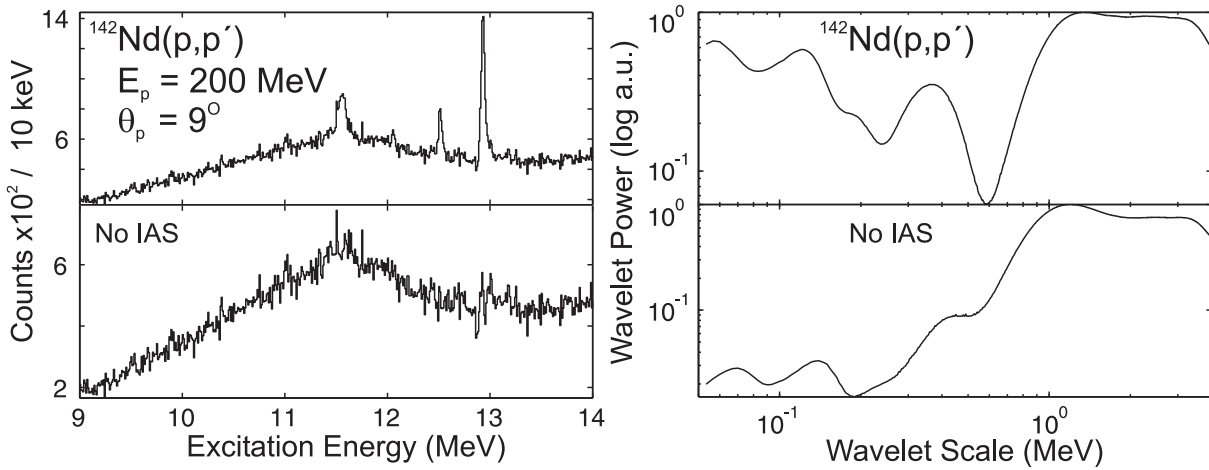


Fig. 6.9: Top: Spectrum of $^{142}\text{Nd}(p,p')$ at 9° (left) and its wavelet power (right). Bottom: Comparison with the case of subtracted strong states.

results for the GQR region in $^{142}\text{Nd}(p,p')$ reaction. One can extract several scales: 120 keV, 190 keV, 370 keV, 1300 keV, and 3200 keV. One may expect some influence from the strong peaks, superimposed on a resonance, on the extracted scales. The subtraction of these peaks leads to a disappearance of a 190 keV scale and a slight shift of all the other scales.

6.5.3 Importance of Wavelet Function Selection

As noted above, another advantage of the wavelet transform is the flexibility to use different wavelet functions, adapted to achieve the necessary resolution when extracting the values of the characteristic scales. This is demonstrated in Fig. 6.10 which shows power spectra obtained using four different wavelet functions (from top to bottom: Morlet, Bior3.9, Mexican Hat, Haar). Comparing the distributions of maxima and their separation, one observes better localization properties of the Morlet wavelet in comparison to the other three wavelets. The Haar wavelet gives the worst scale resolution. Evidently, of the four the Morlet wavelet is best-suited for the present task of the detection of characteristic scales in the nuclear response. Accordingly, this function was selected for carrying out the CWT analysis, described below. Another wavelet, the Bior3.9, which also shows good localizing properties, will be used in the discrete wavelet analysis.

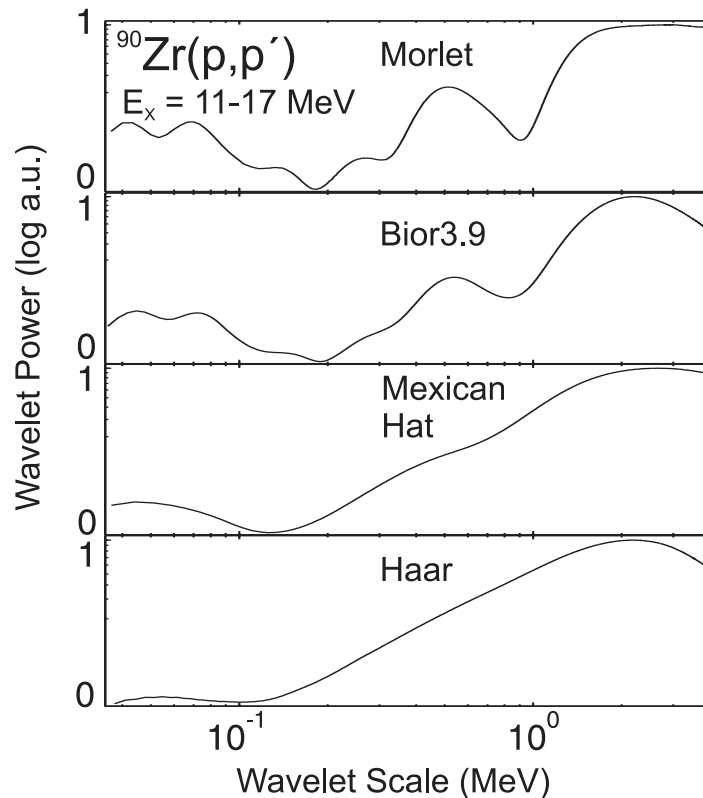


Fig. 6.10: Power spectra of the experimentally measured spectrum in the GQR region of ^{90}Zr nucleus using four different wavelet functions, from top to bottom: Morlet, Bior3.9, Mexican Hat, Haar. The latter has the worst scale resolution of all four functions, whereas Morlet function shows the best performance.

6.5.4 Role of Other Multipoles

The question whether the observed fine structure and characteristic scales really originate from the GQR can also be partially answered by studying the evolution of power spectra as a function of the scattering angle. For this purpose, the excitation energy spectra for two selected cases of ^{90}Zr and ^{208}Pb targets were taken for a larger scattering angle range above and below the maximum of the $\Delta L = 2$ excitations, thereby enhancing contributions of other multipoles and suppressing the GQR. The results of the wavelet analysis for ^{90}Zr are shown in Fig. 6.11 for $\Theta_p = 9.2^\circ$, 11° , and 13° , with the spectra on the left-hand side and wavelet power spectra on the right-hand side. The power is normalized so that the smallest scale (experimental resolution) has unit power. This normalization removes any dependency on the statistics of the spectra, and the power at different angles can be compared directly. The same scales are observed at all three scattering angles. Therefore, the impact of other multipoles on the scales of the GQR, is negligibly small. As the GQR cross section is getting weaker, the power of large scales decreases.

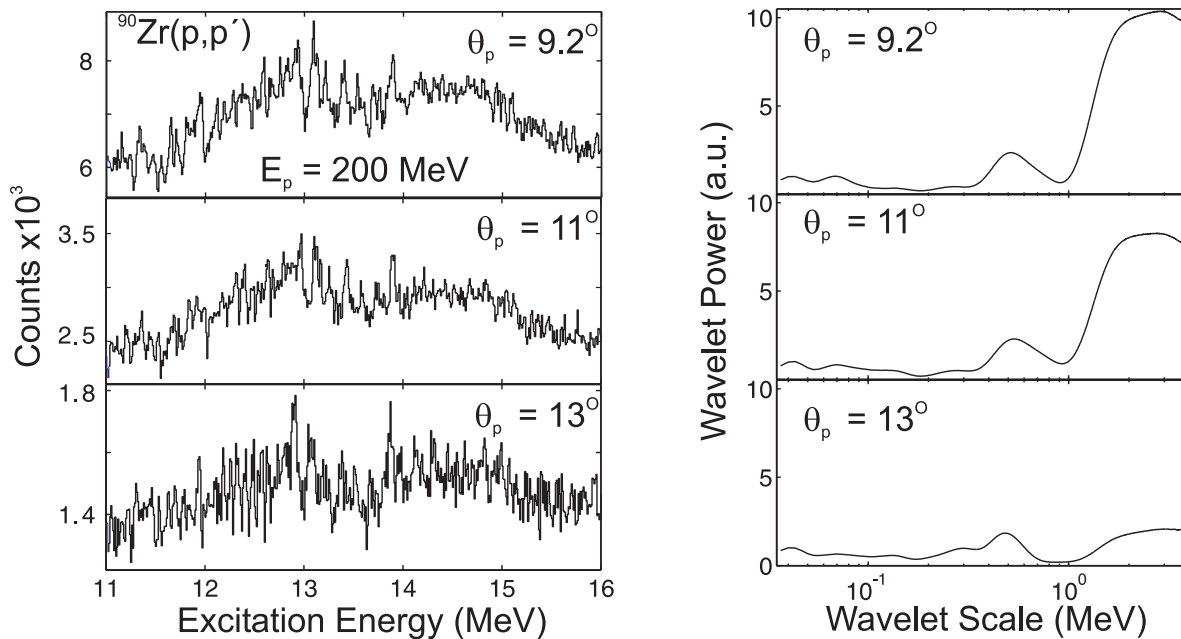


Fig. 6.11: Power spectra for $^{90}\text{Zr}(p,p')$ at three different scattering angles. At 9.2° the GQR is excited mostly, getting weaker at larger angles. The wavelet power spectra show no appearance of new scales at larger angles. The power of large scales is decreasing with the scattering angle, in conformity with the decrease of GQR strength.

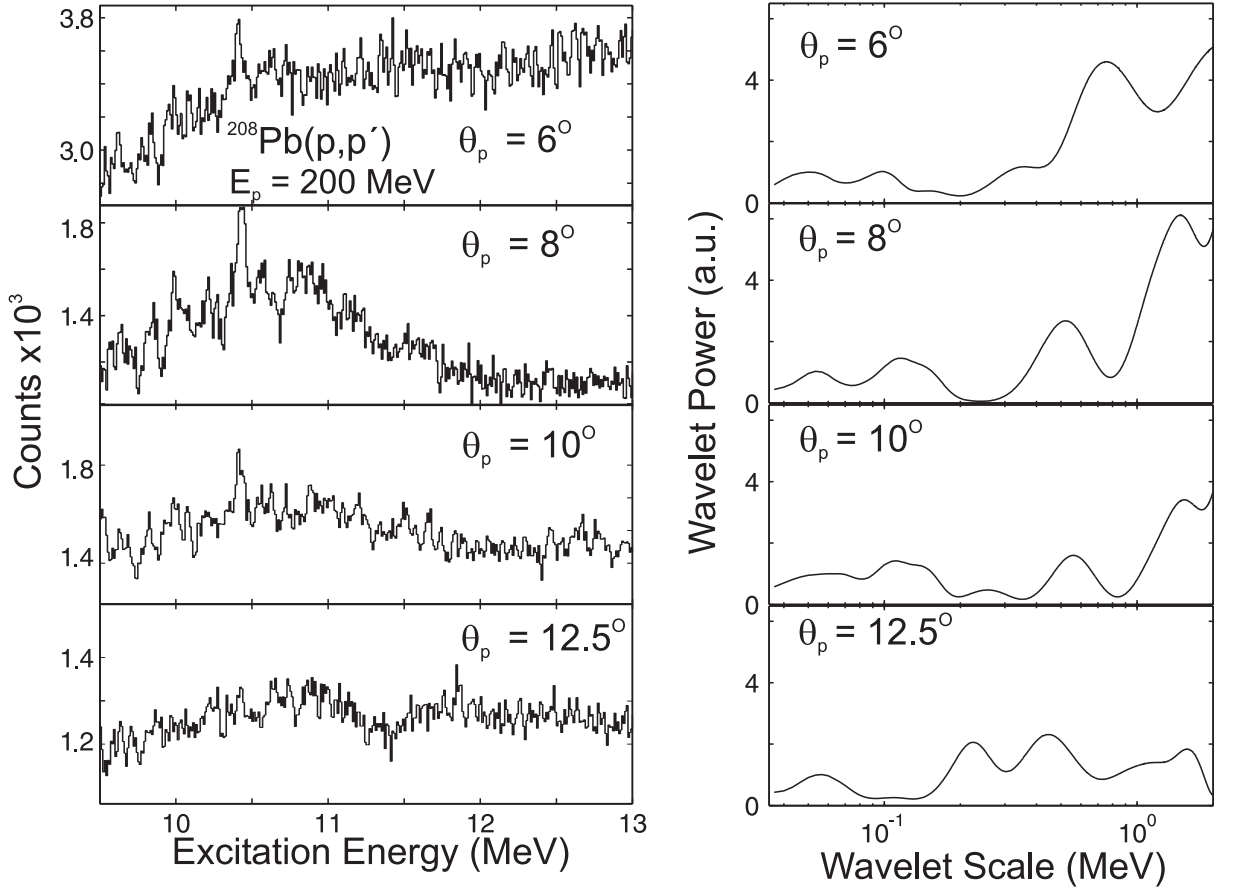


Fig. 6.12: Same as Fig. 6.11 for the $^{208}\text{Pb}(p,p')$ reaction. Maximum of the GQR cross section lies close to 8° . The GQR is getting weaker at larger scattering angles.

Similar results for the ^{208}Pb target, shown in Fig. 6.12, are more difficult to interpret. At $\Theta_p = 6^\circ$ the spectrum contains considerable instrumental background. The 310 keV and 700 keV scales present at the most forward angle are discontinued at $\Theta_p = 8^\circ$ and larger scattering angles, meaning that these scales are of other nature than the quadrupole resonance. In contrary to this, the 110 keV scale increases in power as one moves from 6° to 8° . All scales, present in the maximum of the ISGQR at 8° , are getting weaker in power at larger angles, similarly to the case of ^{90}Zr , thereby supporting the hypothesis of their origin from the quadrupole mode. At 10° a new scale of 230 keV appears, and gets even stronger at 12.5° , whereas the 110 keV scale, on the contrary, almost disappears. So, in the case of the GQR in ^{208}Pb , multipoles other than $\Delta L = 2$ might affect the scaling information. Nevertheless, in the maximum of quadrupole excitations at 8° there is no evidence of any scales caused by other multipoles.

6.5.5 Role of Shell Closures and Deformation

Nuclear shell structure plays an important role in defining decay properties of giant resonances in different nuclei. Figure 6.13 can provide some qualitative insight into these aspects, where two neighboring nuclei ^{90}Zr and ^{89}Y are compared in terms of fine structure and power distributions. In the ^{90}Zr nucleus more power is concentrated in large scales, describing the gross structure, whereas in the ^{89}Y nucleus a larger level density makes high-frequency fluctuations more pronounced as compared to the intermediate scales. Also remarkable is the appearance of another scale of 850 keV and a strong enhancement of the 120 keV scale in ^{89}Y as compared to the ^{90}Zr case. The difference may come from the isobaric analog state (IAS) in ^{89}Y at 13 MeV, which might cause the appearance of new scales. In order to check its contribution, the IAS was cut out of the spectrum of ^{89}Y , and the analysis repeated. The result is shown in the lower part of Fig. 6.13. No any significant differences in the wavelet power spectrum can be observed.

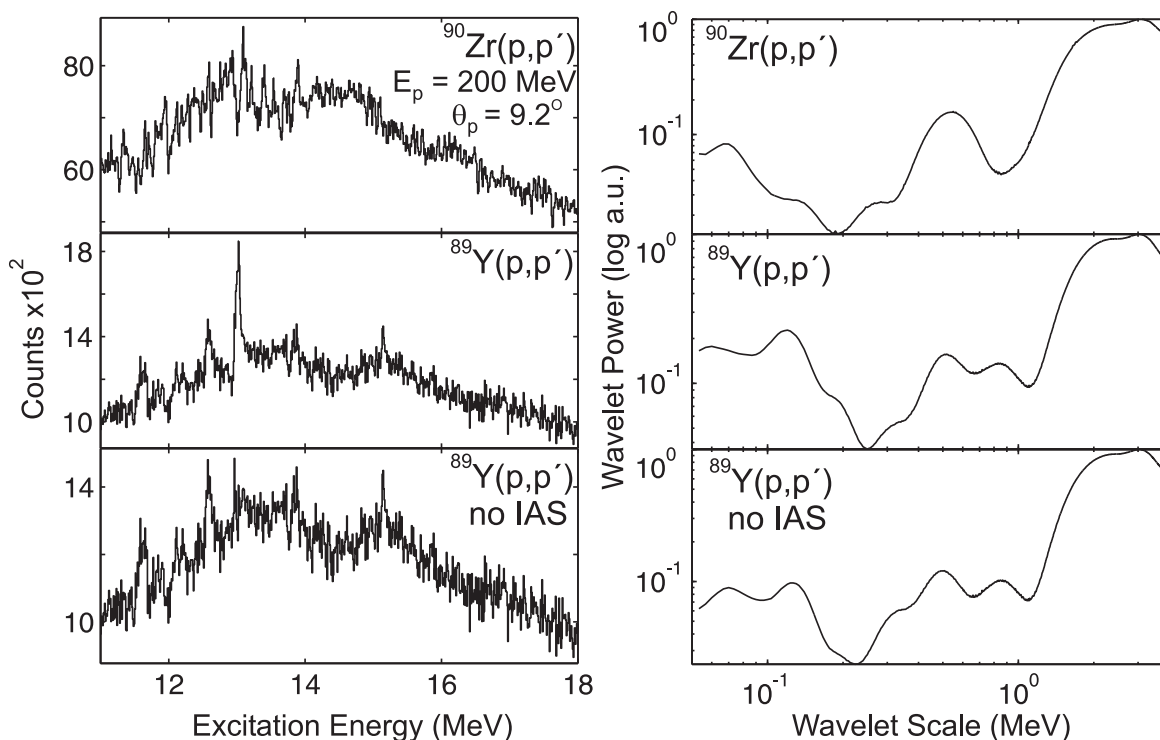


Fig. 6.13: Comparison of spectra (left) and wavelet power distributions (right) in $^{90}\text{Zr}(p,p')$ and $^{89}\text{Y}(p,p')$ reactions (top and middle plots, respectively) at 9.2° . Additional scale of 850 keV appears in ^{89}Y . Bottom plot: subtracting IAS at 13 MeV from the spectrum of $^{89}\text{Y}(p,p')$ does not change the result.

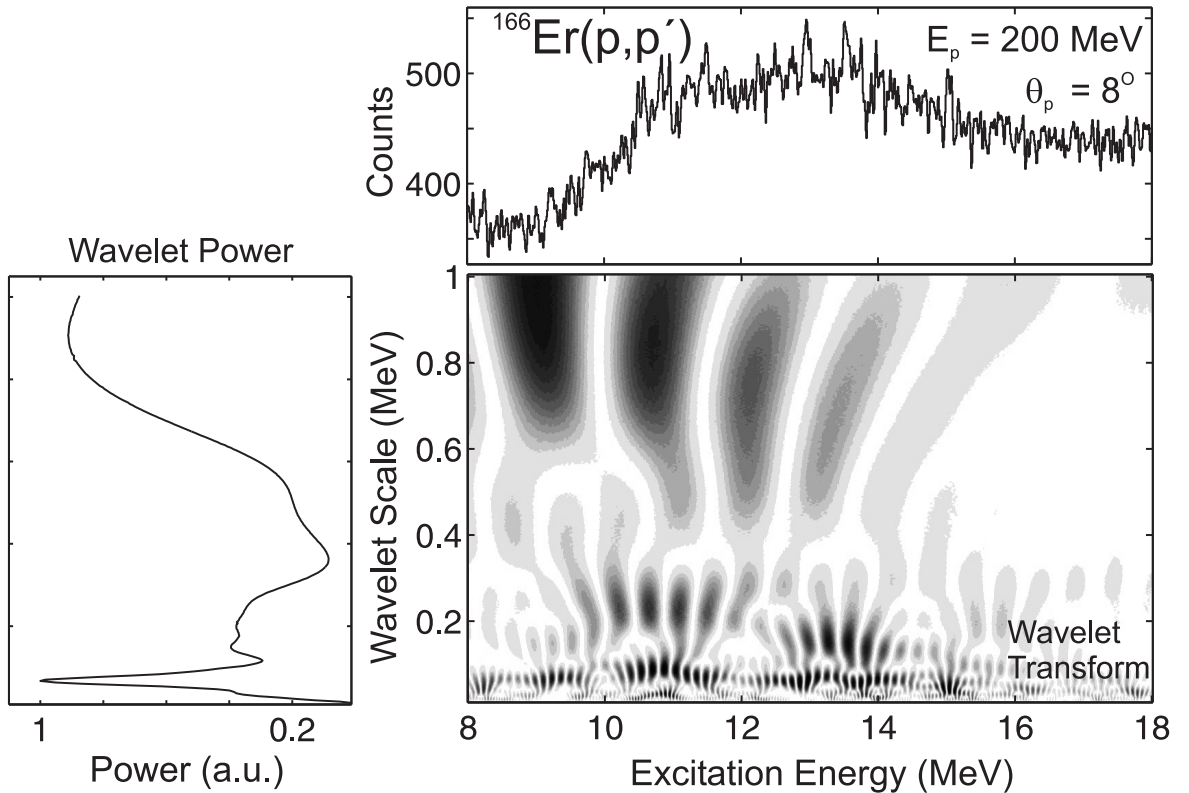


Fig. 6.14: The CWT of the $^{166}\text{Er}(p,p')$ spectrum for $E_p = 200 \text{ MeV}$ and $\Theta_p = 8^\circ$ using the Morlet wavelet.

Figure 6.14 displays the CWT analysis for the GQR region in a deformed ^{166}Er nucleus. The wavelet analysis detects a complex pattern of fluctuations. The wavelet power shows the appearance of several scales. Definitely, a more thorough systematic study of fine structure and scaling information in relation to shell and deformation effects needs to be carried out in order to draw out more definite statements.

6.5.6 Summary of Extracted Scales in the ISGQR Region

All the wavelet power distributions for experimental spectra in the region of quadrupole resonance are shown in Fig. 6.15. A global analysis of all obtained experimental data reveals three general classes of scales, which are summarized in Tab. 6.1. Class I contains a scale around 100 keV which was observed in all the nuclei studied. Several intermediate energy scales of the order of several hundreds of keV belong to Class II. The values of these scales vary rather strongly from nucleus to nucleus. The third class contains the largest observed scales of several MeV which reflect the gross structure and the total width of the resonance.

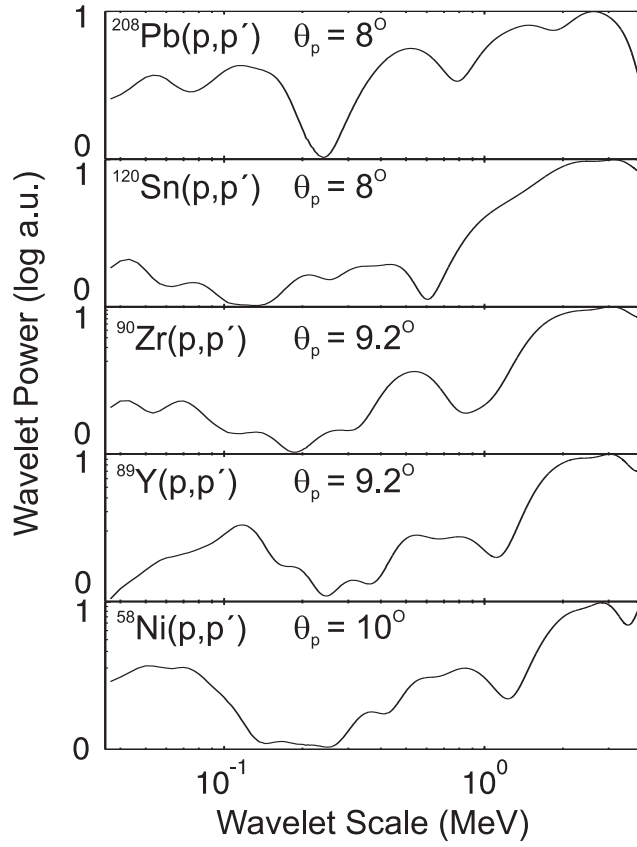


Fig. 6.15: Wavelet power distributions from the experimental spectra in the region of the ISGQR in (top to bottom): ^{208}Pb , ^{120}Sn , ^{90}Zr , ^{89}Y , ^{58}Ni .

Tab. 6.1: Summary of the scales observed experimentally (in keV).

| Nucleus | I | II | III |
|-------------------|-----|-----------------|-----------|
| ^{208}Pb | 110 | 500 | 1500 2600 |
| ^{166}Er | 150 | 250 880 | 2260 3260 |
| ^{142}Nd | 130 | 420 | 1200 3200 |
| ^{120}Sn | 80 | 220 330 470 | 1100 3200 |
| ^{90}Zr | 70 | 140 260 540 | 2100 3100 |
| ^{89}Y | 120 | 190 320 540 830 | 2100 3100 |
| ^{58}Ni | 70 | 170 360 580 850 | 2800 4700 |

6.6 Discrete Wavelet Analysis

The discrete wavelet transform (DWT) can be understood as the application of low-pass (large scales δE) and high-pass (small scales δE) filters on the spectrum separating it into a so-called *approximation* (A) and the *details* (D), respectively, as shown in Fig. 6.16. Starting at the smallest possible scale ($j = 1$) one can reconstruct the original spectrum exactly as $\sigma(E) = A1 + D1$. In the second step, A1 can be further decomposed into A2+D2, and so forth. Figure 6.17 presents an application of the method [83] to the spectrum of $^{208}\text{Pb}(p,p')$ reaction measured at $\Theta_p = 8^\circ$. In the topmost panels the spectrum is shown, underneath are the approximations A_i (left-hand side) and details D_i (right-hand side) at different decomposition levels i . Each level corresponds to a certain range of scales, given at the right-hand side. At each step the scale range increases by a factor of two. One finds that the details D_i corresponding to certain ranges of scales (e.g. D_3, D_4, D_5, D_7, D_8) are more important, whereas other details D_1, D_2 and D_6 are less significant. One advantage of the present method over the entropy index method is the possibility to distinguish whether scales are globally seen over the whole spectrum or rather localized at certain energy regions.

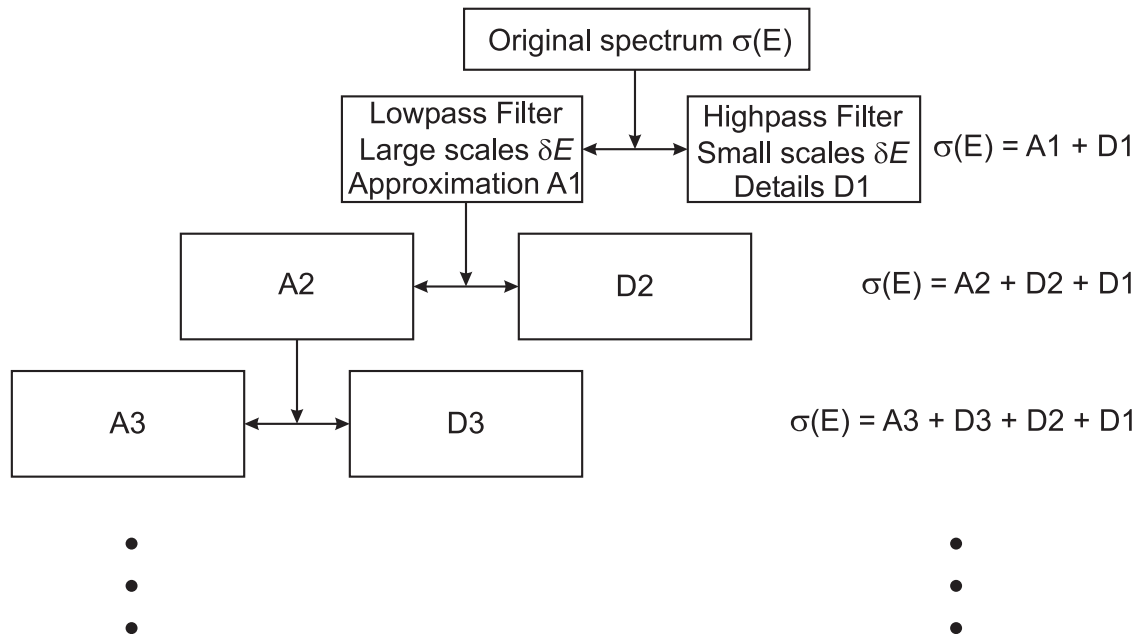


Fig. 6.16: Schematic representation of the discrete wavelet transform as a decomposition of a signal into different frequency components using a set of band-pass filters.

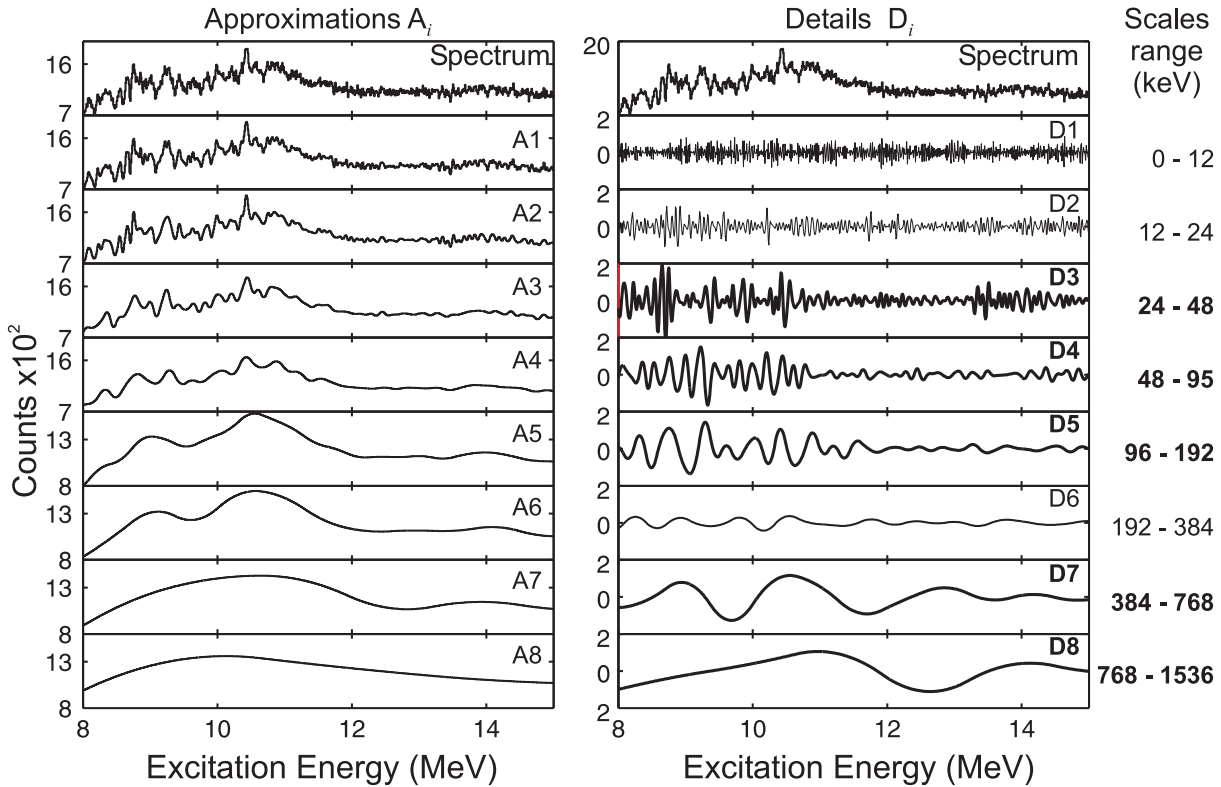


Fig. 6.17: The discrete wavelet transform decomposition of the $^{208}\text{Pb}(p,p')$ spectrum measured at $E_p = 200$ MeV and $\Theta_p = 8^\circ$ into the approximations A_i and details D_i .

While the possibility for a precise determination of characteristic scales with the DWT is strongly limited, a big advantage of the method is that the decomposition is reversible. This allows for a direct test of the importance of different scale regions for the reproduction of the observed fine structure patterns. The left-hand side of Fig. 6.18 shows a comparison of the original spectrum (top) with the one reconstructed from the sum $A_8 + D_8 + D_7 + D_5 + D_4 + D_3$ (middle). The fluctuations can be reproduced remarkably well. The bottom part of Fig. 6.18 shows the relative errors of such a reconstruction, which is generally less than 10%. If one, on the other hand, takes the sum of A_8 with the scales predicted to be less important (right-hand side of Fig. 6.18), only a rather poor reconstruction of the original spectrum is achieved. Similar results of the decomposition within the DWT analysis for the case of GQR in ^{90}Zr are shown in Fig. 6.19. A good reconstruction can be achieved by taking A_8 and $D_8, D_7, D_4, D_3,$ and D_2 as is presented in Fig. 6.20. These results confirm the scale values from the CWT analysis.

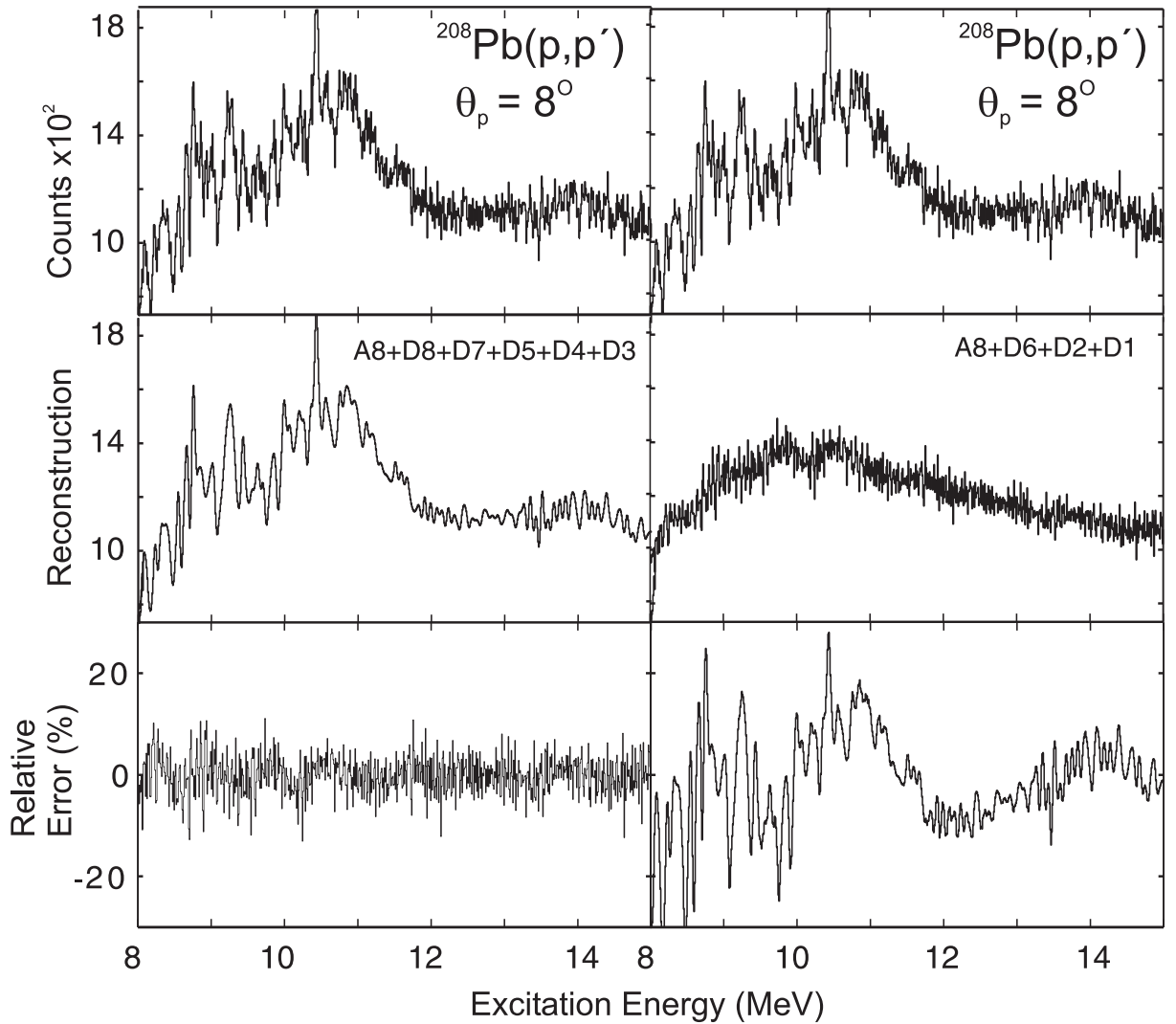


Fig. 6.18: The experimental spectrum (top panels) and its reconstruction (middle panels) from the decomposition in a discrete wavelet analysis analog to Fig. 6.16, including either the scale ranges predicted to be important (left-hand side) or unimportant (right-hand side). Bottom plots show relative errors of the reconstruction, which are in one case much smaller than in another one.

Thus, the discrete wavelet analysis is indeed capable of separating out the scale regions which carry the information about the fine structure and to test their importance directly. The experience shows that this method works quite well in cases where one has only few well-separated scales, so that most of the levels of decomposition (see Fig. 6.16) can be excluded. In the case of the GQR this seems to be somewhat problematic, since one really has several closely-lying scales, so that almost each level of decomposition contains one or two scales and should be taken for a proper reconstruction of the fine structure. Moreover, if a scale value

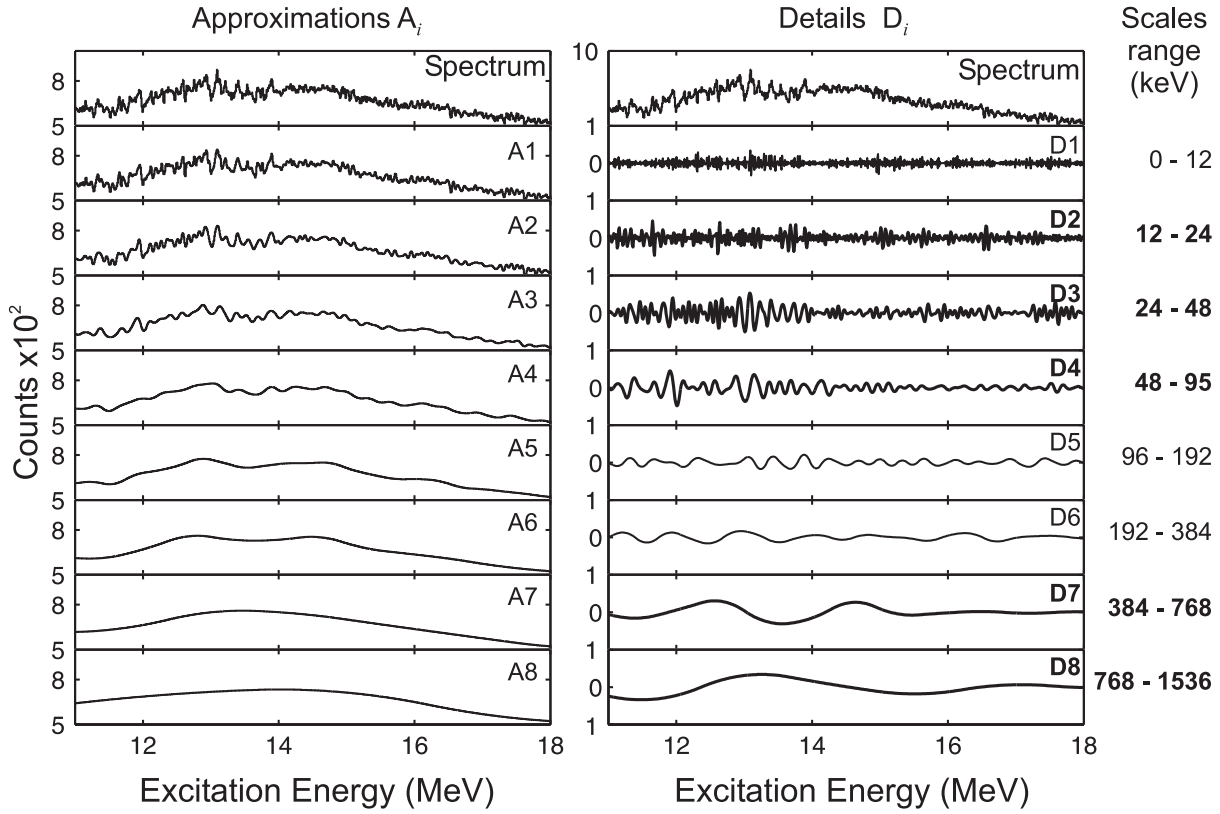


Fig. 6.19: Same as in Fig. 6.17 for the case of $^{90}\text{Zr}(p,p')$ at $E_p = 200$ MeV and $\Theta_p = 9.2^\circ$.

lies close to the boundary between two scale ranges, its power will be distributed over both ranges, which might further complicate the interpretation of obtained results. Still, a cross-consistency check using the DWT is of great help.

A very practicable method to quantitatively estimate the importance of each decomposition level is based on calculating the squared wavelet coefficients from the details of the DWT, as shown in Fig. 6.21. Plotted there is the sum of squared details, normalized to unity, as a function of the level of decomposition. At certain levels there are clear maxima and minima, reflecting the significance of the corresponding scale ranges. Thus, in the case of ^{208}Pb (left-hand side), at level 6 a strong minimum is observed meaning that no characteristic scales are present in the region 192-384 keV, which is consistent with the results of the CWT analysis, carried out above. The similar picture for ^{90}Zr , shown in the right-hand side of Fig. 6.21, reveals that levels 1, 5 and 6 are not significant for fine structure characterization, as it was just found from the reconstruction procedure. Two scales from Tab. 6.1 for ^{90}Zr belong to one such unimportant range. However, observing Fig. 6.15, one can conclude that the magnitudes of these scales are weak, so that

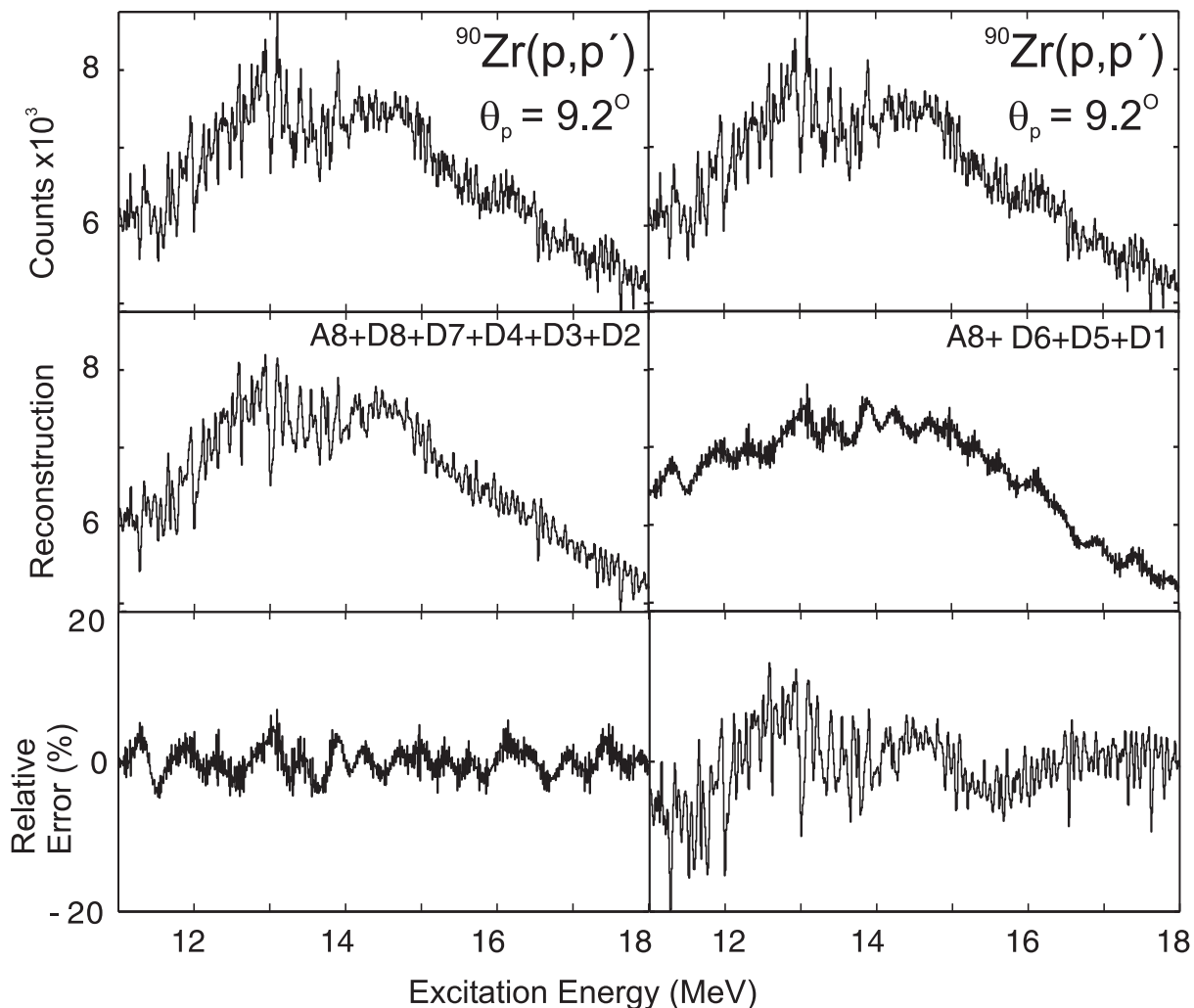


Fig. 6.20: Same as in Fig. 6.18 for $^{90}\text{Zr}(p,p')$ reaction at $E_p = 200$ MeV and $\Theta_p = 9.2^\circ$.

their significance is questionable. This represents a good example for a check of relevance of scales, using the discrete wavelet transform.

It is also useful to plot the squared details as a function of scale range, as shown in the upper part of Fig. 6.22. A direct comparison of obtained distributions with the wavelet power spectra obtained from the CWT analysis (lower part of Fig. 6.22) is to be made. Indeed, a very good correspondence between the scale ranges in the DWT analysis and the wavelet power spectra from the CWT demonstrates the consistency of the two techniques.

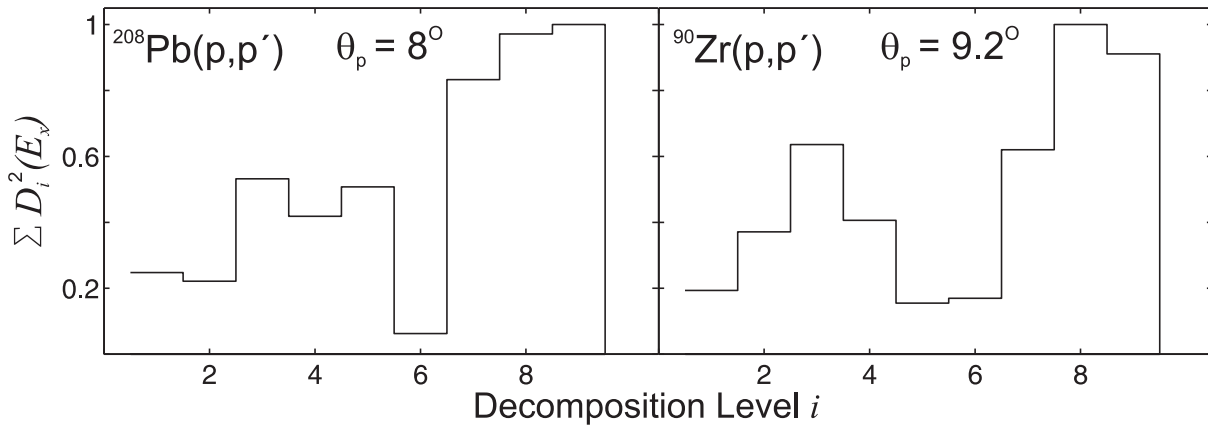


Fig. 6.21: Sum of squared details of the DWT of ^{208}Pb (left-hand side) and ^{90}Zr (right-hand side), as a function of the decomposition level.

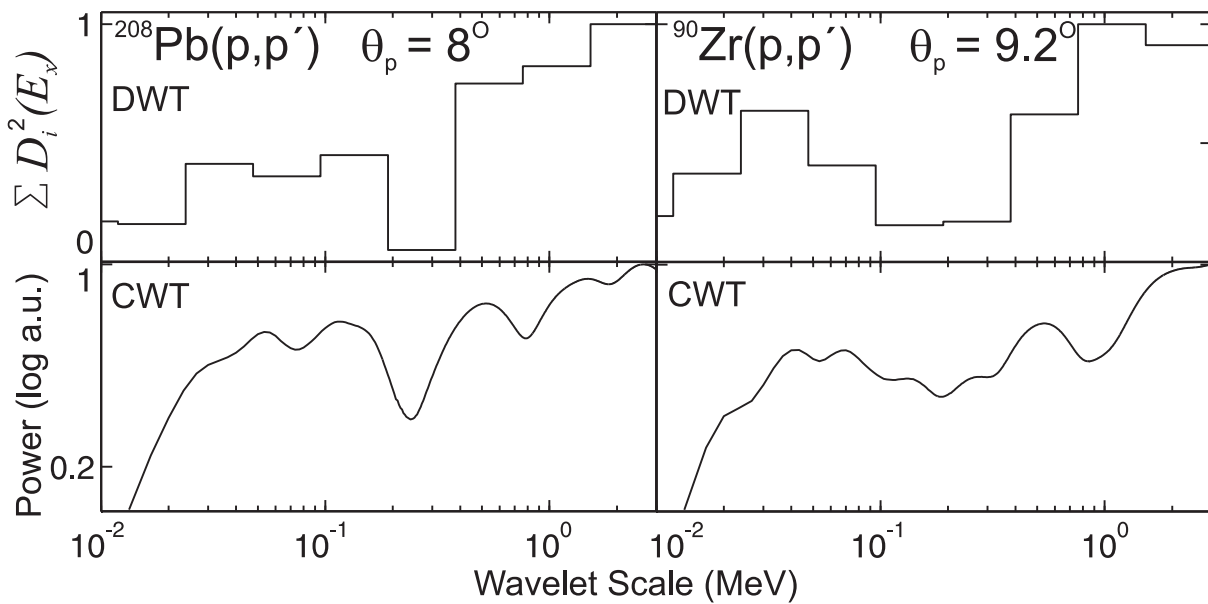


Fig. 6.22: Consistency of the DWT and the CWT results. Upper part: Sum of squared details from the DWT applied to ^{208}Pb (left) and ^{90}Zr (right), as a function of the wavelet scale range. Lower part: Corresponding wavelet power spectra from the CWT.

7 Fine Structure and Microscopic Models for the Damping of Giant Resonances

Precise information on the scales present in the excitation energy spectra of giant resonances is of particular interest since it may help in understanding which mechanisms are dominant for the decay. However, the interpretation of the fine-structure scales is still far from being straightforward. Proper understanding of the observed subtle phenomena is impossible to accomplish without the help of the modern sophisticated microscopic models.

For a physical interpretation of the obtained results, one has to compare them with the microscopic predictions for the strength functions of the collective mode studied, discussed in the next section. On the other hand, fine structure with its characteristic scales may serve as a stringent test for the validity and further improvement of the microscopic description of collective excitations in atomic nuclei. The experimental data set obtained on a number of different closed-shell and near-closed-shell nuclei provides a real challenge for modern microscopic nuclear structure calculations.

7.1 Mean Field Approximation

The mean-field approximation can be, for example, described theoretically using a Time-Dependent Hartree-Fock (TDHF) approach [19, 29]. It is based on the Vlasov equations of the time evolution of a one-body density matrix. This approach can treat, in principle, any type of motions in the mean field, even those with large-amplitude oscillations. However, the practical treatment is in general rather complicated. For the description of giant resonances, one linearizes the equations under the assumption that one has only small-amplitude vibrations. This reduces the TDHF formalism to the Random-Phase Approximation (RPA) equations [19, 29].

In this approach the nucleons move independently in the average potential. The

quasiparticles (qp) only interact via the mean field. This excludes damping phenomena which are related to residual collisions of *quasiparticles* in the mean field. Nonetheless, there exists a damping mechanism which is of purely quantum-mechanical origin. The damping effects contained in this description are usually referred to as *one-body dissipation*. One of them is *Landau damping*. In a finite nucleus it occurs as a mixing between the collective state and the nuclear $p - h$ excitations. In some cases, e.g. in light nuclei, *Landau damping* may introduce a fragmentation of initial $1p - 1h$ doorways and produce a typical scale. A second damping mechanism is induced by a direct particle emission from the initial $1p - 1h$ state, leading to an escape width Γ^\uparrow (see Fig. 2.3). However, as discussed in the next chapter, qualitative agreement with high-resolution experimental data can only be achieved including two-body effects, such as in extended RPA approaches that go beyond the mean field. It has been shown that the coupling of $1p - 1h$ to $2p - 2h$ states gives significant effects (see e.g. [43, 86, 87]).

7.2 Models Beyond the Mean Field

One-body dissipation from the nuclear mean field appears to be insufficient to describe observed resonance broadenings. A so-called *collisional damping* or *two-body dissipation* is needed to account for the widths. An extension for these effects involves complicated parts of the two-body density matrix. There exist several approaches that have been proposed for the description of the damping of giant resonances, including internal mixing. Figure 7.1 summarizes microscopic calculations for the E2 response function in ^{208}Pb in comparison with the experimental findings of the recent data. Structure functions calculated within the second random phase approximation (SRPA) [27], *extended time-dependent Hartree-Fock* (ETDHF) [88], *extended theory of finite Fermi systems* (ETFFS) [43], and *quasiparticle-phonon* model (QPM) [89] are shown. The predictions differ substantially, each having a unique fragmentation of the collective strength over different ranges of excitation energies. In the following section, a brief discussion of each approach will be given.

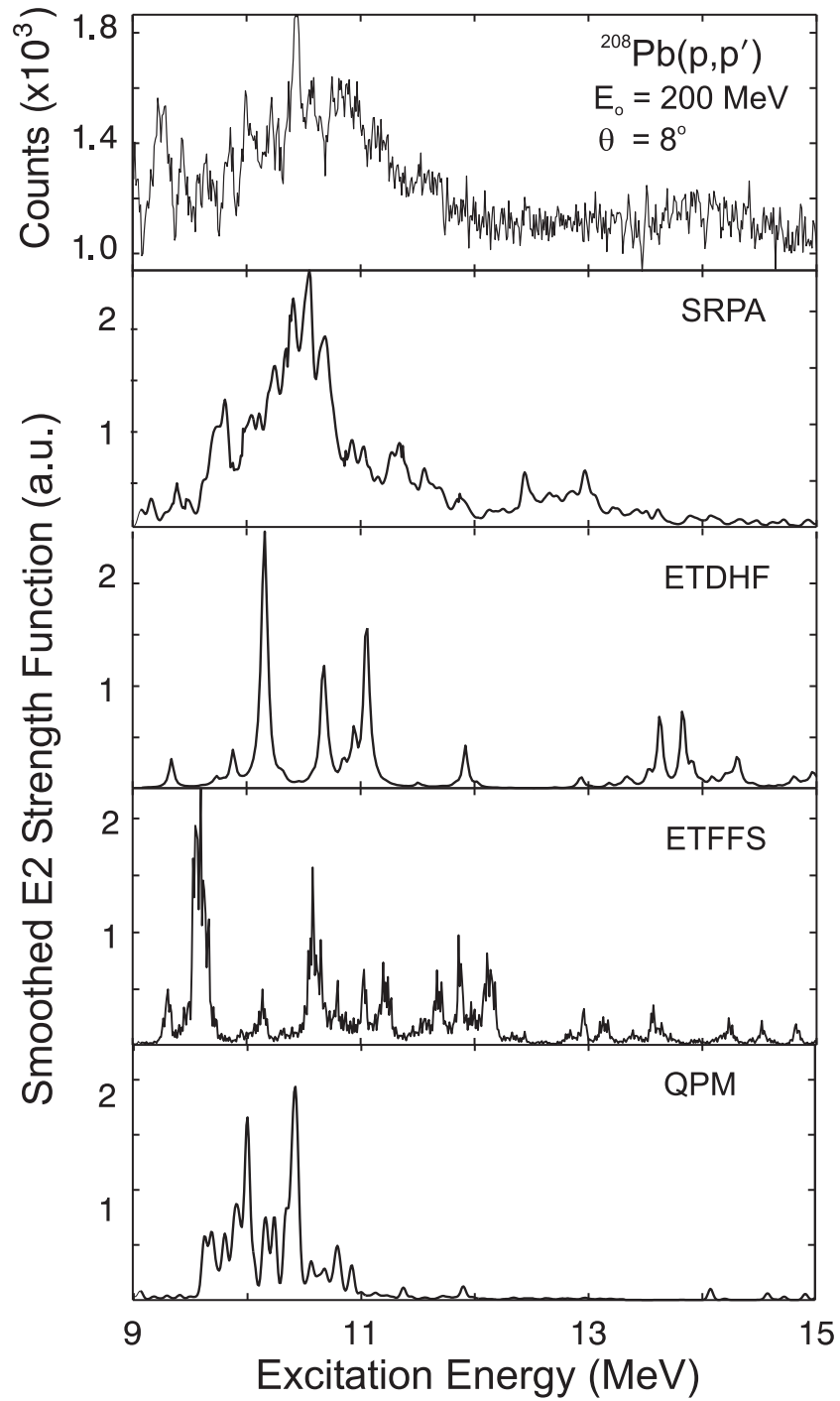


Fig. 7.1: Experimental spectrum of ^{208}Pb at 8° compared to microscopic model calculations for the GQR, including coupling to more complex configurations (top to bottom): SRPA [27], ETDHF [88], ETFFS [43], QPM [89]. All models predict slightly different centroid energies, fragmentations, widths, and fine structure of the GQR.

7.2.1 Second-RPA Model

A small-amplitude limit of the generalized theory, the so-called second Random-Phase Approximation (SRPA), involves $1p - 1h$ as well as $2p - 2h$ excitations of the static ground state. The solutions of the SRPA equations are obtained numerically, using several approximation schemes, which separate out the most relevant degrees of freedom. The SRPA has been successfully used for the description of damping of giant resonances (see e.g. [86, 90]).

The SRPA calculation shown in Fig. 7.1 was taken from [27] and is based on the M3Y interaction [59] with an adjusted short-range part for reproducing the experimental centroids of the low-multipolarity electric giant resonances in ^{208}Pb . A truncation of the $2p - 2h$ configuration space was made at $E_x = 20$ MeV. At this limit one includes about 1.5×10^4 $2p - 2h$ states. Details of the calculation are described in [91].

The method used here focuses on diagonal matrix elements in the $2p - 2h$ subspace. Their distribution can be approximated by a Gaussian, assuming random fluctuations. All configurations associated with matrix elements exceeding this Gaussian fit are included in the further analysis (about 3000 in the present example). The complex SRPA self-energy is chosen to attain a finite resolution similar to the experimental data. At the RPA level, the strength function consisted essentially of a single collective state around 12 MeV. By introducing $2p - 2h$ components, the FWHM strongly increased and fine structure appeared on top of the global shape.

7.2.2 Extended Time-Dependent Hartree-Fock Model

A similar approach is realized within the *extended time-dependent Hartree-Fock* (ETDHF) model, again linearizing the TDHF equations so that one has only the low-amplitude vibrations. One accounts for the damping due to the incoherent $2p - 2h$ decay in the form of a non-Markovian collision term [92, 93]. The isoscalar strength distribution for the GQR in ^{208}Pb given by the ETDHF by employing an effective Skyrme force is shown in the third row of Fig. 7.1. More detailed discussion of the model calculations can be found e.g. in [87, 88].

7.2.3 Extended Theory of Finite Fermi Systems

Another analogous method of describing damping of collective motion in atomic nuclei beyond the mean field theory is done within the *extended theory of finite Fermi systems* (ETFFS), where, in addition to the previously discussed damping mechanisms, namely *Landau damping* and more complex $1p1h \otimes \text{phonon}$ or $2qp \otimes \text{phonon}$ configurations, the coupling to the *single-particle continuum* is included.

An extension of Migdal's Theory of finite Fermi systems [94] was developed and applied to collective vibrations in closed shell nuclei in the past ten years. This microscopic approach is based on a consistent use of the Green function method. Here one considers in a consistent way more complex $1p - 1h \otimes \text{phonon}$ configurations beyond the RPA correlations. Moreover, these configurations are not only included in the excited states but also explicitly in the ground states of nuclei. A review of the theoretical approach is given in [95]. The result for the GQR in ^{208}Pb nucleus [43] is shown in the fourth row of Fig. 7.1. One can see that the coupling to the continuum leads to an additional broadening of the strength. This effect is, however, believed to be much more significant for a proper description of resonance damping in light and medium-heavy nuclei, where the role of the continuum is very important.

7.2.4 Quasiparticle-Phonon Model

Another approach permitting to include complex degrees of freedom equivalent to the SRPA is the *quasiparticle-phonon* model (QPM) [89, 96], which proved to be very successful in the microscopic description of different giant resonances [72, 97, 98]. Decisive features of such an approach are, firstly, a sophisticated way of diagonalizing the Hamiltonian, avoiding the need to treat large configuration spaces via a specific truncation scheme based on the properties of a coupling hierarchy. Secondly, it offers the possibility to separate different contributions to the damping in the nuclear response. This allowed for a further insight into the physical nature of the observed fine structure and scales. A more detailed description of the QPM theory will now be introduced, because the in-depth analysis presented in the next chapter will be based on these results.

In the QPM nuclear excitations are described by creations of *phonons* made up

from *particle-hole* pairs. Due to pairing correlations, the occupation probability for a state j is not exactly one or zero. These states are denoted as *quasiparticle* (qp) states. Since $1p - 1h$ pairs couple to an integer transfer of the quantum numbers, one can describe the transition as a creation of a boson, the so-called *phonon*. Note, however, that the term *phonon* is not reserved for collective states only, but applies to transitions with rather pure $1p - 1h$ character as well. The model can account not only for *1-phonon* transitions, but also for *multi-phonon* excitations.

A characteristic feature of the QPM is a *step-by-step* diagonalization of the Hamiltonian of the system. The Hamiltonian is first introduced on the basis of the mean field with a the residual interaction

$$\mathbf{H} = \mathbf{H}_{s.p.} + \mathbf{H}_{pair} + \mathbf{H}_{r.i.} . \quad (7.1)$$

The first term in (7.1) corresponds to the average field for neutrons (n) and protons (p) and is expressed in terms of operators for creation $\mathbf{a}_{jm\tau}^+$ and annihilation $\mathbf{a}_{jm\tau}$ of particles on the level of the average field with quantum numbers $j \equiv [n, l, j]$ and m in the form

$$\mathbf{H}_{s.p.} = \sum_{\tau} \sum_{j,m}^{n,p} E_{j\tau} \mathbf{a}_{jm\tau}^+ \mathbf{a}_{jm\tau} , \quad (7.2)$$

where E_j is the energy of the *single-particle* level degenerated in spherical nuclei by the magnetic quantum number m , and $\tau = -1(+1)$ means neutrons (protons).

The second term of (7.1) describes the residual interaction, responsible for pairing in non-magic nuclei. This interaction is described by monopole pairing with a constant matrix element $G_{\tau}^{(0)}$ which is treated as a parameter to be adjusted to experimental pairing energies

$$\mathbf{H}_{pair} = \sum_{\tau} G_{\tau}^{(0)} \sum_{j,j'} \sqrt{(2j+1)(2j'+1)} [\mathbf{a}_{jm\tau}^+ \mathbf{a}_{j-m\tau}^+]_{00} [\mathbf{a}_{j'-m\tau} \mathbf{a}_{j'm\tau}]_{00} , \quad (7.3)$$

with

$$[\mathbf{a}_{jm\tau}^+ \mathbf{a}_{j'm'\tau}^+]_{\lambda\mu} = \sum_{m,m'} C_{jm,j'm'}^{\lambda\mu} \mathbf{a}_{jm\tau}^+ \mathbf{a}_{j'm'\tau}^+ , \quad (7.4)$$

where $C_{jm,j'm'}^{\lambda\mu}$ are Clebsch-Gordan coefficients. In a semi-magic nucleus the pairing term gives a non-zero contribution for open proton or neutron system. Since

the QPM is usually applied to medium and heavy nuclei with filling of different subshells of neutrons and protons, the neutron-proton monopole pairing is neglected.

Finally, the residual interaction $\mathbf{H}_{r.i.}$ is taken in the model in a separable form allowing a multipole decomposition. Its part in the *particle-hole* channel can be written as

$$\mathbf{H}_{r.i.}^{(p-h)} = \sum_{\lambda\mu} \sum_{\tau\rho}^{\pm 1} ((1-\rho)\kappa_0^{(\lambda)} + \rho\kappa_1^{(\lambda)}) \mathbf{M}_{\lambda\mu}^+(\tau) \mathbf{M}_{\lambda\mu}(\tau\rho), \quad (7.5)$$

where $\kappa_{0(1)}^{(\lambda)}$ are the model parameters which determine the strength of isoscalar (isovector) residual interaction and $\rho = 0(1)$ for isoscalar (isovector) transitions. The multipole operator $\mathbf{M}_{\lambda\mu}^+(\tau)$ is given by

$$\mathbf{M}_{\lambda\mu}^+(\tau) = \sum_{j,m,j',m'} \langle jm\tau | i^\lambda f_\lambda^\tau(r) \mathbf{Y}_{\lambda\mu}(\Omega) | j'm'\tau \rangle \mathbf{a}_{jm\tau}^+ \mathbf{a}_{j'm'\tau} \quad (7.6)$$

for natural parity states and by

$$\mathbf{M}_{\lambda\mu}^+(\tau) = \sum_{j,m,j',m',l m_1} \langle jm\tau | i^l f_l^\tau(r) [\sigma \cdot \mathbf{Y}_{lm_1}(\Omega)]_{\lambda\mu} | j'm'\tau \rangle \mathbf{a}_{jm\tau}^+ \mathbf{a}_{j'm'\tau} \quad (7.7)$$

for unnatural parity states. The function $f_\lambda^\tau(r)$ is a radial form factor which is taken either in form r^λ or as a derivative of the central part of the average field $f_\lambda^\tau(r) = dU^\tau(r)/dr$.

The solution of the Schrödinger equation is obtained by means of iterative diagonalization of the model Hamiltonian given by (7.1). The first two terms are diagonalized at the beginning. For this purpose, the Bogoliubov canonical transformation from particle creation (annihilation) operators to *quasiparticle* creation (annihilation) operators is applied

$$\mathbf{a}_{jm\tau}^+ = u_j \alpha_{jm\tau}^+ + (-1)^{j-m} v_j \alpha_{j-m\tau}. \quad (7.8)$$

The values u_j^2 and v_j^2 correspond to occupation probabilities for particles and holes in the shell j . The ground state of even-even nuclei is considered as *quasiparticle vacuum* $|\alpha_{jm\tau}\rangle_q \equiv 0$. The energy of the ground state is then minimized

$$\delta \{ \langle |\mathbf{H}_{s.p.} + \mathbf{H}_{pair}| \rangle_q + \sum_j \mu_j (u_j^2 + v_j^2 - 1) \} = 0, \quad (7.9)$$

where μ_j are Lagrange coefficients. The resulting BCS equations can be solved providing correlation functions $C_\tau = G_\tau^{(0)} \sum_j u_j v_j$ and chemical potentials λ_τ for neutron and proton systems. The coefficients of the Bogoliubov transformation can be calculated from these values according to

$$v_j^2 = \frac{1}{2} \left(1 - \frac{E_{j\tau} - \lambda_\tau}{\epsilon_{j\tau}} \right), \quad u_j^2 = 1 - v_j^2, \quad (7.10)$$

where $\epsilon_{j\tau}$ is the *quasiparticle energy*

$$\epsilon_{j\tau} = \sqrt{C_\tau^2 + [E_{j\tau} - \lambda_\tau]^2}. \quad (7.11)$$

Having diagonalized the first two terms of the model Hamiltonian, one can write

$$\mathbf{H}_{s.p.} + \mathbf{H}_{pair} = \sum_\tau \sum_{j,m}^{n,p} \epsilon_{j\tau} \alpha_{jm\tau}^+ \alpha_{jm\tau}. \quad (7.12)$$

Since the ground state is determined as a *quasiparticle vacuum*, the simplest excited states in the nucleus are *two-quasiparticle* states $\alpha_{jm\tau}^+ \alpha_{j'm'\tau}^+ | >_q$ which correspond to *particle-hole* transitions if monopole pairing vanishes. One can make a mapping into the space of *quasi-boson* operators and introduce the following *phonon* operator for multipolarity λ and projection μ

$$\mathbf{Q}_{\lambda\mu}^+ = \frac{1}{2} \sum_\tau \sum_{j,j'}^{n,p} \{ \psi_{jj'\tau}^{\lambda i} [\alpha_{j\tau}^+ \alpha_{j'\tau}^+]_{\lambda\mu} - (-1)^{\lambda-\mu} \phi_{jj'\tau}^{\lambda i} [\alpha_{j'\tau} \alpha_{j\tau}]_{\lambda-\mu} \}. \quad (7.13)$$

The total number of different *phonons* for a given λ should be equal to the sum of neutron and proton *two-quasiparticle* states coupled to the same angular momentum. An index i is used to number these *phonons*. The *phonons* $\mathbf{Q}_{\lambda\mu}^+$ in (7.13) are made up only from proton-proton and neutron-neutron *two-quasiparticle* configurations $[\alpha_{j\tau}^+ \alpha_{j'\tau}^+]_{\lambda\mu}$. The coefficients $\psi_{jj'\tau}^{\lambda i}$ and $\phi_{jj'\tau}^{\lambda i}$ can be obtained by diagonalization of the Hamiltonian in the space of *one-phonon* states $\mathbf{Q}_{\lambda\mu}^+ | >_{ph}$ using the variation procedure

$$\delta \left\{ \langle \mathbf{Q}_{\lambda\mu} \mathbf{H} \mathbf{Q}_{\lambda\mu}^+ | >_{ph} - \left(\frac{\omega_{\lambda i}}{2} \right) \left[\sum_{jj'} \{ (\psi_{jj'\tau}^{\lambda i})^2 - (\phi_{jj'\tau}^{\lambda i})^2 \} - 2 \right] \right\} = 0, \quad (7.14)$$

where $\omega_{\lambda i}$ is the energy of the i -th *phonon*. This yields the well-known RPA equations, whose solutions for each multipolarity λ^π give the spectrum of *one-phonon* excitations $\omega_{\lambda i}$.

For actual calculations, the average field for neutrons and protons is approximated by a phenomenological Woods-Saxon potential with parameters from [99]

$$U^\tau(r) = \frac{V_0^\tau}{1 + e^{(r-R_0^\tau)/a_0^\tau}} - \frac{\hbar^2}{\mu^2 c^2} \frac{1}{r} \frac{d}{dr} \left(\frac{V_{ls}^\tau}{1 + e^{(r-R_{ls}^\tau)/a_{ls}^\tau}} \mathbf{l} \cdot \mathbf{s} \right) + V_{Coul}(r), \quad (7.15)$$

including a central, a spin-orbit and a Coulomb term, respectively. After diagonalizing the model Hamiltonian in the space of *one-phonon* states it can be rewritten in terms of the *phonon* operators

$$\mathbf{H} = \sum_{\lambda\mu i} \bar{\omega}_{\lambda i} \mathbf{Q}_{\lambda\mu i}^+ \mathbf{Q}_{\lambda\mu i} + \mathbf{H}_{int.}, \quad (7.16)$$

where $\mathbf{H}_{int.}$ contains the remaining part of the residual interaction, which cannot be projected onto the space of the *phonon* operators. One can expand it in an infinite sum of even-number *phonon* operators. Taking into account only the first term of the expansion, i.e. only *two-phonon* operators, one can obtain the non-diagonal terms of the model Hamiltonian $\mathbf{H}_{int.}$ in the space of *phonon* operators in the form

$$\mathbf{H}_{int.} = \sum_{\substack{\lambda\mu i \\ \lambda_1\mu_1 i_1 \\ \lambda_2\mu_2 i_2}} U_{\lambda_2 i_2}^{\lambda_1 i_1}(\lambda i) \mathbf{Q}_{\lambda\mu i}^+ [\mathbf{Q}_{\lambda_1\mu_1 i_1} \mathbf{Q}_{\lambda_2\mu_2 i_2}]_{\lambda\mu} + h.c., \quad (7.17)$$

where the matrix elements of the interaction between one- and *two-phonon* configurations $U_{\lambda_2 i_2}^{\lambda_1 i_1}(\lambda i) = \langle \mathbf{Q}_{\lambda\mu i} | \mathbf{H} | [\mathbf{Q}_{\lambda_1\mu_1 i_1}^+ \mathbf{Q}_{\lambda_2\mu_2 i_2}^+]_{\lambda} \rangle$ can be calculated by making use of the internal fermion structure, i.e. from the amplitudes $\psi_{jj'}^{\lambda_1 i_1}$, $\phi_{jj'}^{\lambda_1 i_1}$, $\phi_{jj'}^{\lambda_2 i_2}$, $\psi_{jj'}^{\lambda_2 i_2}$, and $\psi_{jj'}^{\lambda i}$, $\phi_{jj'}^{\lambda i}$.

Accordingly, the wave function of excited states with angular momentum λ and projection μ is written as a composition of *one-phonon* and *two-phonon* configurations

$$|\Psi\rangle_{\lambda\mu} = \left(\sum_i R_i \mathbf{Q}_{\lambda\mu i}^+ + \sum_{\substack{\lambda_1\mu_1 i_1 \\ \lambda_2\mu_2 i_2}} P_{\lambda_2 i_2}^{\lambda_1 i_1} [\mathbf{Q}_{\lambda_1\mu_1 i_1}^+ \mathbf{Q}_{\lambda_2\mu_2 i_2}^+]_{\lambda\mu} \right) | \rangle_{ph}. \quad (7.18)$$

The coefficients R_i and $P_{\lambda_2 i_2}^{\lambda_1 i_1}$, together with eigenenergies of the states (7.18), are calculated from the diagonalization of the Hamiltonian (7.16) in the space of the states (7.18).

| | | | | |
|---|------------------------|------------------------------|------------------------------|---|
| I | Q^+ 1p-1h | $Q^+ \leftrightarrow Q^+Q^+$ | 0 | ⋮ |
| | Q^+ ↕ Q^+Q^+ | II Q^+Q^+ 2p-2h | Q^+Q^+ ↕ $Q^+Q^+Q^+$ | ⋮ |
| | 0 | Q^+Q^+ ↕ $Q^+Q^+Q^+$ | III $Q^+Q^+Q^+$ 3p-3h | ⋮ |
| ⋮ | ⋮ | ⋮ | ⋮ | |

Fig. 7.2: Diagonalization scheme within the QPM.

The *step-by-step* diagonalization procedure is schematically depicted in Fig. 7.2.

The calculated ISGQR strength distribution in ^{208}Pb is shown in the bottom panel of Fig. 7.1. One can see that the centroid energy of the resonance seen experimentally is well reproduced. However, the width given by the QPM is underestimated. (the possible reasons for this are the used interaction, the missing coupling to the continuum, or the truncation scheme). The applied two-step diagonalization is very useful for saving computational time. It allows a huge space of *two-phonon* configurations to be truncated by excluding the ones which have very small matrix elements. The omitted *two-phonon* configurations are believed to give almost no contribution to the damping process of collective *one-phonon* states. This leads to a significant reduction in the range of the matrices to be diagonalized. Another advantage of this calculation scheme is that it allows the disentanglement of various contributions to the damping of collective response in heavy nuclei by setting different truncation thresholds.

In the following chapter the results of the wavelet analysis, when applied to the predictions of the model discussed, are presented. Based on these results one can, in a novel quantitative way, judge on the ability of different models to describe the fine structure observed in the ISGQR.

8 Results and Discussion

8.1 Origin of Fine Structure

An interpretation of the physical nature of the characteristic energy scales obtained from experiment is possible only via a comparison with the results from microscopic calculations. Within the RPA model, where only $1p - 1h$ transitions are treated, the GQR strength is concentrated in just a few states. In the case of ^{208}Pb it is only one state, so that the response function shows no fine structure. Accordingly, as Fig. 8.1 demonstrates, the wavelet analysis does not detect any characteristic scales, except the trivial scale - a folding width of 50 keV, included for the comparison with experiment.

If one goes a step beyond mean field and includes the coupling to $2p - 2h$ configurations the GQR strength in ^{208}Pb shown in the top frame of Fig. 8.2 fragments into many states and the fine structure appears. By way of example the SRPA calculation is discussed as a representative case. The wavelet transform in the

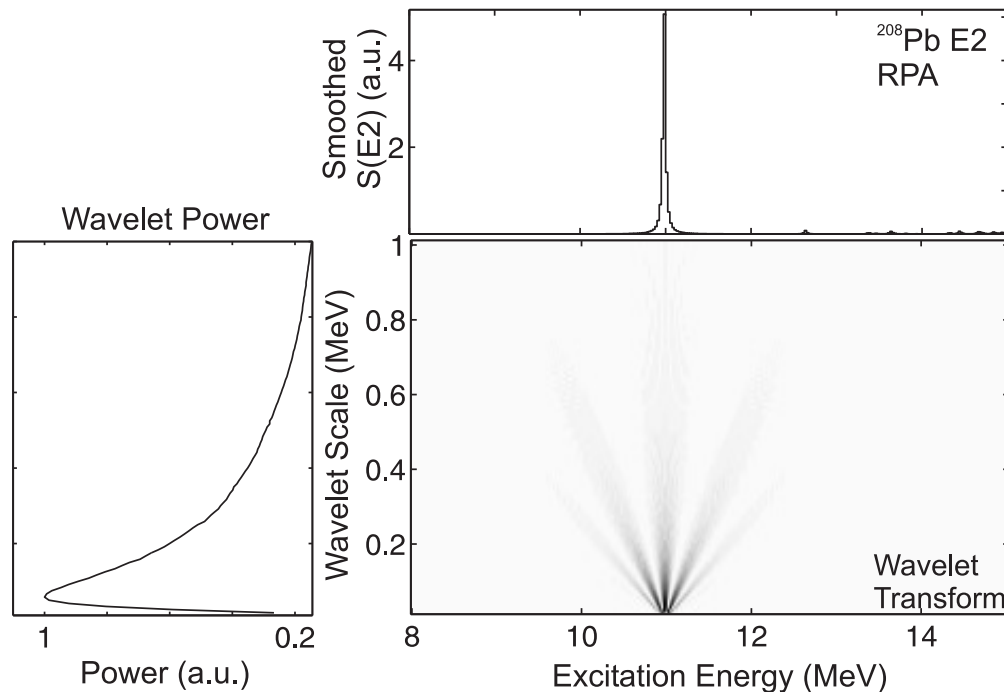


Fig. 8.1: The CWT of the E2 response in ^{208}Pb nucleus predicted within the RPA model. The strength is concentrated in one state, and there is no fine structure. The wavelet analysis also reveals no scales.

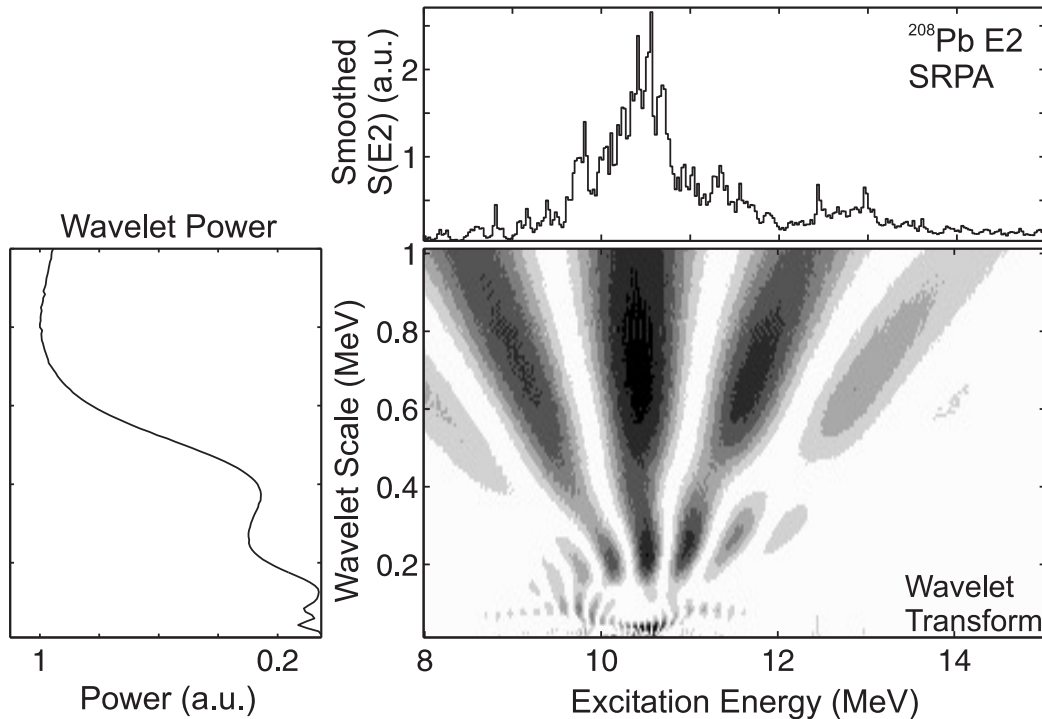


Fig. 8.2: The CWT of the E2 response in ^{208}Pb nucleus predicted by the SRPA calculations.

middle of Fig. 8.2 and the power spectrum on the left-hand side exhibit several characteristic scales. This fact is a demonstration of the significance of coupling to $2p-2h$ configurations for the formation of fine structure and related characteristic scales, found in the experimental spectra.

8.2 Comparison of Extracted Scales

The present data on the ISGQR in ^{208}Pb provide a remarkable opportunity for an in-depth comparison of theory and experiment. A variety of microscopic calculations, including the coupling to $2p-2h$ configurations with different truncation schemes and using different effective interactions, is available for this doubly-magic nucleus. The strength distributions calculated with SRPA, QPM, ETDHF, and ETFFS, are plotted in Fig. 7.1, together with the experimentally measured excitation spectrum. This allows a detailed comparison to be made for the characteristic scales obtained from the experiment vs. those from different model predictions, as it is shown in Figure 8.3. The wavelet analysis, therefore, repres-

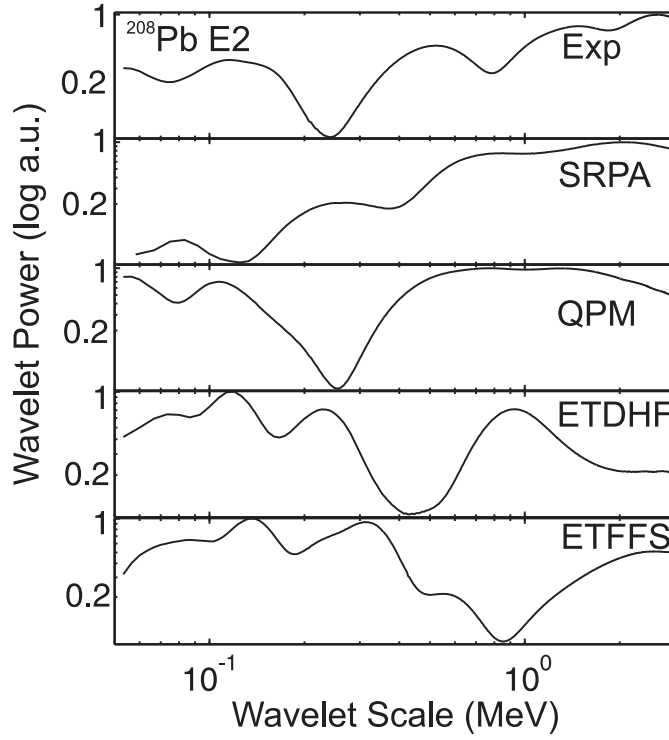


Fig. 8.3: Wavelet power spectra of the GQR in ^{208}Pb , from top to bottom: experiment, SRPA, QPM, ETDHF, ETFFS.

ents a novel approach providing a quantitative measure for the ability of different models to describe fine structure and characteristic scales. Table 8.1 summarizes

Tab. 8.1: Summary of the scales in ^{208}Pb observed experimentally compared to the different microscopic models that take into account coupling of $1p - 1h$ to $2p - 2h$ configurations.

| Class of Scales | I | II | III |
|------------------|--------|---------|-----------|
| Experiment (keV) | 110 | 500 | 1500 2600 |
| Theories | | | |
| SRPA | 80 | 250 800 | 2100 |
| QPM | 110 | 770 | 1400 |
| ETDHF | 70 120 | 230 930 | |
| ETFFS | 80 130 | 310 570 | 2500 |

the values of characteristic scales observed in the fine structure of ^{208}Pb in the region of GQR, as compared to those given by the microscopic model calculations that include $2p - 2h$ configurations. The global analysis of available data shows the presence of three groups of scales, classified according to their values. To the first group belong the scales with the values around and below 100 keV, which were detected in all the nuclei studied. The second group contains intermediate scales in the range of 100 keV to 1 MeV. These scales show large variations depending on the nuclear structure of the nucleus. The largest scales above 1 MeV are classified to the third group, describing the global structure of the resonance (the width). Considering the largest scales, characterizing the width of the resonance, the closest values are given by the SRPA and ETFFS predictions. As for the other scales, of all the microscopic models the results of the QPM are the best in reproducing the experimental observation.

Figures 8.4-8.6 represent similar comparisons of scales in ^{120}Sn , ^{90}Zr , and ^{58}Zr , extracted from available microscopic calculations. In order to verify the relevance of obtained scales and their importance, the discrete wavelet analysis is used. As an example, the comparison between the DWT analysis and the CWT results is made in Fig. 8.7 for the predictions of the GQR strength within the ETDHF and ETFFS models. A consistency of the two techniques is demonstrated. This allows a direct comparison of the ranges of scales given by the DWT to be made, as shown in Fig. 8.8. It is found that all models predict different ranges for scales to be important for the damping of the GQR in ^{208}Pb nucleus.

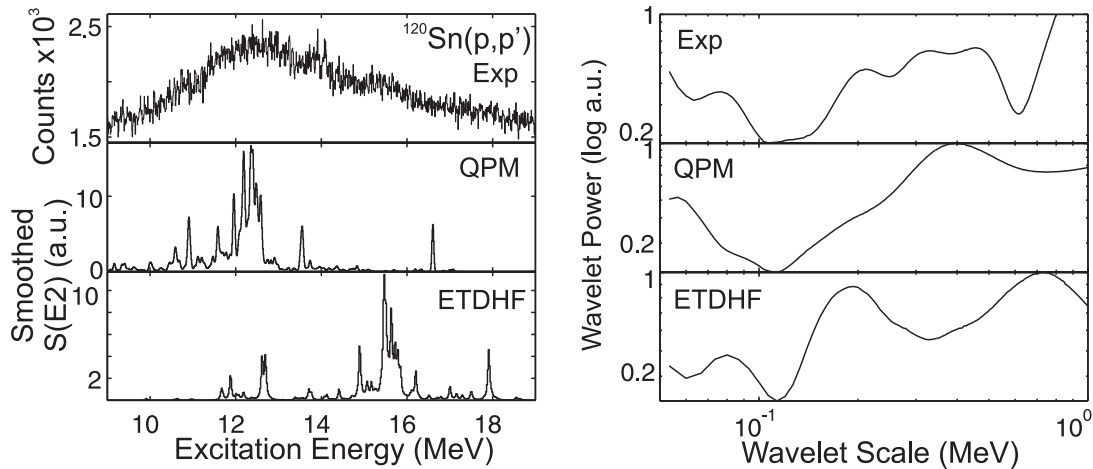


Fig. 8.4: Left: Spectrum of $^{120}\text{Sn}(p,p')$ reaction at $\Theta = 8^\circ$ vs. QPM and ETDHF predictions for the ISGQR. Right: corresponding wavelet power spectra.

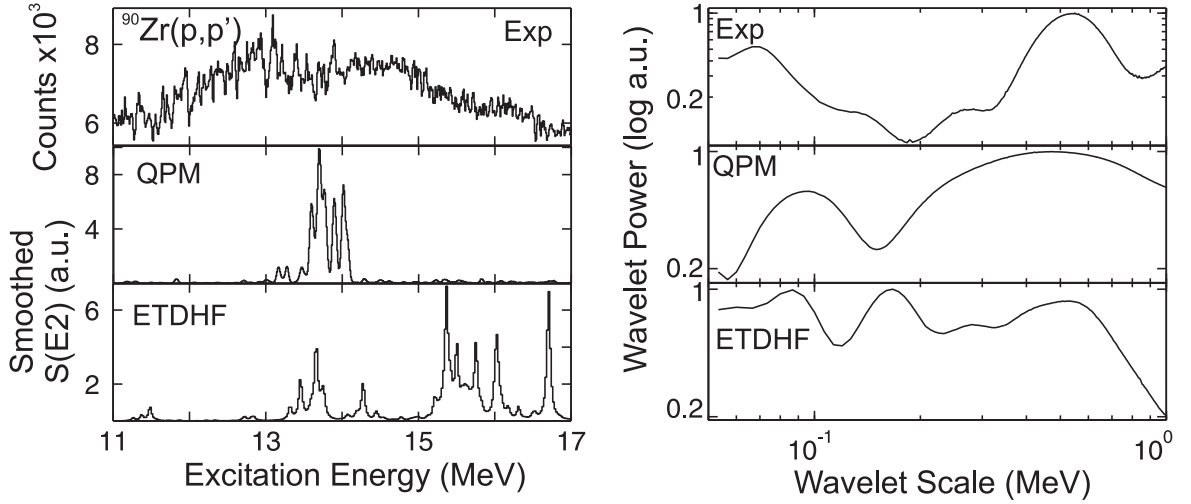


Fig. 8.5: Same as Fig. 8.4 for the ISGQR in ^{90}Zr .

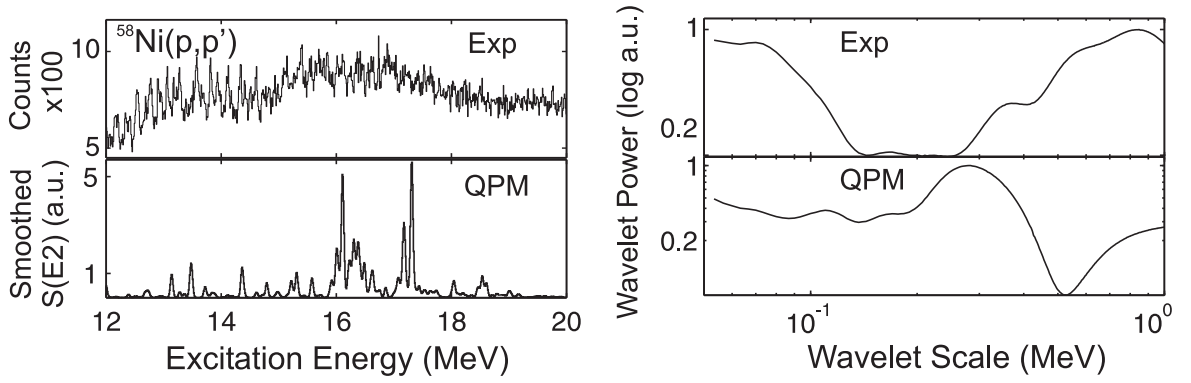


Fig. 8.6: Left: Spectrum of $^{58}\text{Ni}(p,p')$ reaction at $\Theta = 10^\circ$ vs. QPM prediction for the ISGQR. Right: corresponding wavelet power spectra.

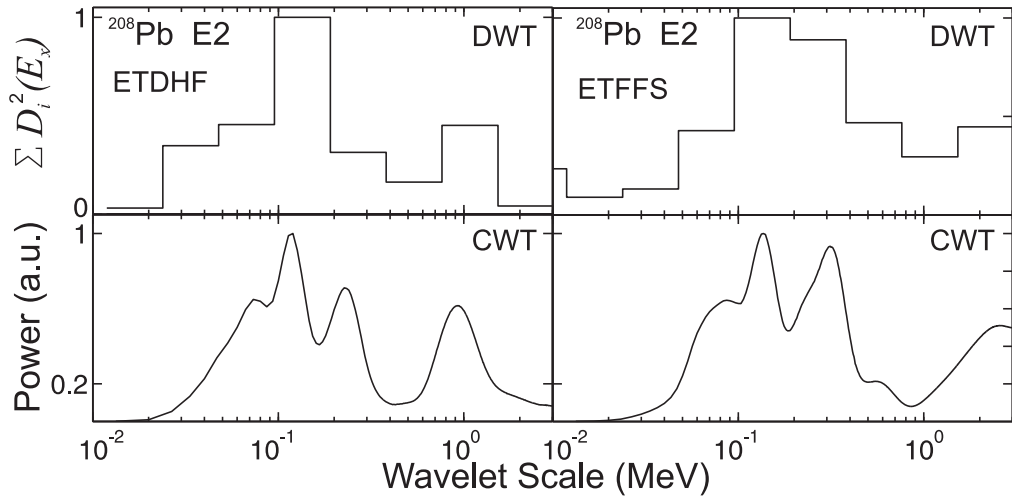


Fig. 8.7: Sum of squared details from the DWT (top) vs. the CWT power (bottom) for ETDHF (left) and ETFFS (right) models, of the GQR in ^{208}Pb .

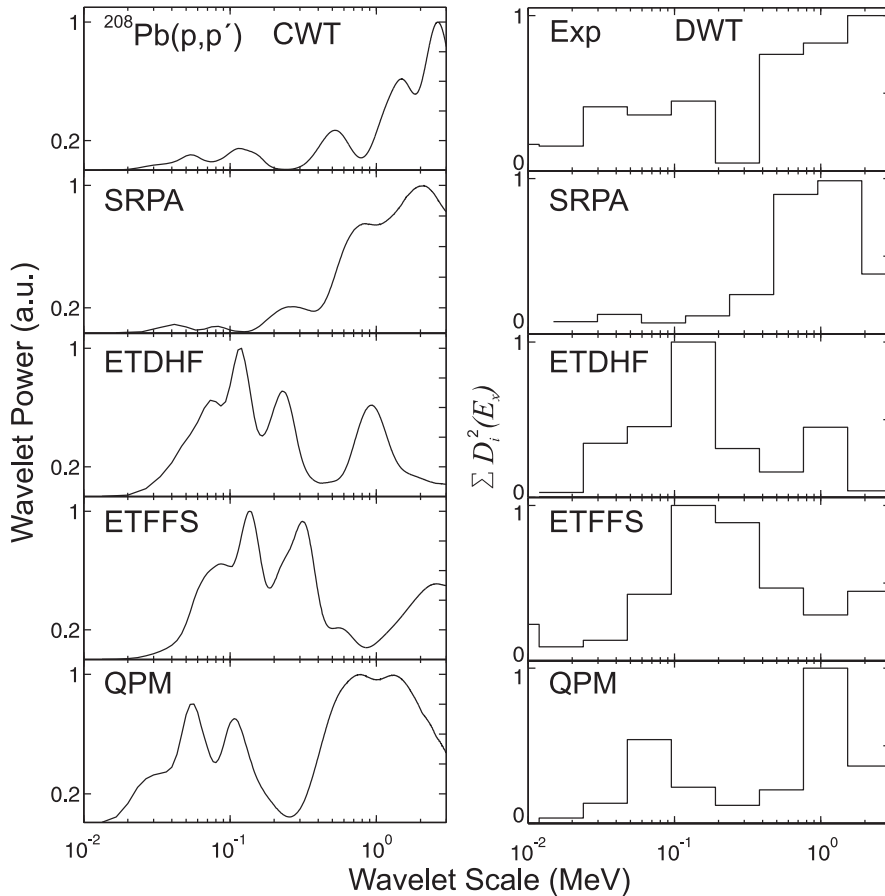


Fig. 8.8: The CWT power spectra (right) and the DWT decomposition results (left) for available microscopic models of the GQR in ^{208}Pb .

Summarizing this subsection, significant differences are observed on the scales from different models. The possible reasons are different techniques for model-space truncation, different interactions used in the models, and in the case of ETFFS the coupling to the continuum.

8.3 Collective vs. Non-Collective Damping

While the quantitative results of different models differ considerably, the success in reproducing at least the qualitative features of the characteristic scales motivates attempts to extract their underlying physical nature from the model predictions. In the framework of the QPM, which is very successful in describing many different collective modes, one is able to make a decomposition of the full model space into subspaces approximately corresponding to different damping

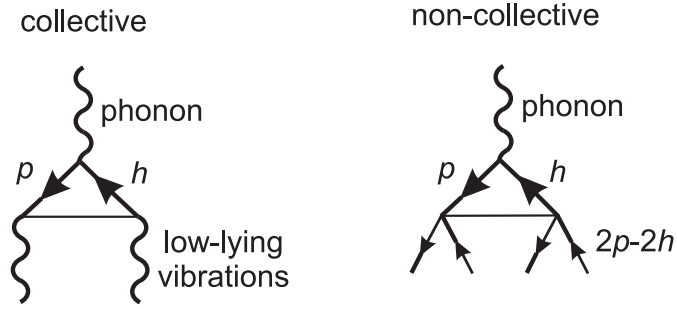


Fig. 8.9: *Collective* vs. *non-collective* damping mechanisms. The term *collective* corresponds to coupling to low-lying surface vibrations. The *non-collective* contribution results from the mixing of initial $1p - 1h$ states with the large background of states with more complex wave functions.

mechanisms. One such important mechanism contributing to the damping of the single-particle as well as the collective response in heavy nuclei is the coupling to low-lying surface vibrations, in the following called *collective*. Another significant contribution may come from mixing of the initial $1p - 1h$ states with the large background of states with more complex wave functions, called *non-collective*. These two mechanisms are depicted diagrammatically in Fig. 8.9.

The two contributions can be approximately disentangled within the QPM by considering the properties of the coupling matrix elements between the one- and two-phonon configurations. The probability $P\left(V_{1p-1h}^{2p-2h}\right)$ of finding a certain value of V_{1p-1h}^{2p-2h} is displayed as a histogram in Fig. 8.10 for the case of ^{208}Pb . The distribution deviates significantly from the Gaussian form (dot-dashed line in Fig. 8.10) expected for chaotic systems: one finds a strong overshoot of very small matrix elements and some enhancement at large values. Very similar features have been reported from the analysis of off-diagonal interaction matrix elements in shell-model calculations. The excess of small matrix elements indicates that many two-phonon configurations contribute little to the fragmentation process. On the other hand, the large matrix elements have an appreciable effect and are due to the presence of soft collective modes.

For separating the *collective* and *non-collective* mechanisms as prescribed above, the two-phonon configurations are divided into two subspaces: (i) – a large subspace with matrix elements following the Gaussian distribution (plus overshoot of the small matrix elements), and (ii) – a small subspace with large matrix elements values above the Gaussian tails.

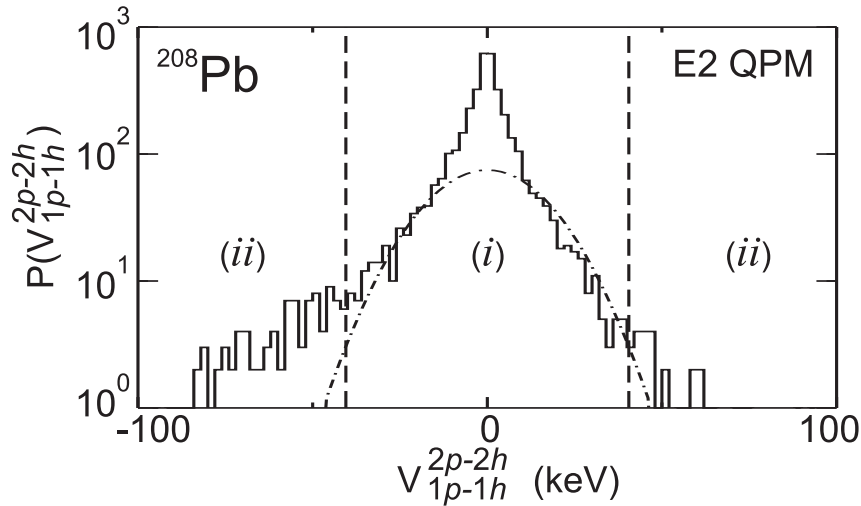


Fig. 8.10: Distribution of coupling matrix elements of $1p-1h$ states to the background states of more complex configurations in the full QPM calculation for the E2 response in ^{208}Pb . Dot-dashed line shows a Gaussian distribution, which follows from the Gaussian orthogonal ensemble (GOE) statistics as predicted by the Random Matrix Theory [100] for fully chaotic systems, the value for the Gaussian width is adopted to the data. One can see a large overshoot in the number of small matrix elements and the wings of the distribution, which carry the most collectivity of the excitations and are responsible for the *collective* damping.

The QPM Hamiltonian was then diagonalized in the 2-phonon subspaces composed from the $1\text{-phonon}\oplus(i)$ and alternatively from the $1\text{-phonon}\oplus(ii)$ subspaces. The resulting E2 strength functions are displayed in the left frame of Fig. 8.11. It is obvious that the fragmentation is dominated by the *collective* mechanism. One should also keep in mind that the full calculation is not just the sum of the two contributions, and interference terms may play a role. The corresponding wavelet power spectra are displayed in the right frame of Fig. 8.11. The decomposition makes clear that all scales in the calculation are already present in the *collective* part. These findings are also confirmed by a comparable analysis within the ETDHF model, shown in Fig. 8.12. This model also allows based on a perturbation approach to separate the contributions from the *collective* and the *non-collective* damping mechanisms. The absence of pronounced scales in the *non-collective* part suggests a generic origin, i.e. a stochastic coupling to a 'background' of complex states. The level spacings and coupling matrix element distributions are then described by the Gaussian orthogonal ensemble (GOE).

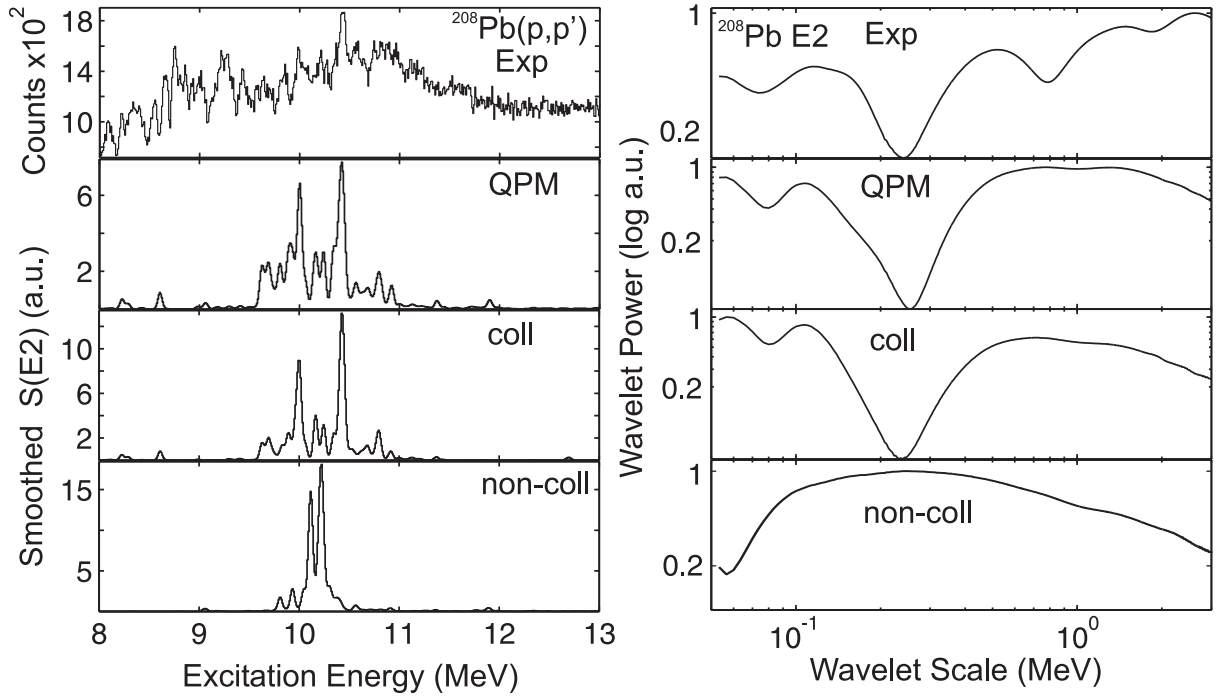


Fig. 8.11: Left-hand side: Experimental spectrum of the ISGQR in ^{208}Pb as compared to the QPM prediction and its decomposition to the *collective* and *non-collective* damping contributions. Right-hand side: the corresponding wavelet power spectra.

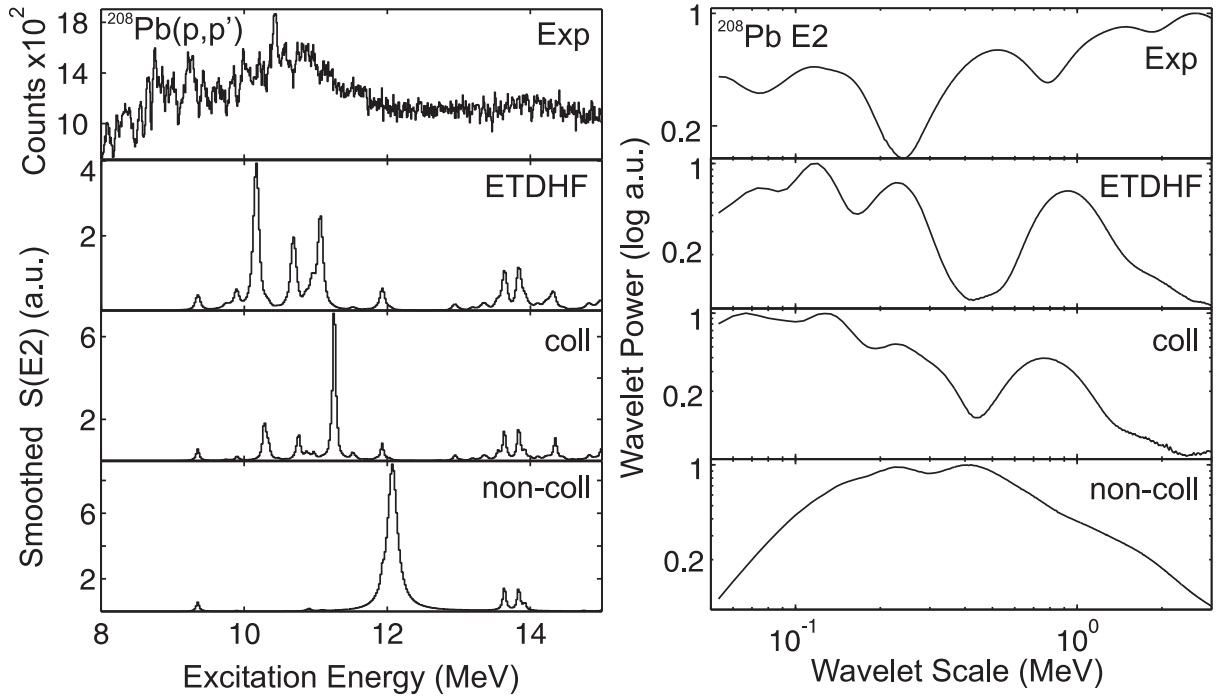


Fig. 8.12: Same as Fig. 8.11 for the ETDHF model predictions.

Figures 8.13 and 8.14 present a similar disentanglement for the case of ^{120}Sn and provide the same picture. The results for ^{208}Pb and ^{120}Sn show that all the scales observed in the full QPM prediction are already reproduced by including only *collective* damping. The conclusion can be drawn that in heavy nuclei what is called *collective damping* is responsible for all the scales. In the *non-collective* part of ^{208}Pb and ^{120}Sn , a broad distribution of wavelet power is observed.

Conversely, the decomposition into a *collective* and a *non-collective* part in medium-heavy nuclei ^{90}Zr and ^{58}Ni (see Figs. 8.15 – 8.17) shows an increased role of the *non-collective* damping. The role of *collective* and *non-collective* mechanisms changes dramatically as one moves towards lighter nuclei. The structure in the lighter nuclei is still not so well described. The *non-collective* damping mechanism is becoming more non-generic as one goes to lighter systems. The results of the ETDHF model qualitatively confirm the findings from the QPM model. However, the perturbative approach of the ETDHF leads to large shifts in the strength distributions, which might indicate strong interference effects of the two damping mechanisms, intrinsic within the model. This makes the results more difficult to interpret, as compared to the QPM calculations.

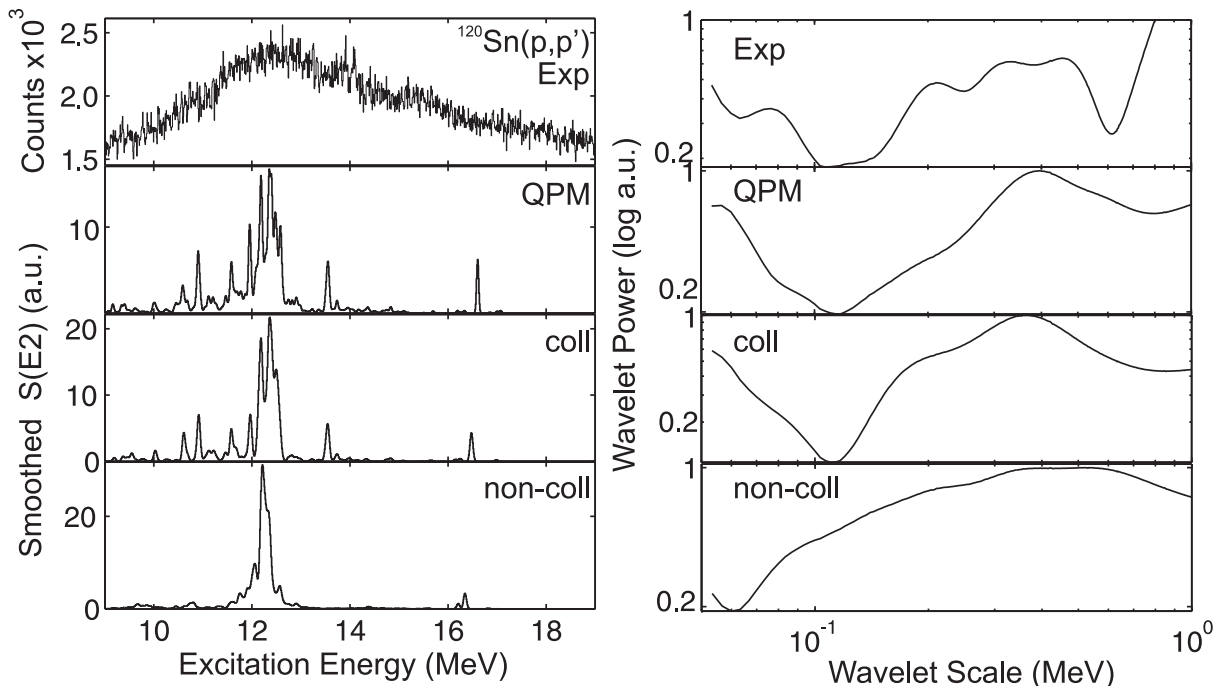


Fig. 8.13: Left-hand side: Experimental spectrum of the ISGQR in ^{120}Sn at $\Theta = 8^\circ$ as compared to the QPM result and its decomposition to the *collective* and *non-collective* parts. Right-hand side: the wavelet power spectra.

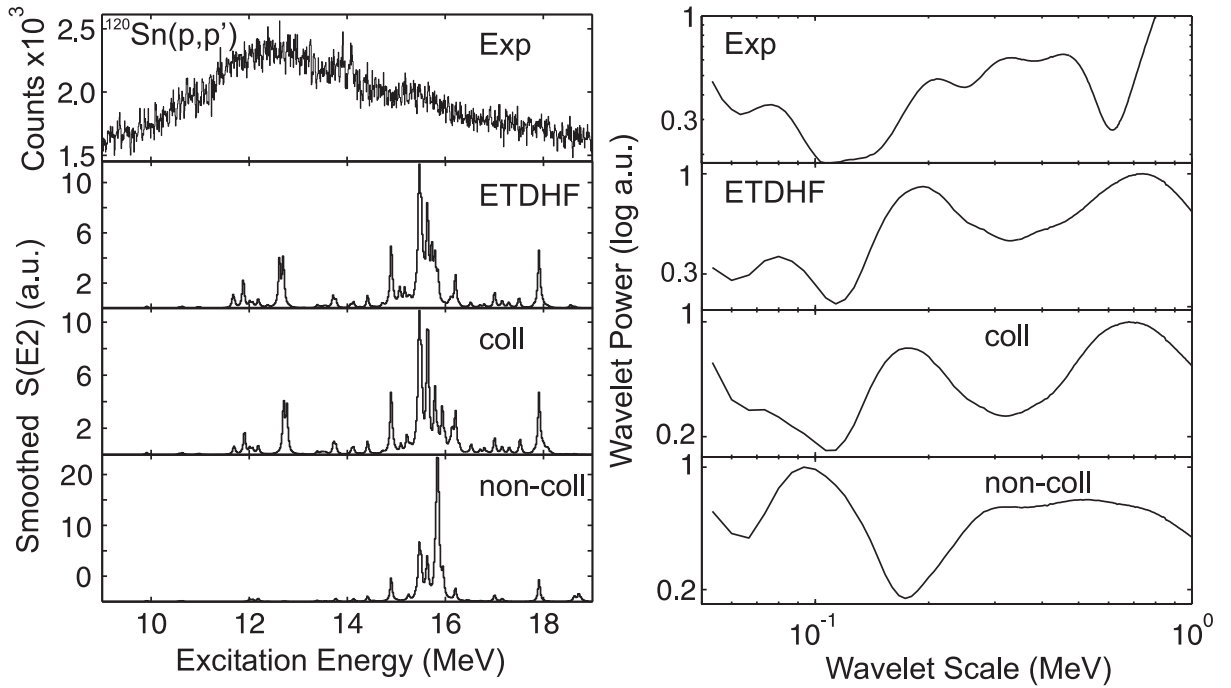


Fig. 8.14: Left-hand side: Experimental spectrum of $^{120}\text{Sn}(p,p')$ at $\Theta = 8^\circ$ as compared to the ETDHF result and its decomposition to the *collective* and *non-collective* parts. Right-hand side: the wavelet power spectra.

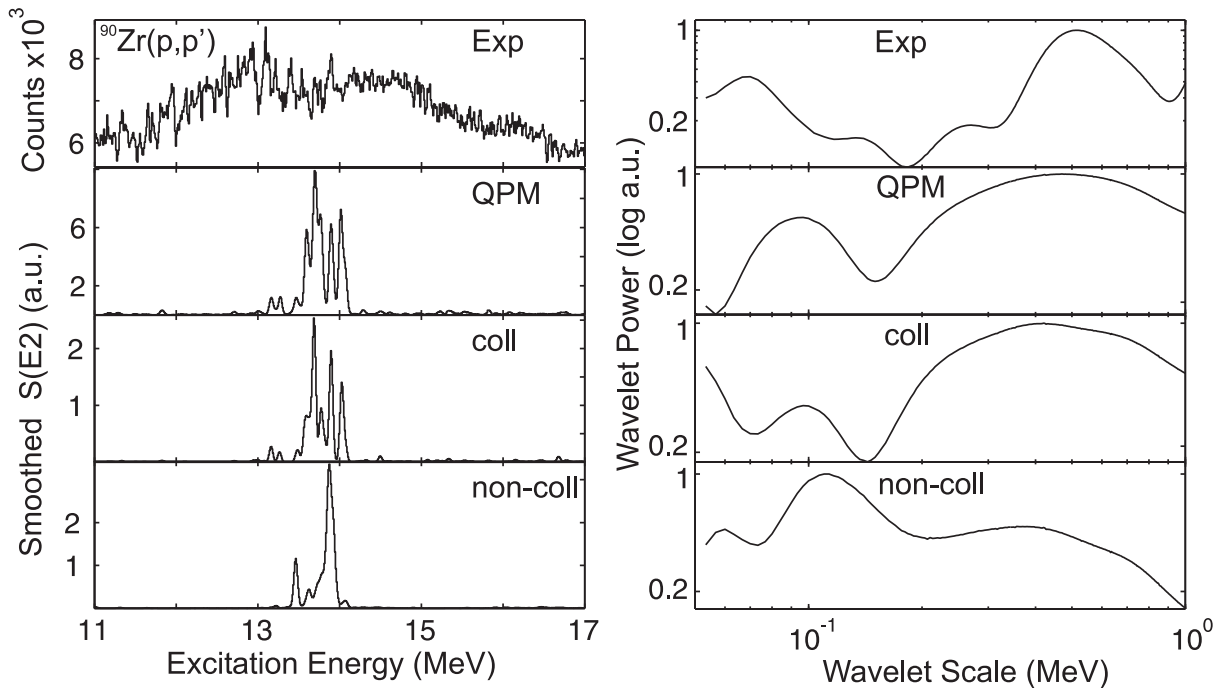


Fig. 8.15: Left-hand side: Spectrum of $^{90}\text{Zr}(p,p')$ at $\Theta = 9.2^\circ$ as compared to the QPM result and its decomposition to the *collective* and *non-collective* parts. Right-hand side: the wavelet power spectra.

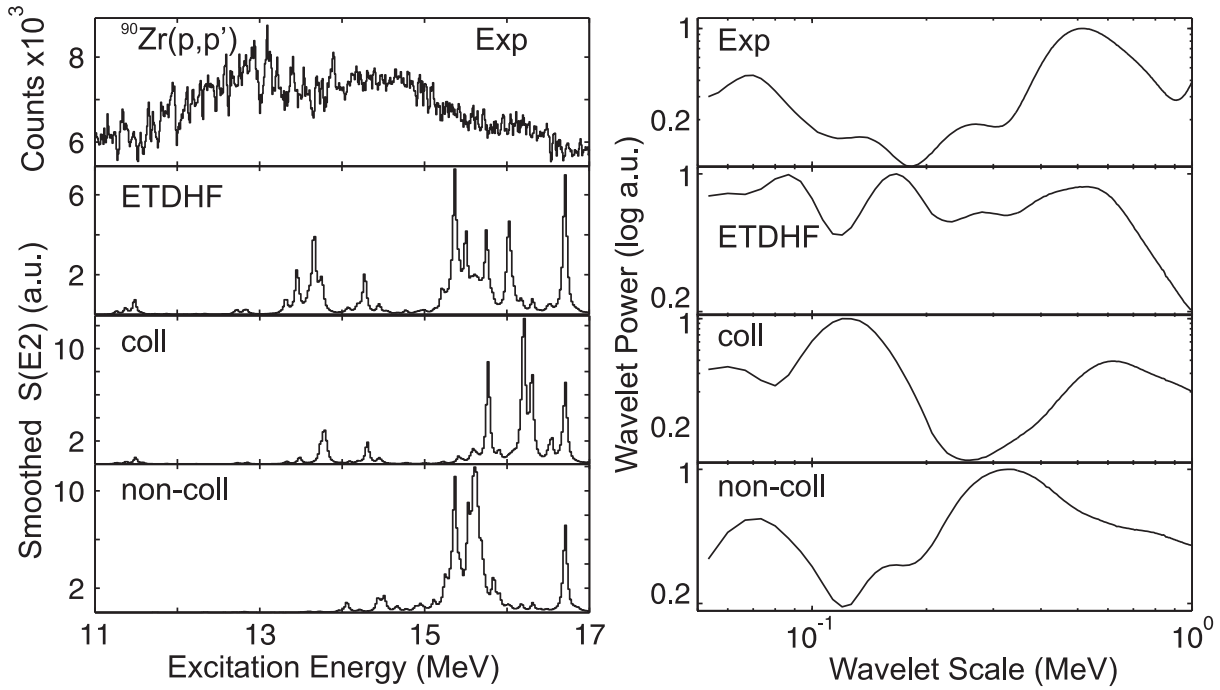


Fig. 8.16: Left-hand side: Spectrum of $^{90}\text{Zr}(p,p')$ at $\Theta = 9.2^\circ$ as compared to the ETDHF result and its decomposition to the *collective* and *non-collective* parts. Right-hand side: the wavelet power spectra.

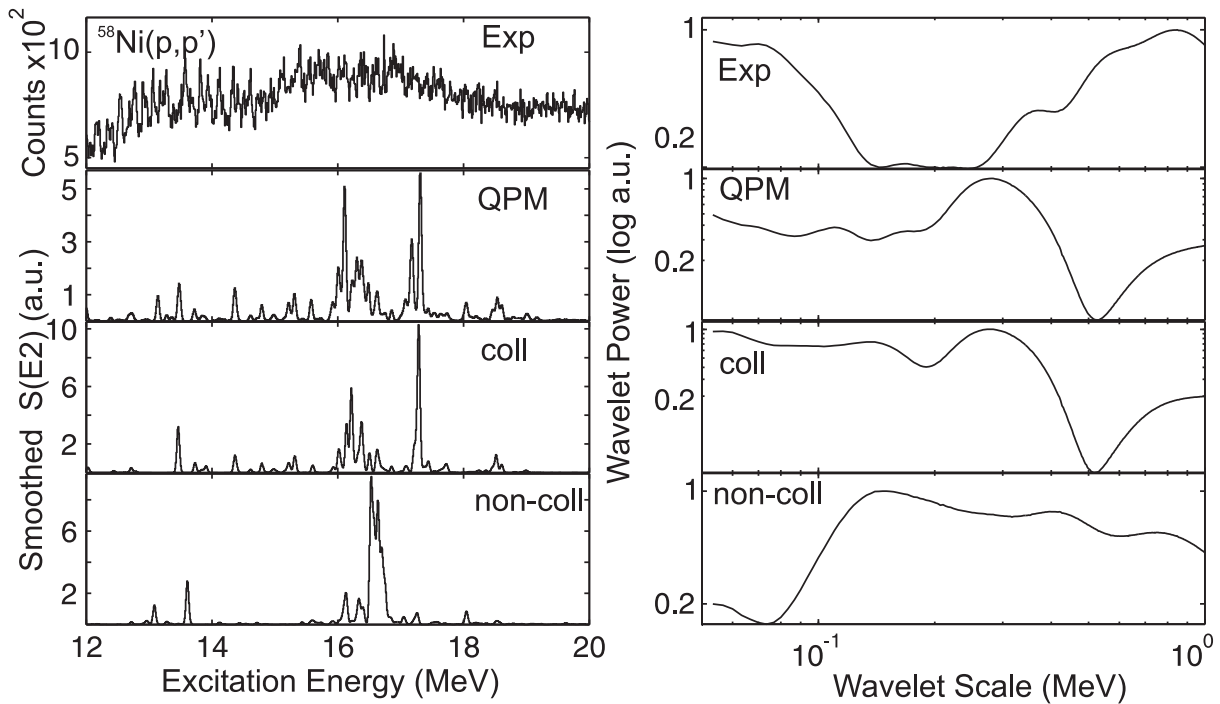


Fig. 8.17: Left-hand side: Spectrum of $^{58}\text{Ni}(p,p')$ at $\Theta = 10^\circ$, compared to the QPM result and its decomposition to the *collective* and *non-collective* parts. Right-hand side: the wavelet power spectra.

8.4 Nature of the Non-Collective Damping

For a better understanding of the wavelet analysis results, it is worthwhile to consider a qualitative model for the *non-collective* coupling. First, a discussion of a simple, schematic approach, the so-called *picket-fence* model is given. In the next step we proceed to a more realistic picture allowing for stochastic coupling.

8.4.1 Picket-Fence Model

Within the picket-fence model one considers the case of a single doorway state, which can couple to many equidistantly spaced background states. The left panel of Fig. 8.18 shows the response function, and the right panel the resulting wavelet power distribution using a Morlet wavelet function. The two upper plots correspond to the case when coupling matrix elements are all equal. In this case one obtains a strength function, which has a well-known Breit-Wigner shape

$$S(E) = \frac{1}{2\pi} \frac{\Gamma}{(E - E_0)^2 + \Gamma^2/4} . \quad (8.1)$$

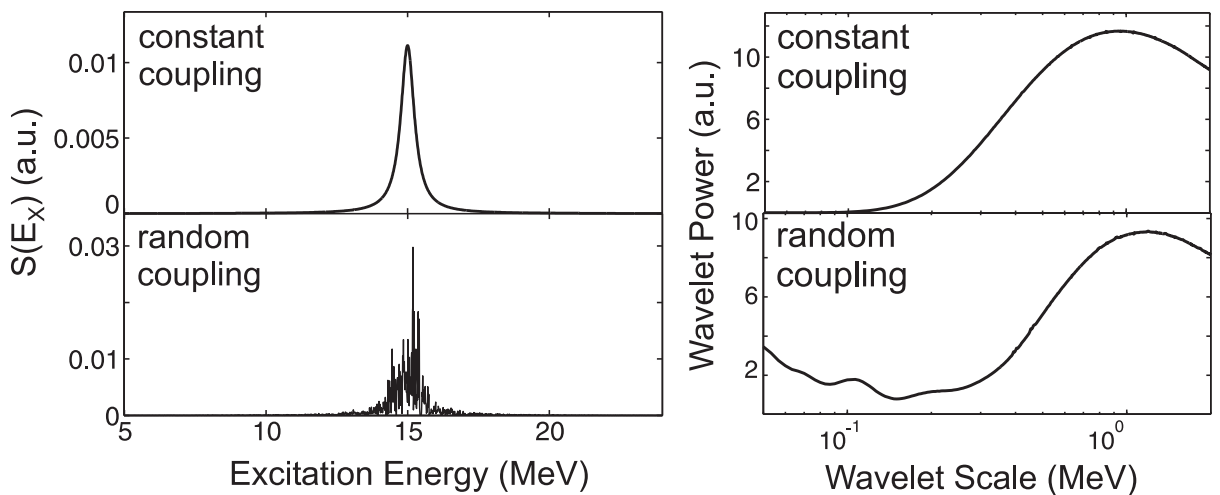


Fig. 8.18: Picket-fence model for one doorway state, coupled to many equidistantly spaced background states. Left panel: the response function. Right panel: the wavelet power distribution. Two cases: a) constant coupling matrix element V_{coupl} (upper plots) - A Breit-Wigner shape for the response is reproduced. The wavelet analysis detects the presence of one scale which corresponds to the width of the distribution. b) Random coupling matrix elements with uniform distribution (lower plots).

The wavelet power distribution shows, as expected, the appearance of only one scale, which corresponds to the width Γ of that distribution. The *Fermi's golden rule* relates then the width Γ to the squared coupling matrix element $|V|^2$ and the density of the background states ρ via the expression

$$\Gamma = 2\pi |V|^2 \rho . \quad (8.2)$$

The two other plots at the bottom of Fig. 8.18 show the results for the case where coupling matrix elements are generated randomly with a uniform distribution. The global behavior of the response function remains, additional structures caused by a chaotic component appearing on top of it. The wavelet analysis shows the same large scale, resulting from the width, together with an increased intensity at smaller scales. For each realization of the ensemble of random matrix elements, a unique wavelet power distribution will appear, reflecting the chaotic origin of coupling matrix elements.

Although the example given is very simplified and practically never realized in real nuclei, one can see how well the wavelet transform performs when applied to the problem of doorway coupling. In the following a more realistic model case is considered.

8.4.2 Stochastic Coupling Model

In both previous examples of the picket-fence model the background states were placed at equidistant spacing. A more realistic case is realized by generating the level spacings D between the background states randomly according to a Wigner distribution [101]

$$P_{Wigner}(D) = \frac{\pi}{2} \frac{D}{\langle D \rangle} \exp\left(-\frac{\pi}{4} \frac{D^2}{\langle D \rangle^2}\right) \quad (8.3)$$

for a given average level spacing $\langle D \rangle$. This distribution shows the so-called “level repulsion”, i.e. an absence of small distances, which is characteristic for fully chaotic systems. The values of coupling matrix elements are randomly generated using not a uniform but rather a Gaussian distribution, having a width corresponding to that from the full QPM calculation for ^{208}Pb (see Fig. 8.10). The strength function generated in such a *stochastic coupling* model is in agreement

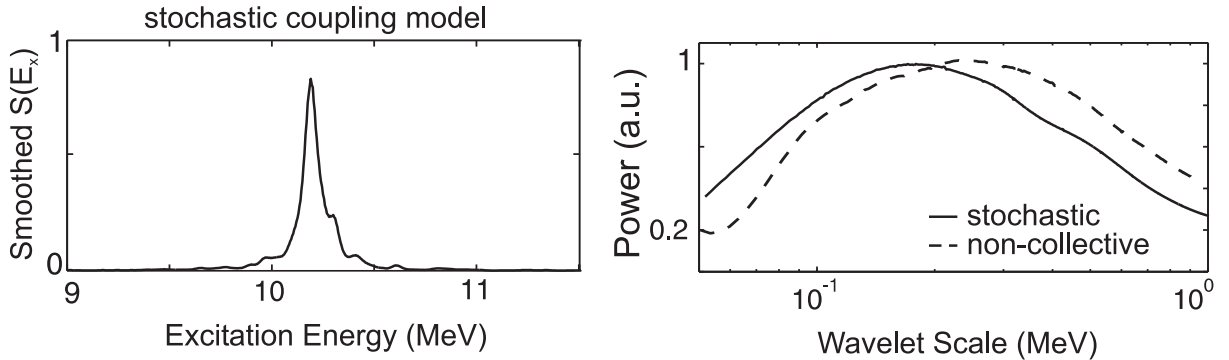


Fig. 8.19: Stochastic coupling model. Left-hand side: the strength function. Right-hand side: the wavelet power averaged over an ensemble of many random realizations. Dashed line: the wavelet power for the case of *non-collective* damping within the QPM for ^{208}Pb nucleus.

with the predictions of the Random Matrix Theory (RMT) for fully chaotic systems. The results of the wavelet analysis for this model are shown in Fig. 8.19. The left panel gives the form of the response function for one random realization for the coupling matrix elements and the positions of the background states.

In order to detect a generic feature that would not depend on any random realization a statistical ensemble of many such response functions has been generated. For each realization the CWT using Morlet wavelet function was calculated. The average wavelet power distribution was then extracted for the whole ensemble and is shown in the right panel of Fig. 8.19. One can see a rather featureless distribution of scales, having a flat maximum at several hundreds of keV. A rather good correspondence is observed with the wavelet power that was obtained for the *non-collective* component of the QPM calculation in ^{208}Pb (dashed line in Fig. 8.19). This finding serves as a strong indication that the *non-collective* damping is indeed a generic mechanism, coming from the stochastic coupling with the background complex configurations, and leading to the appearance of rather broad range of scales in the nuclear response with a maximum at scale values of several hundred keV.

9 Summary and Outlook

The present thesis has been devoted to the investigation of the phenomenon of fine structure of giant resonances in heavy and medium-heavy nuclei. Emphasis was placed on the extraction of the properties of the ISGQR. High-resolution inelastic proton scattering data were collected at the iThemba LABS cyclotron facility utilizing an $E_p = 200$ MeV proton beam and the K600 magnetic spectrometer for ^{58}Ni , ^{89}Y , ^{90}Zr , ^{120}Sn , ^{142}Nd , ^{166}Er , and ^{208}Pb target nuclei for kinematical conditions corresponding to the maximum of a $\Delta L = 2$ excitation. For some selected cases, angular distributions were measured above and below the maximum of the $\Delta L = 2$ angular distributions in order to estimate the effects of different multipoles contributing to the cross sections. An energy resolution of 35 to 50 keV FWHM was achieved using dispersion matching techniques, which were mandatory for the detection of the fine structure in the excitation energy spectra. Fine structure was identified in all the investigated nuclei, thereby proving it to be a global feature, at least for medium-heavy and heavy nuclei. Recent work [102] also confirms the appearance of fine structure in a spin-isospin mode (Gamow-Teller resonance). Furthermore, high-resolution (e,e') data suggest its existence in E1 (GDR) and M2 modes [35, 103].

Several methods have been applied for the characterization of fine structure and the extraction of energy scales. New techniques based on a wavelet transform were developed and utilized, which give the precise and model-independent information on the scales and their localization in the excitation energy spectrum. These features of the wavelet analysis allowed to confirm that the experimentally identified scales are indeed characteristic for the ISGQR energy region.

For the interpretation of these data, a variety of microscopic models has been used. By comparison to RPA and more sophisticated microscopic calculations, which are in good agreement with the experiment, it could be shown that the fine structure and the characteristic scales of it are related to the coupling of $1p - 1h$ to $2p - 2h$ states. This probably represents the clearest experimental confirmation so far of the doorway picture of giant resonances.

In order to reveal the physical nature of the observed scales, a detailed comparison to QPM predictions was made, in which different damping mechanisms could be

disentangled. The collective damping, i.e. the coupling of $1p-1h$ states to surface vibrations, was found to be responsible for all the scales, proving the commonly accepted hypothesis that the collective mechanism is dominant in the damping. On the contrary, the non-collective damping, which is due to the coupling to the background of many more complex states, gave no pronounced scales, but a rather broad distribution of wavelet power. Further comparison with several model cases lead to the conclusion of a generic nature for non-collective damping, which actually comes from a stochastic coupling in which many randomly distributed small matrix elements contribute incoherently to the damping process.

In future experimental studies an improved energy resolution must be achieved in order to uncover the next levels in the hierarchy of couplings, which are expected to produce even finer structure and smaller scales. Possible approaches are the decay study of giant resonances using high-resolution detector arrays EUROBALL [104] and GAMMASPHERE [105].

It would be also of interest to study the transition from spherical to deformed nuclei (e.g., on the basis of the neodymium isotope chain $^{142,144,146,148}\text{Nd}$). Presently, reliable theoretical microscopic predictions for deformed nuclei are still lacking. Inclusion of two-phonon configurations has been achieved within the QPM using a Nilsson model basis, however, applications have been restricted to the low-energy collective modes only [96], like octupole vibrations or the orbital M1 scissors mode.

These studies would allow one to go a step further in understanding the transition from order to chaos in fermionic quantum systems like the atomic nucleus.

References

- [1] A. van der Woude, in: J. Speth (Ed.), *Electric and Magnetic Giant Resonances in Nuclei* (World Scientific, Singapore, New Jersey, London, Hong Kong, 1991), p. 160.
- [2] M.N. Harakeh and A. van der Woude, *Giant Resonances: Fundamental High-Frequency Modes of Nuclear Excitation* (Oxford University Press, Oxford, 2001).
- [3] W. Bothe and W. Gentner, *Z. Phys.* **106** (1937) 236.
- [4] G.C. Baldwin and G.S. Klaiber, *Phys. Rev.* **71** (1947) 3.
- [5] M. Goldhaber and E. Teller, *Phys. Rev.* **74** (1948) 1046.
- [6] R. Pitthan and Th. Walcher, *Phys. Lett.* **36B** (1971) 563.
- [7] M.B. Lewis, *Phys. Rev. Lett.* **29** (1972) 1257.
- [8] M.B. Lewis and F.E. Bertrand, *Nucl. Phys. A* **196** (1972) 337.
- [9] S. Fukuda and Y. Torizuka, *Phys. Rev. Lett.* **29** (1972) 1109.
- [10] D.H. Youngblood, P. Bogucki, J.D. Bronson, U. Garg, Y.-W. Lui, and C.M. Rozsa, *Phys. Rev. C* **23** (1981) 1997.
- [11] F. Zwarts, A. G. Drentje, M. N. Harakeh and A. van der Woude, *Nucl. Phys. A* **439** (1985) 117.
- [12] M. Buenerd, K. Bouhela, Ph. Martin, J. Chauvin, D. Lebrun, G. Perrin, P. de Saintignon, and G. Duhamel, *Phys. Rev. C* **38** (1988) 2514.
- [13] M.M. Sharma, W. T.A. Borghols, S. Brandenburg, S. Crona, A. van der Woude, and M.N. Harakeh, *Phys. Rev. C* **38** (1988) 2562.
- [14] G. Duhamel, M. Buenerd, P. de Saintignon, J. Chauvin, D. Lebrun, Ph. Martin, and G. Perrin, *Phys. Rev. C* **38** (1988) 2509.

- [15] W. T. A. Borghols, S. Brandenburg, J. H. Meier, J. M. Schippers, M. M. Sharma, A. van der Woude, M. N. Harakeh, A. Lindholm, L. Nilsson, S. Crona, A. Håkansson, L. P. Ekström, N. Olsson and R. de Leo, *Nucl. Phys. A* **504** (1989) 231.
- [16] J. Lisantti, D.J. Horen, F.E. Bertrand, R.L. Auble, B.L. Burks, E.E. Gross, R.O. Sayer, D.K. McDaniels, K.W. Jones, J.B. McClelland, S.J. Seestrom-Morris, and L.W. Swenson, *Phys. Rev. C* **40** (1989) 211.
- [17] G.R. Satchler and D.T. Khoa, *Phys. Rev. C* **55** (1997) 285.
- [18] K. Schweda, J. Carter, A.A. Cowley, H. Diesener, R.W. Fearick, S.V. Förtsch, J.J. Lawrie, P. von Neumann-Cosel, J.V. Pilcher, A. Richter, F.D. Smit, G.F. Steyn and S. Strauch, *Phys. Lett. B* **506** (2001) 247.
- [19] J. Speth (Ed.), *Electric and Magnetic Giant Resonances in Nuclei* (World Scientific, Singapore, 1991).
- [20] P.F. Bortignon, A. Bracco, and R.A. Broglia, *Giant Resonances: Nuclear Structure at Finite Temperature* (Harwood Academic, Amsterdam, 1998).
- [21] *Topical Conference on Giant Resonances 1998, Varenna, Italy*, *Nucl. Phys. A* **649** (1999).
- [22] *International Conference on Giant Resonances 2000, Osaka, Japan*, *Nucl. Phys. A* **687** (2001).
- [23] G. Kühner, D. Meuer, S. Müller, A. Richter, E. Spamer, O. Titze and W. Knüpfner, *Phys. Lett. B* **104** (1981) 189.
- [24] H. Aiba, S. Mizutori, and T. Suzuki, *Phys. Rev. E* **56** (1997) 119.
- [25] H. Aiba and M. Matsuo, *Phys. Rev. C* **60** (1999) 034307.
- [26] H. Aiba, M. Matsuo, S. Nishizaki, and T. Suzuki, *Phys. Rev. C* **68** (2003) 054316.
- [27] D. Lacroix, A. Mai, P. von Neumann-Cosel, A. Richter and J. Wambach, *Phys. Lett. B* **479** (2000) 15.
- [28] D.J. Rowe, *Nuclear Collective Motion* (Methuen, London, 1970).

- [29] P. Ring and P. Schuck, *The Nuclear Many-Body Problem* (Springer-Verlag, Berlin, 1980).
- [30] B. Block and H. Feshbach, *Ann. Phys. (N.Y.)* **23** (1963) 47.
- [31] H. Feshbach, *Rev. Mod. Phys.* **36** (1964) 1076.
- [32] H. Feshbach, *Rev. Mod. Phys.* **46** (1974) 1.
- [33] G. Herbert, Dissertation D17, TH Darmstadt (1994).
- [34] H. Diesener, Dissertation D17, TH Darmstadt (1995).
- [35] S. Strauch, Dissertation D17, TU Darmstadt (1998).
- [36] K. Schweda, Dissertation D17, TU Darmstadt (2000).
- [37] W. Cassing and U. Mosel, *Prog. Part. Nucl. Phys.* **25** (1990) 235.
- [38] P.-G. Reinhard and C. Toepffer, *Int. J. Mod. Phys. E.* **3** (1994) 435.
- [39] Y. Abe, S. Ayik, P.-G. Reinhard, and E. Suraud, *Phys. Rep.* **275** (1996) 49.
- [40] T. Ericson, *Ann. Phys. (N.Y.)* **23** (1963) 390.
- [41] T. Ericson, *Phys. Rev. Lett.* **5** (1960) 430.
- [42] A. Schwierczinski, R. Frey, A. Richter, E. Spamer, H. Thiessen, O. Titze, T. Walcher, S. Krewald, and R. Rosenfeld, *Phys. Rev. Lett.* **35** (1975) 1255.
- [43] S. Kamerdzhiev, J. Lisantti, P. von Neumann-Cosel, A. Richter, G. Tertychny, and J. Wambach, *Phys. Rev. C* **55** (1997) 2101.
- [44] J. Winchenbach, K. Pingel, G. Holzwarth, G. Kühner and A. Richter, *Nucl. Phys. A* **410** (1983) 237.
- [45] G. Kilgus, G. Kühner, S. Müller, A. Richter, and W. Knüpfner, *Z. Phys. A* **326** (1987) 41.
- [46] D. Lacroix and P. Chomaz, *Phys. Rev. C* **60** (1999) 064307.

- [47] P. von Neumann-Cosel, F. Neumeyer, S. Nishizaki, V.Yu. Ponomarev, C. Rangacharyulu, A. Richter, G. Schrieder, D.I. Sober, T. Waindzoeh, and J. Wambach, *Phys. Rev. Lett.* **82** (1999) 1105.
- [48] R.T. Newman, Ph.D. thesis, University of Cape Town (1996).
- [49] G.F. Steyn, S.V. Förtsch, A.A. Cowley, S. Karataglidis, R. Lindsay, J.J. Lawrie, F.D. Smit, and R.T. Newman, *Phys. Rev. C* **57** (1998) 1817.
- [50] J. Carter, A.A. Cowley, H. Diesener, R.W. Fearick, S.V. Förtsch, J.J. Lawrie, P. von Neumann-Cosel, J.V. Pilcher, A. Richter, K. Schweda, F.D. Smit, G.F. Steyn, and S. Strauch, *Phys. Rev. C* **63** (2001) 057602.
- [51] R. Neveling, Ph.D. thesis, University of Stellenbosch (2001).
- [52] H. Diesener, U. Helm, P. von Neumann-Cosel, A. Richter, G. Schrieder, A. Stascheck, A. Stiller and J. Carter, *Nucl. Phys. A* **696** (2001) 272.
- [53] H. Diesener, U. Helm, V. Huck, P. von Neumann-Cosel, C. Rangacharyulu, A. Richter, G. Schrieder, A. Stascheck, S. Strauch, J. Ryckebusch and J. Carter, *Nucl. Phys. A* **696** (2001) 293.
- [54] R. Neveling, A.A. Cowley, G.F. Steyn, S.V. Förtsch, G.C. Hillhouse, J. Manno, and S.M. Wyngaardt, *Phys. Rev. C* **66** (2002) 034602.
- [55] H.A. Enge, *Nucl. Instrum. Methods* **187** (1981) 1.
- [56] G. Hinderer, H. Lehr and K.H. Maier, *Nucl. Instrum. Methods* **160** (1979) 449.
- [57] C.C. Foster and G.P.A. Berg, IUCF Sci. and Tech. Report (1988-1989) 193.
- [58] Y. Fujita, K. Hatanaka, G.P.A. Berg, K. Hosono, N. Matsuoka, S. Morinobu, T. Noro, M. Sato, K. Tamura, and H. Ueno, *Phys. Res. B* **126** (1997) 274.
- [59] W. Bertozzi, M.V. Hynes, C.P. Sargent, C. Creswell, P.C. Dunn, A. Hirsch, M. Leitch, B. Norum, F.N. Rad and T. Sasanuma, *Nucl. Instrum. Methods* **141** (1977) 457.
- [60] TRANSPORT a computer program for designing charged particle beam transport systems, Technical report, CERN-80-04, Geneva 1980.

- [61] H. Fujita, Y. Fujita, G.P.A. Berg, A.D. Bacher, C.C. Foster, K. Hara, K. Hatanaka, T. Kawabata, T. Noro and H. Sakaguchi, Nucl. Instrum. Methods A **484** (2002) 17.
- [62] IUCF VME Data Acquisition System User Information, Technical report, Indiana University Cyclotron Facility, unpublished, 1994.
- [63] C.R. Gould, L.G. Holzweig, S.E. King, Y.C. Lau, R.V. Poore, N.R. Robertson, and S.A. Wender, IEEE trans. Nucl. Sci. **NS-28** (1981) 3708.
- [64] J.V. Pilcher, A.A. Cowley, D.M. Whittall, and J.J. Lawrie, Phys. Rev. C **40** (1989) 1937.
- [65] J. Lisantti, E.J. Stephenson, A.D. Bacher, P. Li, R. Sawafta, P. Schwandt, S.P. Wells, S.W. Wissink, W. Unkelbach, and J. Wambach, Phys. Rev. C **44** (1991) R1233.
- [66] F.E. Bertrand, E.E. Gross and D.J. Horen, J.R. Wu, J. Tinsley, D.K. McDaniels, L.W. Swenson and R. Liljestrand, Phys. Lett. **103B** (1981) 326.
- [67] H. Spangenberger, F. Beck and A. Richter, Nucl. Phys. A **448** (1986) 21.
- [68] P. Grassberger and I. Procaccia, Physica **9D** (1983) 189.
- [69] P. Grassberger and I. Procaccia, Phys. Rev. Lett. **50** (1983) 346.
- [70] P. Grassberger and I. Procaccia, Physical Review A **28** (1983) 2591.
- [71] F. Crow, Communications of the ACM **20(11)** (1977) 799.
- [72] J. Enders, T. Guhr, N. Huxel, P. von Neumann-Cosel, C. Rangacharyulu and A. Richter, Phys. Lett. B **486** (2000) 273.
- [73] R.C. Hwa, physics/9809041 .
- [74] N. Morrison, *Introduction to Fourier Analysis* (John Wiley and Sons, 1994).
- [75] P.S. Addison, *The Illustrated Wavelet Transform Handbook* (The Institute of Physics Publishing, Bristol, 2001).
- [76] G. Kaiser, *A Friendly Guide to Wavelets* (Boston, Birkhäuser, 1994).

- [77] H.L. Resnikoff and Jr. R.O. Wells, *Wavelet Analysis : The Scalable Structure of Information* (Springer-Verlag New York, 2002).
- [78] C. Torrence and G.P. Compo, *Bulletin of the American Meteorological Society* **79(1)** (1998) 61.
- [79] S. Mallat, *A Wavelet Tour of Signal Processing* (Academic Press, San Diego, 1998).
- [80] I. Daubechies, *IEEE Trans. Inform. Theory* **36** (1990) 961.
- [81] G. Erlebacher, M.Y. Hussaini, and L.M. Jameson (Eds.), *Wavelets: Theory and Applications* (Oxford University Press, New York, NY, USA, 1996).
- [82] D. Lagoutte, J.C. Cerisier, J.L. Plagnaud, J.P. Villian, and B. Forget, *J. Atm. Terr. Phys.* **54** (1992) 1283.
- [83] A. Richter, *Nucl. Phys. A* **731** (2004) 59.
- [84] P. von Neumann-Cosel, in: *Proceedings of the International Workshop XXII on Gross Properties of Nuclei and Nuclear Excitations, Hirschegg, Austria, January 11-17 2004* (GSI, Darmstadt, 2004).
- [85] A. Shevchenko, J. Carter, R.W. Fearick, S.V. Förtsch, H. Fujita, Y. Fujita, Y. Kalmykov, D. Lacroix, J.J. Lawrie, P. von Neumann-Cosel, R. Neveling, V.Yu. Ponomarev, A. Richter, E. Sideras-Haddad, F.D. Smit, and J. Wambach, *Phys. Rev. Lett.* **93** (2004) 122501.
- [86] S. Drożdż, S. Nishizaki, J. Speth, and J. Wambach, *Phys. Rep.* **197** (1990) 1.
- [87] Ph. Chomaz D. Lacroix and S. Ayik, *Phys. Rev. C* **58** (1998) 2154.
- [88] D. Lacroix, S. Ayik, and P. Chomaz, *Phys. Rev. C* **63** (2001) 064305.
- [89] C.A. Bertuliani and V.Yu. Ponomarev, *Phys. Rep.* **321** (1999) 139.
- [90] C. Yannouleas, M. Dworzecka and J.J. Griffin, *Nucl. Phys. A* **397** (1983) 239.
- [91] A. Mai, Diploma thesis, TU Darmstadt (2000).

- [92] K. Ando, A. Ikeda and G. Holzwarth, *Z. Phys. A* **310** (1983) 223.
- [93] S. Ayik and M. Dworzecka, *Phys. Rev. Lett.* **54** (1985) 534.
- [94] A.B. Migdal, *Theory of Finite Fermi Systems and Application to Atomic Nuclei* (John Wiley and Sons, New York, 1967).
- [95] S. Kamenetzkiy, J. Speth, and G. Tertychny, arXiv:nucl-th/ 0311058v1.
- [96] V.G. Soloviev, *Theory of Atomic Nuclei: Quasiparticles and Phonons* (IOP Publishing, Bristol, 1992).
- [97] B. Reitz, A.M. van den Berg, D. Frekers, F. Hofmann, M. de Hoo, Y. Kalmykov, H. Lenske, P. von Neumann-Cosel, V.Yu. Ponomarev, S. Rakers, A. Richter, G. Schrieder, K. Schweda, J. Wambach and H.J. Wörtche, *Phys. Lett. B* **532** (2002) 179.
- [98] N. Ryezayeva, T. Hartmann, Y. Kalmykov, H. Lenske, P. von Neumann-Cosel, V.Yu. Ponomarev, A. Richter, A. Shevchenko, S. Volz, and J. Wambach, *Phys. Rev. Lett.* **89** (2002) 272502.
- [99] V. Y. Ponomarev, V. G. Soloviev, C. Stoyanov, and A. I. Vdovin, *Nucl. Phys. A* **323** (1979) 446.
- [100] T. Guhr, A. Müller-Gröling, and H.A. Weidenmüller, *Phys. Rep.* **299** (1998) 189.
- [101] E.P. Wigner, in: C.E. Porter (Ed.), *Statistical Theories of Spectra: Fluctuations* (Academic Press, New York, 1965), p. 200.
- [102] Y. Kalmykov, Dissertation D17, TU Darmstadt (2005).
- [103] H. Diesener, U. Helm, G. Herbert, V. Huck, P. von Neumann-Cosel, C. Rangacharyulu, A. Richter, G. Schrieder, A. Stascheck, and A. Stiller, *Phys. Rev. Lett.* **72** (1994) 1994.
- [104] The Euroball Home Page, <http://nnsa.dl.ac.uk/euroball-home/>.
- [105] L.Y. Lee, *Prog. Part. Nucl. Phys.* **38** (1997) 65.

Danksagung

Diese Arbeit wurde nur durch das Zusammenwirken vieler möglich, denen ich an dieser Stelle herzlich danken möchte.

Herrn Professor Dr. Dr. h.c. mult. Achim Richter danke ich sehr nicht nur dafür, daß er mich in seine Arbeitsgruppe aufnahm und mir damit die Möglichkeit gab, an der Technischen Universität Darmstadt zu promovieren, sondern auch für sein stetes Interesse am Fortgang dieser Arbeit. Außerdem danke ich auch für die Möglichkeit, an mehreren Experimenten, Konferenzen und Workshops teilnehmen zu dürfen, wodurch meine Sichtweite entscheidend erweitert wurde.

Herrn Professor Dr. Jochen Wambach danke ich für die Übernahme des Korreferats und die vielen wertvollen Diskussionen, Ideen und Anregungen.

Herrn Priv.-Doz. Dr. Peter von Neumann-Cosel bin ich für die ständige Unterstützung meiner Arbeit und enorme Hilfe bei der Interpretation der Daten recht herzlich dankbar.

Special thanks go to Professor. Dr. John Carter for numerous discussions, permanent help at all stages and an interest in the progress of this work.

I am indebted to Vladimir Ponomarev and Denis Lacroix for providing calculations and for many helpful discussions. I would also like to thank many collaborators from South Africa, R.W. Fearick, S.V. Förtsch, F.D. Smit, R. Neveling, R. Newman, E. Sideras-Haddad, for helping during the beam time and data analysis. Special thanks to J.J. Lawrie and the cyclotron team at iThemba LABS for providing stable high-quality beam for the experiments. My thanks go also to the colleagues from Japan, Y. Fujita and H. Fujita, for many ideas in our joint work.

Bei meinen Freunden und Kollegen aus dem IKP, insbesondere S. Khodyachykh, Y. Kalmykov, N. Ryezayeva, sowie bei Dr. Harald Genz und J. Zwarych möchte ich mich für das sorgfältige Durchlesen dieser Arbeit und die freundliche Unterstützung vielmals bedanken.

Diese Arbeit wurde gefördert durch die Mittel der DFG im Rahmen des Förderprojekts 445 SUA-113/6/0-1 und des SFB 634.

Lebenslauf

Artem Shevchenko

17. September 1975 Geboren in Kharkiv, Ukraine
- 1982 – 1992 Besuch der Sekundärschule Nr. 62, Kharkiv, Ukraine
- 1992 – 1998 Studium der Physik an der Fakultät für Physik und
Technik der Kharkiver Staatsuniversität (jetzt *Karazin Kharkiv National University*), Ukraine.
- 1995 – 1996 Ausbildung zum Offizier
- Februar 1998 Abschluss des Studiums mit Diplom mit Auszeichnung
- 1998 Wissenschaftlicher Mitarbeiter, *Scientific Center of Physics and Technology "NFTC"* Kharkiv, Ukraine
- Seit 1999 Wissenschaftlicher Mitarbeiter am Institut für Kernphysik der Technische Universität Darmstadt

Erklärung:

Hiermit erkläre ich, dass ich die vorliegende Dissertation selbständig verfasst, keine anderen als die angegebenen Hilfsmittel verwendet und bisher noch keinen Promotionsversuch unternommen habe.

Darmstadt, im Februar 2005

Артем Шевченко